

AD-A096 983 CLEVELAND CLINIC FOUNDATION OHIO DEPT OF RADIOLOGY

F/G 6/5

THE MECHANICS OF LONG BONE FRACTURES

31 JAN 81 MORAN, JAMES M.

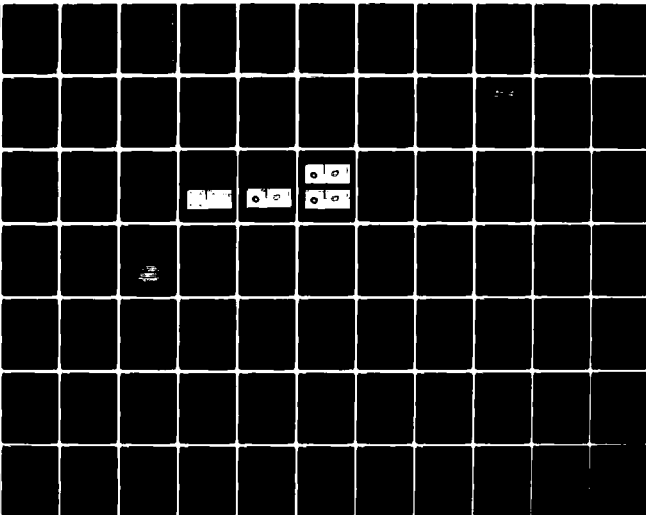
F49620-79-C-0112

UNCLASSIFIED

PROJ. 2312 TASK A2 AFOSR TR-81-0294

NL

1002  
2000000



1002  
2000000



AD A 096983

(16) 23115

(17) A2

(18) AFOSK

(19) 7K-21-0294

THE MECHANICS OF  
LONG BONE FRACTURES,

James M. Moran  
Diane L. Peterson  
Joseph S. Skraba  
Joe H. Gallagher\*  
A. Seth Greenwald

Final Report.

F49620-79-C-0112

April 1, 1979 - January 31, 1981

Prepared for

Air Force Office of Scientific Research  
Bolling AFB, D.C. 20332

CRI 001-81

Cleveland Research Institute  
2351 East 22nd Street  
Cleveland, Ohio 44115

\*Department of Radiology, Cleveland Clinic Foundation

Approved for public release;  
distribution unlimited.

412250

UNCLASSIFIED

SECURITY CLASSIFICATION OF THIS PAGE (When Data Entered)

REPORT DOCUMENTATION PAGE		READ INSTRUCTIONS BEFORE COMPLETING FORM
1. REPORT NUMBER <b>AFOSR-TR-81-0294</b>	2. GOVT ACCESSION NO. <b>AD-A096</b>	3. DECISION & CATALOG NUMBER <b>983</b>
4. TITLE (and Subtitle)  <b>THE MECHANICS OF LONG BONE FRACTURES</b>		5. TYPE OF REPORT & PERIOD COVERED <b>FINAL</b> <b>4/1/79 - 12/31/80</b>
		6. PERFORMING ORG. REPORT NUMBER <b>CRI 001-81</b>
7. AUTHOR(s) <b>A. Seth Greenwald, James M. Moran, Diane L. Peterson, Joseph S. Skraba, Joe H. Gallagher</b>		8. CONTRACT OR GRANT NUMBER(s)  <b>F49620-79-C-0112</b>
9. PERFORMING ORGANIZATION NAME AND ADDRESS <b>Cleveland Research Institute 2351 E. 22nd Street Cleveland, OH 44115</b>		10. PROGRAM ELEMENT PROJECT, TASK AREA & WORK UNIT NUMBERS <b>61102F 2312 A2</b>
11. CONTROLLING OFFICE NAME AND ADDRESS  <b>Air Force Office of Scientific Research (NL) Building 410, Bolling AFB, D.C. 20332</b>		12. REPORT DATE <b>31 January 1981</b>
		13. NUMBER OF PAGES <b>113</b>
14. MONITORING AGENCY NAME & ADDRESS (if different from Controlling Office)		15. SECURITY CLASS. (of this report)  <b>Unclassified</b>
		15a. DECLASSIFICATION DOWNGRADING SCHEDULE <b>N/A</b>
16. DISTRIBUTION STATEMENT (of this Report)  <b>Approved for public release; distribution unlimited.</b>		
17. DISTRIBUTION STATEMENT (of the abstract entered in Block 20, if different from Report)		
18. SUPPLEMENTARY NOTES		
19. KEY WORDS (Continue on reverse side if necessary and identify by block number)  <b>ANTHROPOMETRY; BONE DENSITY; BONE FRACTURE; COMPUTERIZED AXIAL TOMOGRAPHY; CROSS SECTIONAL PROPERTIES; NON-DESTRUCTIVE EVALUATION; WINDFLAIL INJURIES</b>		
20. ABSTRACT (Continue on reverse side if necessary and identify by block number)  <b>Fractures of long bones are a common clinical finding in human trauma situations. These include injuries which are sustained during automotive and aircraft crashes, parachute landings, and aircraft ejection. Irrespective of the trauma-producing environment, extremity fractures are related to the loading state and the rates of application of injury forces, as well as local geometrical and mechanical properties of bone structure. The objectives of this current research are:</b>		

UNCLASSIFIED

SECURITY CLASSIFICATION OF THIS PAGE (When Data Entered)

(1) to gain insight into the fracture behaviour of long bones under singular and combined states of loading through a spectrum of loading rates, and (2) to characterize the geometric and mechanical properties of long bones by non-destructive means.

Using a modified Instron Materials Test System fresh paired canine long bones are being studied under torsional and torsion-compressive states of loading through a spectrum of loading rates. Fracture behaviour is characterized by the torque and energy to failure, angle of twist, fracture type and location.

Additional studies involve the development of techniques employing computerized axial tomography (CT-scan) and automated data reduction to obtain long bone geometric and mechanical properties. Computerized axial tomography allows construction of sequential radiographs in a plane perpendicular to that of a normal flat plate x-ray. This capability allows accurate construction of the cross sectional dimensions and localized tissue densities of long bones under in vivo and in vitro conditions. A correlation has been shown to exist between bone density and mechanical properties. To obtain the geometric properties, a program called PROPS has been developed in the laboratory and used in conjunction with a mini-computer and digitizer to analyze the scans.

Using these procedures, paired cadaver human and baboon femora, tibiae, fibulae, humeri and radii have been analyzed. Experimentally produced fractures have been related to minima of geometric and physical properties and compared with clinically observed fractures.

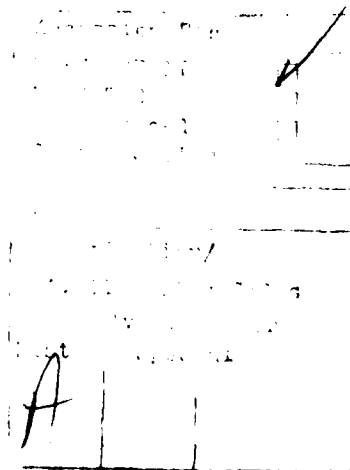
UNCLASSIFIED

SECURITY CLASSIFICATION OF THIS PAGE (When Data Entered)

# THE MECHANICS OF LONG BONE FRACTURES

## Table of Contents

I.	INTRODUCTION	1
II.	THE EFFECT OF LOADING RATE ON FRACTURE BEHAVIOUR	2
2.1	Previous Work	2
2.2	Methods	6
2.2.1	Torsional Loading	6
2.2.2	The Effects of Combined Loading	10
2.2.3	Cancellous Bone Effects	11
2.3	Results	11
2.3.1	Torsional Loading	11
2.3.2	Axial and Torsional Loading	14
2.3.3	Cancellous Bone Effects	16
2.4	Discussion	18
III.	TOPOGRAPHIC PHYSICAL AND CROSS SECTIONAL PROPERTIES	21
3.1	Previous Work	22
3.2	Methods	26
3.2.1	Cross Sectional Property Software	26
3.2.2	CT Scanning Procedure	28
3.2.3	Linear Dependency of Density and Mechanical Properties on Measured CT Number	32
3.2.4	Physical and Cross Sectional Data Collection and Reduction	34
3.3	Results	35
3.4	Discussion	35
IV.	CORRELATION AND UTILIZATION	37
4.1	Relation Between Loading Rate and Cross Sectional Property Studies	37
4.2	Modelling	40
4.2.1	The Canine Fracture Model	40
4.2.2	Utilization of Computed Tomography in Modelling	41
4.4	The Relation to Windflail Injury	42
V.	SUMMARY	44
VI.	RECOMMENDATIONS	45
VII.	REFERENCES	46
VIII.	APPENDIX I	49
IX.	APPENDIX II	50



## I. INTRODUCTION

Fractures of long bones are a common clinical finding in human trauma situations. These include injuries which are sustained during automotive and aircraft crashes, parachute landings and aircraft ejection. Many of the latter are wind flail induced upper extremity injuries resulting from hyperextension of the elbow and hyperabduction of the shoulder. Lower extremity injuries of the tibia, fibula and femur are also common findings (Fryer, 1961; Payne and Hawker, 1974; Combs, 1977). In these situations severe torques, moments and compressive forces act in concert to produce complex states of loading. With the exception of work by Schneck (1976, 1979), little information has been reported that attempts to define the precise nature of this environment. In general, however, fracture behaviour is related to the loading state and the rates of application of injury forces, as well as local geometrical and physical properties. The objectives of this research effort are twofold: (1) to gain insight into the fracture behaviour of long bones under singular and combined states of loading through a spectrum of loading rates in a controlled laboratory environment, and (2) to characterize the geometric and physical properties of long bones by non-destructive means. The methods developed to determine the latter employ computerized axial tomography and automated data reduction and have resulted in a significant capability to measure the anthropometric properties of long bone.

## II. EFFECT OF LOADING RATE ON FRACTURE BEHAVIOUR

Long bone fractures usually occur due to impact of extremities with stationary objects or from rapidly applied loads which cannot be accommodated due to soft and hard tissue restraints. Since bone is a viscoelastic material its response to these fracture producing environments will be a function of loading rate. This aspect of bone behavior is examined in our study by:

1. Determination of the effect of loading rate upon bone failure under torsional loading conditions;
2. Determination of the effect of axial compressive loads on torsional fractures;
3. Analysis of the effect of cancellous bone on torsional fracture characteristics.

### 2.1 Previous Work

Although a considerable number of studies have investigated the mechanical properties of standardized specimens and of whole bone, most have been conducted at low loading rates. The following is a chronological review of pertinent studies that have included testing at higher loading rates.

McElhaney and Byars (1965), using standardized specimens of bovine and human femora, conducted constant-velocity compression tests at strain rates varying from .001 to 1500 sec<sup>-1</sup>. Plotting energy versus strain rate, they noted an increase in the energy absorbing capacity of bone, a peak, then a sharp decline as strain rate increased. They concluded that the



mechanical properties of bone are rate sensitive and that a critical velocity for bone occurs at a strain rate of approximately  $1 \text{ sec}^{-1}$ .

Experimental impact torsion tests of intact fresh and embalmed human tibia have been performed by Burstein and Frankel (1968). The tibia was rigidly fastened to a pendulum and the unit was allowed to gain kinetic energy at the expense of its potential energy. When maximum velocity was attained, the grip on the distal end of the tibia struck a stop and the pendulum, with the proximal end of the bone, continued to rotate. The loading duration was .1 second. A second series of tests were then conducted at a loading duration of one minute to determine if there were significant differences in the energy absorbing capacity. The tests showed a considerable variation among the individual bones. However, they were able to obtain three paired specimens thus allowing direct comparisons. A reduction in energy capacity of about 55% was found, compared to only a 20% difference noted by McElhaney and Byars in their standardized specimens. They attributed this difference to the presence of cancellous structure and a more complex stress field existing in whole bones.

Piekarski (1970), using machined bovine femur specimens in bending tests, measured the energy required for crack propagation and observed microscopically the mechanism of fracture. He noted that at low strain rates cracks propagate along Haversian lamellae and at high rates propagate

indiscriminately through all the micro-constituents. He concluded that bone behaves as a tough material at low strain rates and fractures as a brittle material at high strain rates.

Sammarco, Burstein, and Frankel (1971) conducted a study to determine the effect of loading rate on the ultimate properties of bone. Their results were obtained from torsional tests of 31 pairs of fresh canine bone tested at both a high and a low loading rate. The right bones were broken rapidly, with a loading time of 40-60 milliseconds for fracture, while the left bones were broken slowly, with loading times of between 120-180 seconds required for fracture. For each pair, and for each parameter studied they calculated the ratio  $(F-S)/((F + S)/2)$  where F is the value for the bone loaded quickly, and S for that loaded slowly. The parameters for which F and S could stand were maximum torque, energy absorption, and angular deformation. Expressed as a percentage, angle of twist was found to be 112 per cent; maximum torque, 133 per cent; and energy recorded to fracture, 144 per cent. They concluded that whole dog bone exhibits viscoelastic properties and the amount of torque and energy the bone absorbs increased at the higher loading rate.

Panjabi, White, and Southwick (1973) conducted a similar torsion experiment on fresh rabbit femora and ulnae. The same mechanical parameters were determined under five loading rates ranging from .003 to 13.2 radians per second. They found

that maximum torque, maximum torsional deformation and energy absorbed to fracture all increased with the rate of deformation, reached a maximum, and then declined.

Using uniaxial tensile tests, Wright and Hayes (1976) studied the relation between strain rate and density on ultimate strength. They tested standardized longitudinal specimens of bovine compact bone at strain rates ranging from  $5.3 \times 10^{-4}$  to  $237 \text{ sec}^{-1}$ . The test results demonstrated a highly significant correlation between ultimate strength and strain rate, and between ultimate strength and density. Strain rate also had a significant effect on the energy absorbing capacity of bone. The specimens tested at higher strain rates generally absorbed more energy during failure. However, unlike some previous studies, they found no evidence of a critical rate at which the energy absorbing capacity attains a maximum.

From a slightly different viewpoint, Ducheyne, Martens, et al. (1977), investigated the microscopic fracture aspects of impact tested bones. Human tibiae and femora were torsion tested to yield fractures within .05 seconds and 30 seconds. A scanning electron microscope was used to correlate fracture behavior with bone structure. Throughout the impact fracture surfaces both ductile and brittle fracture characteristics were observed. However, the brittle fracture mode was predominant during propagation, indicating a higher energy absorption in this fracture regime. They remarked that, "The conclusion that a higher energy absorption to failure upon increasing strain rate is

linked to an increased brittleness and a more marked brittle fracture surface morphology is as yet not established."

A recently published study conducted by Martens, et al. (1980), utilized human femoral and tibial whole bone specimens. These specimens were subjected to torsional loading at high strain rates; fractures occurring within 100 milliseconds. Torque versus angular deflection was recorded. They calculated strain energy before fracture, torsional stiffness, maximum torque and ultimate deflection. A high variability of these mechanical parameters was observed, and was attributed to differences in geometry of the bones.

One final relevant study, by Miller and Piotrowski (1974), was concerned with the variability of the torsional strength of paired bones. Monkey, dog, and rat bones were utilized to determine if a right-left bias existed. No statistical difference was noted and it was concluded that the torsional strength of matched bone pairs can be expected to be equal.

## 2.2 Methods

### 2.2.1 Torsional Loading

An examination of the effects of loading rate on bone under a torsional load has been conducted in an attempt to clarify this relationship. Torsional loading was chosen for several reasons: 1) in every cross section of a test body the torque remains constant, therefore causing failure to occur in the weakest section; 2) torque and angular velocity can be easily

measured and 3) torsion is a realistic loading mode producing failure similar to clinically observed fractures.

Paired canine radii were tested utilizing the entire loading rate spectrum of an Instron Testing Machine (Model 1115). This system is capable of rates ranging from .0533 to 53.3 revolutions per minute (.0558 to 5.58 radians per second).

The bones obtained for this experiment were from adult canine mongrels utilized for various research projects not affecting the skeletal system. As soon as possible after animal sacrifice, the bones were removed and cleared of all soft tissue. The bones were paired and kept wet until tested. If the specimens could not be tested the day they were obtained, they were packaged and frozen at  $-20^{\circ}$  C. Freezing has been shown to have no significant detrimental effect on the mechanical properties of bone (Sedlin, 1966), an observation confirmed by our results.

In preparation for testing the bones were mounted in brass fixture cups with center pins. Proper position and alignment were maintained by placing the cups in a drill press, using it as a vise. Cerrobend, an alloy with a melting temperature of  $158^{\circ}$  F, was then poured around the bone ends (Figure 1). After the Cerrobend had set, the brass fixture cups were placed within a second set of concentric cups and mounted in the Instron. This outer pair of cups was designed to insure that the torsion unit of the Instron has accelerated to the desired rate before actual loading of the bone took place. This acceleration

occured as the outer cup spun around the inner cup. The two cups engage by means of a pin and the bone was then externally rotated at the specified loading rate (Figure 2).

Figure 1

Alignment and mounting  
in cerrobend

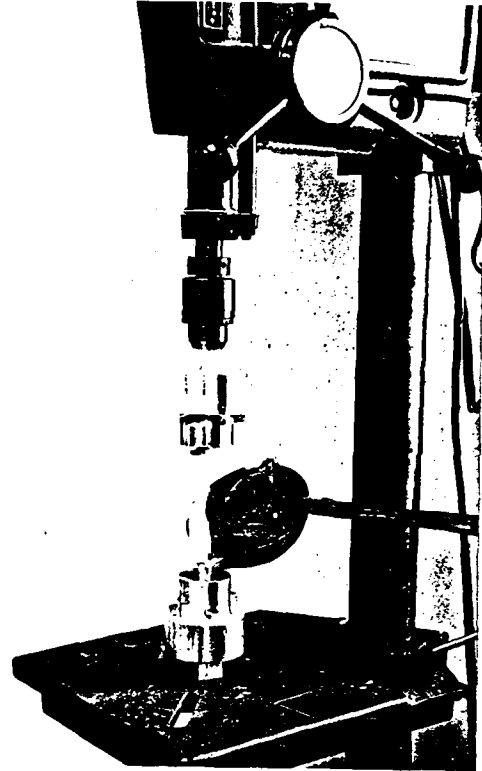
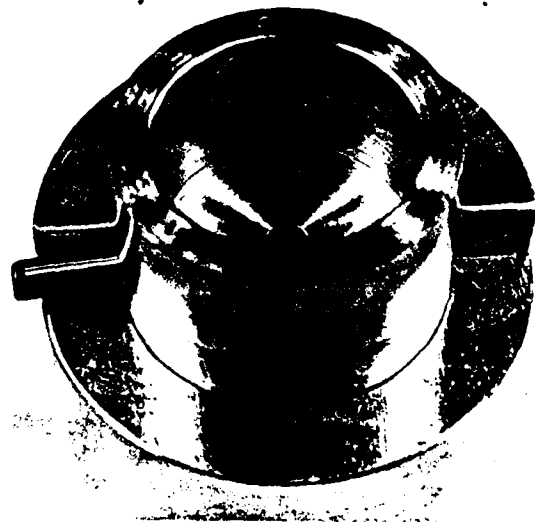


Figure 2

Mounting cups



The right bone of each pair was tested at the slowest loading rate (.0533 rpm), while the left one was tested at one of the faster rates (.267, .533, 2.67, 5.33, 10.33, 26.7, 53.3 rpm). This pattern was not altered as it has been shown that there is no significant side-to-side variation in the mechanical properties of paired bones (Miller and Piotrowski, 1974). Since the loading rate of the right bone was kept constant, it was used as a control to compare the effect of increased loading rate on the left bone. The parameters recorded were: maximum torque, energy absorbed, angle of twist at failure, and the time required for fracture. Also noted was the type and location of the fracture and, when possible, the fracture angle was measured with a goniometer.

The Instron load cell was connected to a Gould strip chart recorder (Model 2400) with the vertical pen displacement indicating the magnitude of the torque and horizontal displacement indicating the angle of rotation. Using a Hewlett-Packard 9874A digitizer and 9845T desktop computer, the area under the torque-rotation curve was calculated. This area represents the amount of energy absorbed by the bone until fracture. A Tektronix oscilloscope was also used to insure that the pen response of the chart recorder was sufficient to capture the event.

### 2.2.2 Axial and Torsional Loading

A similar study was conducted to determine the effect of combined loads at different loading rates. The mounting and testing procedure previously described in Section 2.2.1 was followed except that the bone was subjected to a compressive load in addition to the applied torque. The right bone was used as a control and was broken at the lowest loading rate in pure torsion. This method made it possible to note the effect of the axial load and also to compare these results with those from the previous study using torsional loading only. A compressive load of 45 kg was applied axially to the bones by a loading fixture comprised of three pneumatic cylinders (Figure 3). The bones were then torsionally loaded utilizing the entire loading rate spectrum as before. The same parameters, torque, energy and angle of twist were recorded.

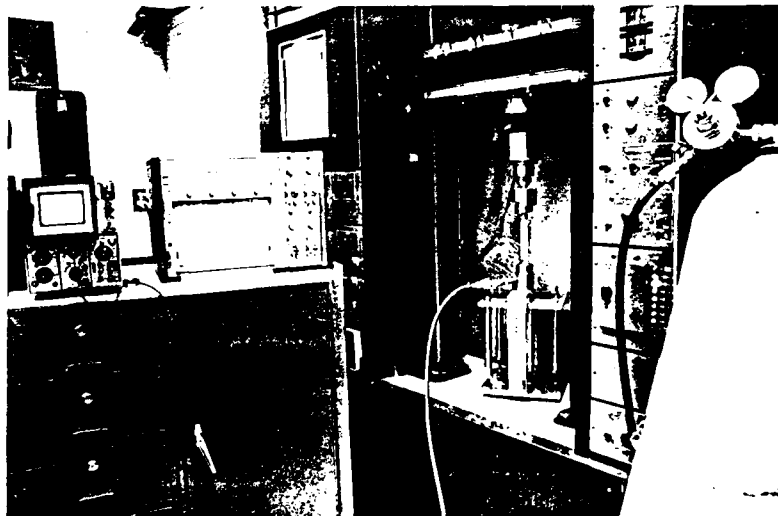


Figure 3

Testing and recording apparatus-  
Combined torsional and axial loading experiment



### 2.2.3 Cancellous Bone Effects

To investigate the effect cancellous bone has on energy absorption, canine tibiae were prepared in a manner similar to that previously described in Section 2.2.1, with the exception that one of the bones from each pair was cleared of all cancellous bone. This was accomplished by drilling a hole in each end of the bone and reaming the medullary canal. Flexible reamers capable of negotiating the curvature of the shaft were used (Berry, et al., 1978). Both the reamed and unreamed bone of each pair was then torsionally loaded at one of three loading rates covering the available spectrum of the Instron (.533, 5.33, and 53.3 revolutions per minute). The maximum torque and amount of energy absorbed to failure was again measured.

Canine tibiae were chosen for these tests rather than radii as their larger size and straighter shaft facilitated the reaming procedure. Additionally, since the tibia has a large amount of trabecular bone, its absence might produce a more pronounced effect.

## 2.3 Results

### 2.3.1 Torsional Loading

While establishing the experimental protocol 70 pairs of specimens were broken. These preliminary results are not reported. Fractured specimens which showed signs of immaturity or any physiologic abnormality are also not represented in the reported data.

To compare the effects of the loading rate between different bone pairs, a non-dimensional quantity was calculated according to the following relation,  $\bar{X} = X_L/X_R$ , where the variable  $X$  stands for one of the three parameters recorded.  $X_R$  indicates the right bone which was always tested at the slowest loading rate and  $X_L$  indicates the left bone which was broken at one of the higher loading rates. The three parameters for which the variable  $\bar{X}$  can stand are the maximum torque attained ( $\bar{T}$ ), energy absorbed until fracture ( $\bar{E}$ ), and the angle of twist at failure ( $\bar{A}$ ). These dimensionless ratios enable the comparison of different paired specimens by minimizing the effects of bone size, geometry, histological differences, or other factors that may exist between different pairs of bones. These non-dimensional parameters are an indication of the effect of the torsional loading rate.

Ten pairs of canine radii were broken at each of the seven different loading rates, a total of 140 specimens. Means and standard deviations for the parameters  $\bar{T}$  and  $\bar{E}$  were plotted versus loading rate. A best-fit curve analysis was performed and the resulting polynomial curve was drawn (Figures 4 and 5). Correlation coefficients for  $\bar{T}$  and  $\bar{E}$  were .85 and .73, respectively. Means and standard deviations for the angle of twist data was plotted; no trend is evident (Figure 6).

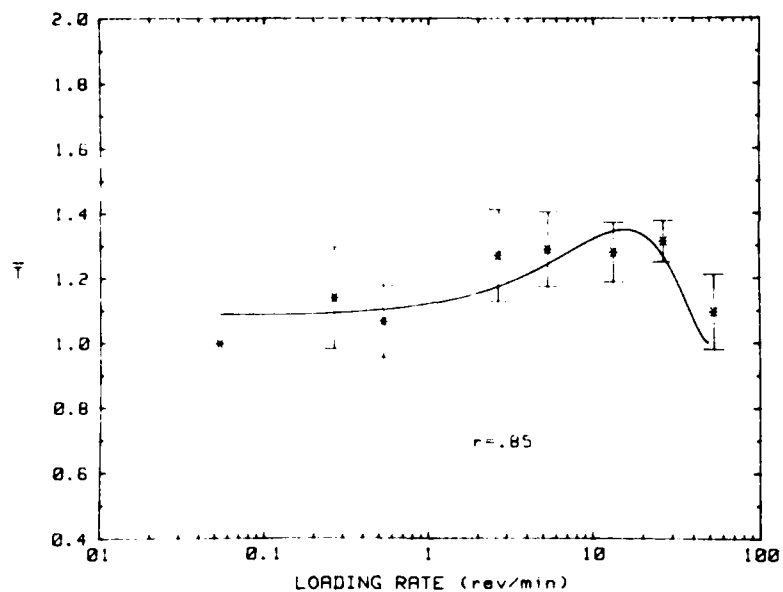


Figure 4

Torque versus loading rate (torsional load)

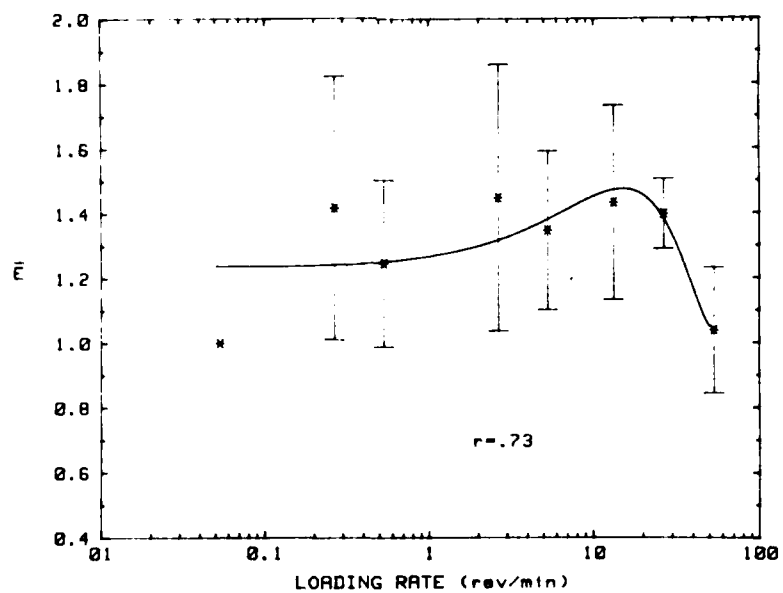


Figure 5

Energy versus loading rate (torsional load)

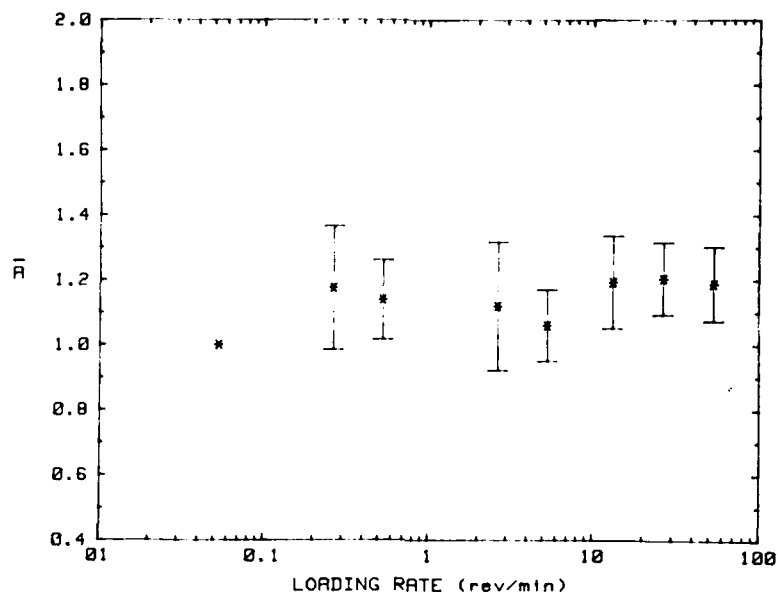


Figure 6

Angle of twist at fracture versus loading rate (torsional load)

### 2.3.2 Axial and Torsional Loading

To analyze the results of the combined loading tests the same procedure as outlined in Section 2.3.1 for the torsional loading studies was followed. The parameter  $X_L$  indicates the left bone which was axially loaded. Ten pairs of canine radii were broken at eight different loading rates (160 specimens). Again a best-fit curve analysis was performed and the resulting polynomial along with the means and standard deviations for the parameters  $\bar{T}$  and  $\bar{E}$  were plotted (Figures 7 and 8). Correlation coefficients for  $\bar{T}$  and  $\bar{E}$  were .78 and .86, respectively. As before, no trend was realized in the angle of twist data (Figure 9).

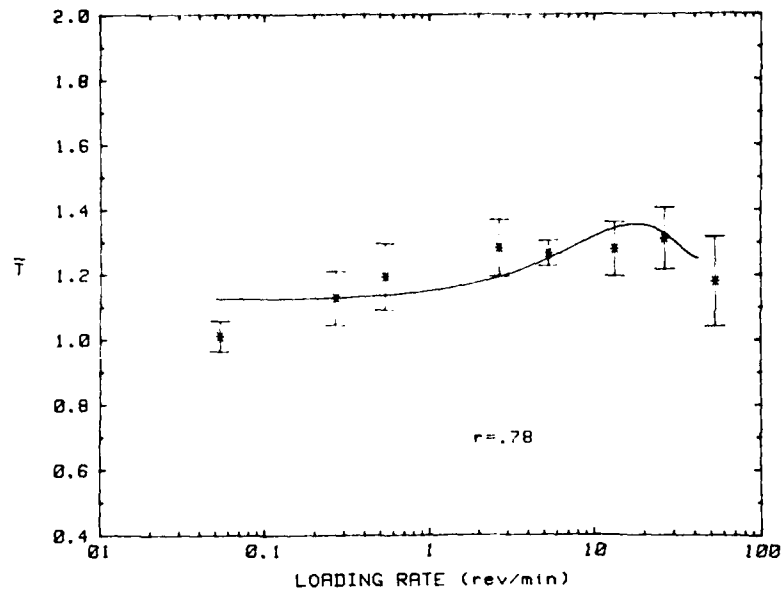


Figure 7

Torque versus loading rate (torsional axial load)

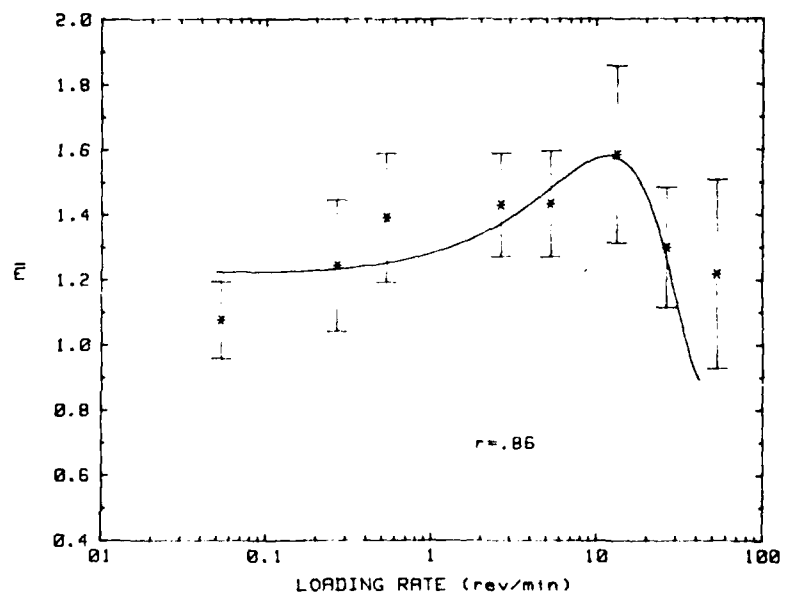


Figure 8

Energy versus loading rate (torsional axial load)

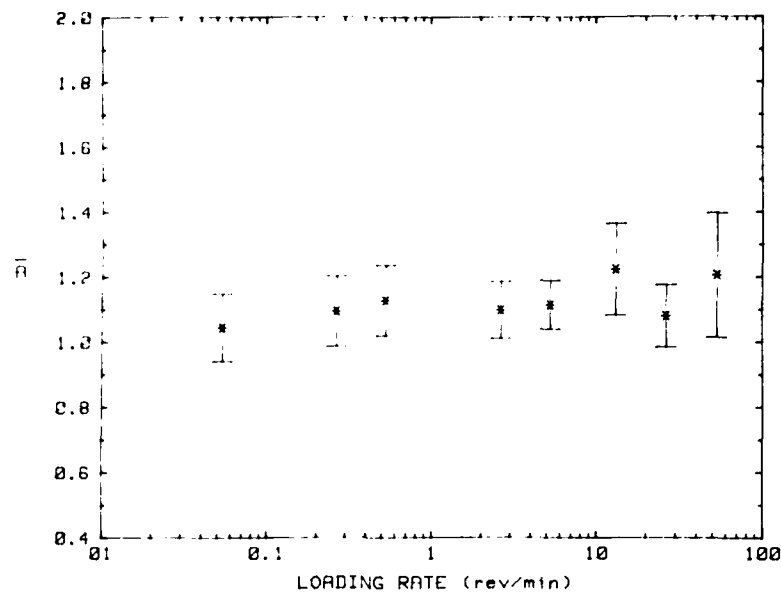


Figure 9

Angle of twist at fracture versus loading rate (torsional axial load)

### 2.3.3 Cancellous Bone Effects

A non-dimensional ratio was again used to compare the difference between the reamed and the non-reamed bones. In this case the ratio used was  $\bar{X} = X_R/X_{NR}$ , where  $X_R$  stands for the reamed bone and  $X_{NR}$  stands for the bone that was not cleared of cancellous structure.  $\bar{X}$  represents either maximum torque ( $\bar{T}$ ) or energy absorbed ( $\bar{E}$ ).

The data was subjected to a Student's t test to determine if cancellous bone plays a significant role in energy absorption at the loading rates used. The results indicate that no significant difference ( $p \leq .25$ ) exists between the reamed

and non-reamed bones (Table I). Based on the specimens tested, this finding implies that long bones may be adequately modelled as hollow tubes rather than as composite structures.

TABLE I  
CANCELLOUS BONE EFFECTS  
CANINE TIBIA  
Five Pairs at Each Loading Rate

	TORQUE	ENERGY
(rev/min)		
.533	$\bar{T} = .916$ $t = 3.89$ ( $p \leq .0025$ )	$\bar{E} = .884$ $t = 1.335$ ( $p \leq .25$ )
5.33	$\bar{T} = .960$ $t = .689$ ( $p \leq .25$ )	$\bar{E} = .906$ $t = .762$ ( $p \leq .25$ )
53.3	$\bar{T} = .836$ $t = 4.89$ ( $p \leq .001$ )	$\bar{E} = .750$ $t = 3.786$ ( $p \leq .005$ )

$$\bar{T} = \frac{T_{\text{reamed}}}{T_{\text{non-reamed}}}$$

$$\bar{E} = \frac{E_{\text{reamed}}}{E_{\text{non-reamed}}}$$

## 2.4 Discussion

Both pairs of curves,  $\bar{T}$  and  $\bar{E}$  versus loading rate for torsional loading and for combined torsional and axial loading, are of similar nature. On a semi-log plot, all curves start at a minimum, increase slowly, reach a peak and then drop off. However, when comparing  $\bar{T}$  for pure torsion to  $\bar{T}$  for combined loading, the combined loading plots exhibit a slightly higher magnitude, indicating an effect of axial load on the bone. Maximums in the curve occurred at 15.5 rev/min and 14.8 rev/min for  $\bar{T}$  and  $\bar{E}$ , respectively, under pure torsional loading. For axial and torsional loading, the maximums for  $\bar{T}$  and  $\bar{E}$  occurred at 17.6 rev/min and 11.8 rev/min, respectively.

The slightly increased torque to failure which occurs when a concurrent compressive axial load is applied appears reasonable. Compressive stresses may act to mitigate torsion induced tensile stresses. It would be interesting to see if the effect of higher axial loads would be to exaggerate this difference, in the absence of buckling.

Most bones tested exhibited a spiral type fracture typical of tubular structures loaded in torsion. Fracture generally initiated at the proximal end of the bone. The loading rate did not appear to influence the position on the bone where fracture occurred as suggested by Sammarco, et al. (1971). Comminution occurred frequently at the rapid loading rates, indicating the relationship of fracture to energy dissipation, since crack formation is an energy dissipating mechanism (Figure 10).



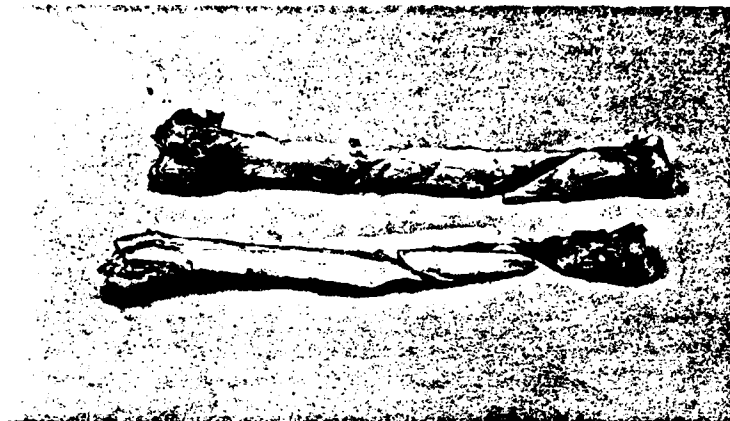


Figure 10

Spiral Fracture (top) and Comminution (bottom)

Torsional testing conducted on a large population over a wide range of loading rates is not found in the literature. Several investigators have noted an increase in the energy absorbing capacity of bone at higher loading or strain rates. Sammarco, et al., found this increase, testing specimens at only two rates, thereby implying a continuously increasing energy absorption. Panjabi, et al. (1973), using five different loading rates obtained curves for torque or energy versus loading rate that increased to a maximum and then declined. This trend is in general agreement with the results obtained for the pure torsion and the combined loading tests conducted in our study. Panjabi averaged the results from both rabbit femora and ulnae but did not indicate the statistical significance of the data. In our study, 160 specimens, ten pairs at

each of eight selected loading rates, were tested producing curves with relatively high correlation coefficients. By using a large sample population and non-dimensional parameters, experimental artifacts and biological variations are minimized.

Studies relevant to the fracture mechanisms of whole bones under combined torsional and axial loading and at different loading rates have not been previously reported. Fractures produced under this combined state of loading are representative of those clinically found in human trauma situations.

### III. TOPOGRAPHIC PHYSICAL AND CROSS SECTIONAL PROPERTIES

The fracture behavior of a long bone cannot be completely characterized unless the geometry of the bone and any regional variations in strength within the bone are determined. An ideal method to accomplish this would be non-destructive so that the specimens would also be available for histological study or mechanical testing. The data derived from such experiments could be put to other uses, such as modelling of bone fractures.

In this section the geometric and physical properties of long bones have been determined. One of the exciting fallouts of this work has been the development of non-destructive techniques employing computerized axial tomography (CT-scan) and automated data reduction to obtain this information. Originally it had been proposed to utilize hardness plots to determine local strength variations. This method can only be employed on the bone surface and due to the curvature of the bone repeatability is poor. Additionally, the Structural Dynamics Research Corporation SPOTS program was originally used to determine the cross sectional properties. It was found to be time consuming and tedious in application, and to have difficulty representing certain bone cross sections. Computerized axial tomography allows construction of sequential radiographs in a plane perpendicular to that of a normal flat plate x-ray. This capability permits accurate simultaneous construction of the cross sectional dimensions and delineation of localized tissue densities

of long bones under in vivo and in vitro conditions. In addition, the data is stored on a magnetic medium and may be readily recalled and manipulated. A method has been developed to rapidly and accurately process the vast amount of data which is generated.

### 3.1 Previous Work

Of the seven articles found in the literature on property determination of bone, three are concerned with the geometric properties of the human tibia, one deals with physical properties of the human femur, while the remaining three further develop algorithms and procedures to compute cross sectional geometric properties.

The first of the papers (Minns, Bremble and Campbell, 1975) described a method in which seven serial sections are taken at intervals ranging from 20 to 80% of the total bone length. A cartesian grid is superimposed upon a photograph of the section and the coordinates of the grid are used as input for a computer program to calculate the geometric properties. The results from four left human tibiae showed that the minimum cross sectional area occurred at 80% of the total length. The minimum moment of inertia fell between 70 and 80% of the length and the minimum polar moment of inertia occurred at 70% where it would be expected that mechanical failure due to torsional loading only would occur.

The second of the papers on the geometric properties of the human tibia (Miller and Purkey, 1980) analyzed right-left variability, sex related differences, and expected difference between individuals. Nine pairs of embalmed human tibiae were obtained: three male, two female, and four of unknown gender. Fifteen serial sections were cut from each tibia representing cross sections from 20 to 80% of the total length. A dimension reference was marked on each section and an enlarged tracing of the cortical bone and reference mark was produced with the aid of an opaque projector. The coordinates of the inside and outside boundary of each cross section were used as input for a computer program. The results indicated a significant difference in properties between pairs of bones from different individuals yet the graphs had similar shapes. No statistically significant right-left bias was observed. Also, the minimum polar moment of inertia occurred at 70% of the length. This corresponds to the primary location of clinically observed torsional fractures.

Incidental to their finite element analysis of the human tibia, Piziali and Hight (1976) determined the cross sectional properties of four cadaver specimens. Inertial properties were largest at the metaphyses and diminished in the shaft. Cross sectional area followed a similar pattern but the overall variation was not as pronounced. Minima of inertia and area occurred at approximately 20% superior to the distal end.

In a study of the physical properties of the human femur, Evans and Lebow (1953) used samples of compact bone which were cut longitudinally from anterior, posterior, medial, and lateral quadrants of the proximal, middle, and distal thirds of the femoral shaft. Both wet and dry samples were used, each sample being machined to a standard size. These samples were then tested to determine the modulus of elasticity, ultimate tensile strength and hardness. Femurs from five male caucasian cadavers ranging in age from 58 to 81 were studied. The results indicated no significant difference between modulus of elasticity and hardness for the wet and dry samples from various quadrants. Further, the middle third exhibited the highest average modulus of elasticity (14.6 GPa), maximum hardness, and highest average ultimate tensile strength (83.2 MPa). The proximal third had the lowest average modulus of elasticity (13.5 GPa), minimum hardness, and the lowest average ultimate tensile strength (77.6 MPa). Air drying the samples increased the modulus of elasticity 17.6% and the hardness 54.3%. The average ultimate tensile strength also increased by 31.3%.

The final three papers deal with development of geometric property determination procedures. In the first of these articles, Lovejoy and Burstein (1977) obtained laminograms of five left human tibiae, taken at half their length. These sections were removed from the bone and photographs were projected with laminograms onto a cartesian grid. The coordinates from the grid were used as input for a computer program to calculate

the various geometric properties. Laminogram and bone section results were then compared and the percent error determined. The average error for all geometric properties (i.e. area, moments of inertia, and polar moment) were less than 6%. This paper confirms the accuracy of using x-ray cross sections of bone for geometric property computations. Also, the procedure using laminograms allows the bone specimen to be left intact for further testing.

A similar study was done by the same author (Lovejoy and Barton, 1980) using a radial grid instead of the cartesian grid for data reduction. The average error was found to be less than 8% for the various properties. The benefit of this method was that individual sectional properties could be determined more rapidly than with the previous cartesian grid method. The average time for data reduction was reduced from more than 45 minutes to about two minutes. With the advent of automated techniques, however, this method must still be considered slow.

Nagurka and Hayes (1980) developed an algorithm to determine geometric properties of irregular shapes and suggested its application to long bone studies.

It is anticipated that knowledge of the locations of material and cross sectional weakness, when correlated to the location of fracture sites, will increase our understanding of long bone fracture mechanics. In turn, this may lead to better methods of fracture prevention.

## 3.2 Methods

### 3.2.1 Cross Sectional Property Software

An interactive program has been written to determine the bone cross sectional properties. The complexity of the shapes involved precludes manual computation of these properties. Originally, as has been mentioned, it was intended to use SPOTS (Section Properties of Thin-walled Sections) to facilitate sectional property data collection. However, the amount of manual pre-processing necessary to faithfully represent the sections was found to be considerable. The SPOTS program is finite element based and requires the bone to be broken up graphically into rectangles and arc segments. Certain coordinates of these base figures are then used to define the bone shape. The construction of many small elements is necessary for the complex shapes involved.

Because of the tedious nature of the above procedure, it was decided to approach the problem from a different viewpoint. A Hewlett-Packard desktop computer (Model 9845T) and digitizer (Model 9874A) were used to implement section property software based partially on an algorithm presented by Wojciechowski (1976). The fundamental equations and a basic flow chart of this program called PROPS are contained in Appendix I. The section under consideration must be entirely contained in the first quadrant of the digitizer coordinate system. Coordinates may be digitized at intervals as small as .1 mm, but a 1 mm interval has been found to give reliable results. The procedure is fast



and efficient since the operator merely traces the exterior boundary of the bone in a clockwise direction and the interior medullary canal in a counterclockwise direction with the digitizer cursor. Pertinent cross sectional property output includes area, maximum and minimum principal moments of inertia and polar moment of inertia.

The analytical solutions for properties of selected shapes have been compared with results numerically calculated by PROPS. It can be seen by the comparison in Table II that agreement is excellent.

TABLE II

Shape	Area	I Min	I Max	J
Circular Ring	.083	-2.62	1.24	-.67
Elliptical Ring	2.73	3.87	-.40	.98
Triangle	.32	1.17	.19	.60

Percent error in selected properties.

The only anomaly that has been found is that when two successive points have the same x coordinate, a division by zero occurs in the product of inertia calculation. The program notes this occurrence, ignores the term in the summation and continues execution.

The PROPS program as we have implemented it has several advantages over SPOTS. It does not require any manual measurements, therefore reducing the occurrence of operator error and overall computation time. Much more data is acquired and the nature of the algorithm results in a more realistic model of the cross section.

### 3.2.2 CT Scanning Procedure

Specimens are kept in a freezer at  $-20^{\circ}\text{C}$  after collection. The desired specimen is removed from the freezer to thaw before testing. It is then stripped of flesh and bony landmarks which denote the area to be scanned are identified. The bone is sealed in a circular tank completely filled with water. The water, in addition to preventing dehydration, acts as one of the references needed to relate CT number to density. The bone is then scanned in 10 mm increments utilizing an Ohio Nuclear Model 2020 scanner.

Figure 11a shows a scan of paired baboon humeri (top) and femora (bottom). The scans are also displayed simultaneously in color (Figure 11b). The circular objects in the center of the picture are phantoms used to check machine calibration and for reference dimensions. The display has been processed so that

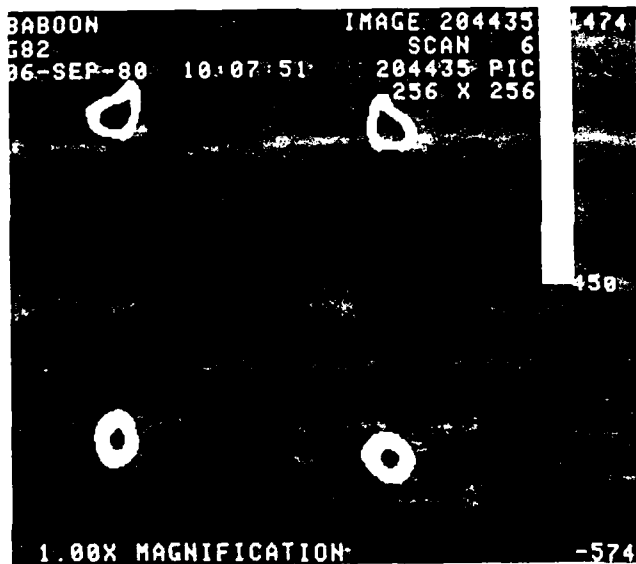


Figure 11a

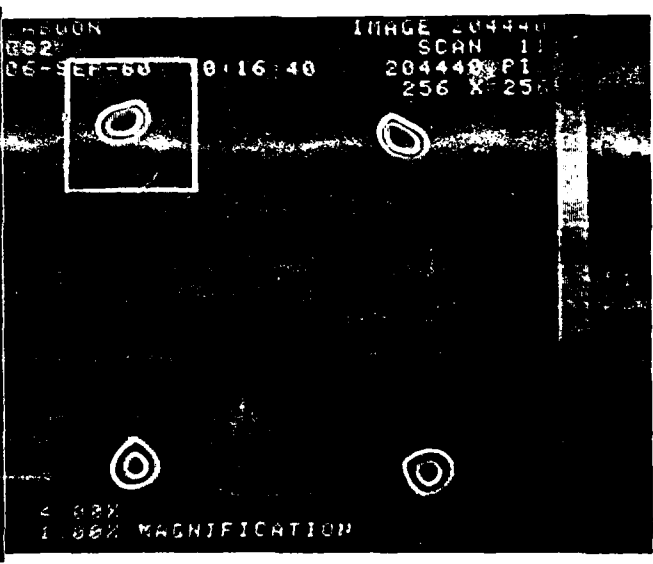


Figure 11b

Color and black and white scans of paired baboon humeri (top) and femora (bottom). The black and white scan is 5 cm more proximal.

CT numbers above 450 appear white and those below 450 appear black. This sharpens resolution of the boundaries and aids digitization. The boundaries are non-distinct due to partial volume artifact, that is, the picture elements (pixels) on the boundary not only encompass bone but surrounding water as well. The result is an artificially low CT number somewhere between that of bone and water. This appears as a light blue halo in Figures 11-14b. Since the minimum CT number of cortical bone is approximately 900 and that of water is 0, a cutoff value of 450 rejects pixels which are less than 50% bone. It is obvious that the boundaries in Figures 11-14b are much less distinct than those of Figures 11-14a.

A bone is selected by positioning a frame over it (Figure 11b) and is then enlarged (Figure 12). The coarse



Figure 12a

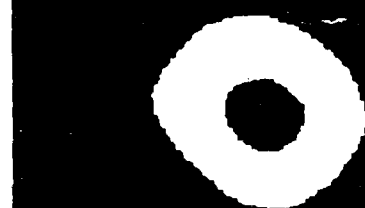


Figure 12b

The desired bone is magnified.

boundaries which result can be smoothed by further data processing (Figures 13 and 14). The black and white image is photographed for projection onto a digitizer platten.

BABOON  
G82  
06-SEP-80 10:07:51  
IMAGE 204435  
SCAN 6  
204435 PIC  
256 X 256



4.00X MAGNIFICATION

1474 BABOON  
G82  
06-SEP-80 10:16:40  
IMAGE 204440  
SCAN 11  
204440 PI  
256 X 256



4.00X MAGNIFICATION

Figure 13a

Figure 13b

The boundary is smoothed.

BABOON  
G82  
06-SEP-80 10:07:51  
IMAGE 204435  
SCAN 6  
204435 PIC  
256 X 256



4.00X MAGNIFICATION

1474 BABOON  
G82  
06-SEP-80 10:16:40  
IMAGE 204440  
SCAN 11  
204440 PI  
256 X 256



4.00X MAGNIFICATION

Figure 14a

Figure 14b

The boundary is smoothed again and the bone is ready to be photographed.

Error can be introduced if the bone is not scanned perpendicular to its long axis. Every effort is made to insure that this error does not occur but a certain amount is inescapable since most long bones have a slight natural curvature. An attempt was made to quantify this error. If a long bone is assumed to be a thick walled circular cylinder and if it is cut or scanned at some angle  $\theta$  to its long axis, a thick walled elliptical section will be revealed. The properties of the circular and elliptical sections have been compared as a function of the angle  $\theta$ . The difference in area was found to be a function of  $\sec \theta$  and the difference in moments of inertia was found to be a function of  $\sec^3 \theta$ . This is plotted in Figure 15. It can be seen that for angles as large as  $10^\circ$  the error is small.

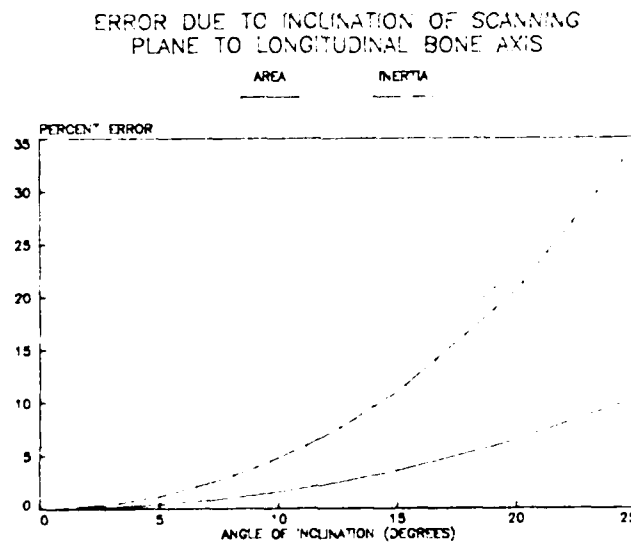


Figure 15

Estimate of error introduced by inclination of the scanning plane  
to the bone axis.

### 3.2.3 Linear Dependency of Density and Mechanical Properties on Measured CT Number

Computed tomography (CT) is a well developed diagnostic imaging method for determining the linear attenuation coefficient of x-rays passing through an object. An image of numbers which is proportional to the linear attenuation coefficients is computed from precise measurements at many positions and many angles. The linear relationship between these numbers and the linear attenuation coefficient is the defining equation for the so-called Hounsfield units. This is given by

$$CT_i = k \frac{u_i - u_{\text{water}}}{u_{\text{water}}}$$

where  $CT_i$  is the calculated CT number in the  $i^{\text{th}}$  pixel,  $u_i$  is the effective linear attenuation coefficient for that pixel,  $u_{\text{water}}$  is the effective linear attenuation of water, and  $k$  is the proportionality constant which defines Hounsfield units (and thus calibrates the CT scanning apparatus) and should have the value 1000. On the Hounsfield scale, air has the value of -1000, water is 0, and bone is about 1000 and above. However, the constant of proportionality  $k$  is experimentally established by calibration of the CT scanning apparatus and may not be treated as a universal constant. It is effectively constant but not necessarily equal to 1000 for a given instrument.

The linear attenuation coefficient,  $u$ , strongly depends on the effective energy of the x-ray beam and the elemental composition of the material in the pixel. For a material of uniform composition, the linear attenuation coefficient is given by

$$\mu_i = \rho N \frac{Z}{A} (\sigma_R^e + \sigma_c^e + \sigma_{pe}^e)$$

where  $\rho$  is the density,  $N$  is Avagadro's number,  $Z$  the atomic number,  $A$  the atomic weight, and the  $\sigma$ 's are the scattering cross sections per electron for Rayleigh scattering, Compton scattering, and the photoelectric effect. The Compton cross section is mildly dependent upon the effective energy of the x-ray beam and independent of  $Z$ . The cross sections for Rayleigh and photoelectric scattering are strongly dependent on both energy and atomic number.

Determining calibration standards from materials with atomic numbers and densities similar to bone allows removal of the dependence on the Hounsfield scaling constant and the effective linear attenuation of water to give the relationship

$$\rho_i = CT_i A + B$$

The constants  $A$  and  $B$  depend on the measured CT numbers of the standards, the effective energy of the x-rays and on the ratios of the total electronic scattering cross sections for the measured and standard materials. This equation demonstrates a linear relationship between density and CT number in our region of interest.

The corresponding relationship between density and mechanical properties is well documented. Abendshein and Hyatt (1970) found a linear correlation ( $r = .94$ ) between wet density and modulus of elasticity for 52 specimens of human tibial and femoral cortical bone. Martin and Atkinson (1977) also determined a

linear relationship ( $r = .99$ ) between wet density and ultimate bending strength for 37 specimens of human femoral bone.

Evans (1973) studied embalmed human tibial, femoral and fibular specimens. For 70 tibial specimens, positive correlations at the .001 level of significance were found between dry density and ultimate tensile strength, modulus of elasticity and Rockwell hardness. At the .05 level of significance a correlation was found between dry density, single shear strength and Rockwell hardness. For 17 femoral specimens a correlation was only found between dry density and Rockwell hardness. This was attributed to the relatively small population studied.

In summary, since linear relationships exist between CT number and density and between density and mechanical properties a linear relationship between CT number and mechanical properties can be assumed. Thus, a local CT number minimum should indicate a local mechanical property minimum.

#### 3.2.4 Physical and Cross Sectional Data Collection and Reduction

Slides of the scans are back projected on the digitizer platen to determine bone cross-sectional properties. The bone perimeter is digitized and PROPS is utilized to perform the property calculations. The graphics capabilities of the Hewlett-Packard desktop computer are employed to plot these properties as a function of longitudinal bone position.

CT numbers are obtained using a PDP-15 image processing system and a line printer. A bone is displayed on the CRT and



location whose CT numbers are desired is selected. The numbers are then output to a line printer. Maximum values on the lateral, medial, posterior and anterior aspects of the bone are recorded. These values are also plotted as a function of longitudinal bone position.

### 3.3 Results

The long bones of a human and a baboon cadaver have been studied, 542 diaphyseal sections being evaluated. Complete physical and cross sectional properties are graphically presented in Appendix II. Unfortunately, complete CT number data on the human bones is not available since a scanner capable of differentiating between high bone densities was obtained only recently. For ease of comparison some selected properties of human and baboon humeri and femora are shown in Figures 16-19. Note that the data for the baboon is less irregular than that of the human since it was acquired at a later date and employed a new scanner with increased resolution and the smoothing and filtering techniques described in Section 3.2.2.

### 3.4 Discussion

Based on the number of specimens available, the following general observations are made. On the average, minimum cross sectional areas of human bones are 2.5 times greater than that of baboons, the difference being more pronounced in the lower extremities. Minimum inertial properties are approximately 5 times as great in man, again the difference being larger in the lower

Figure 16

Comparison of Human and Baboon Humeral Areas

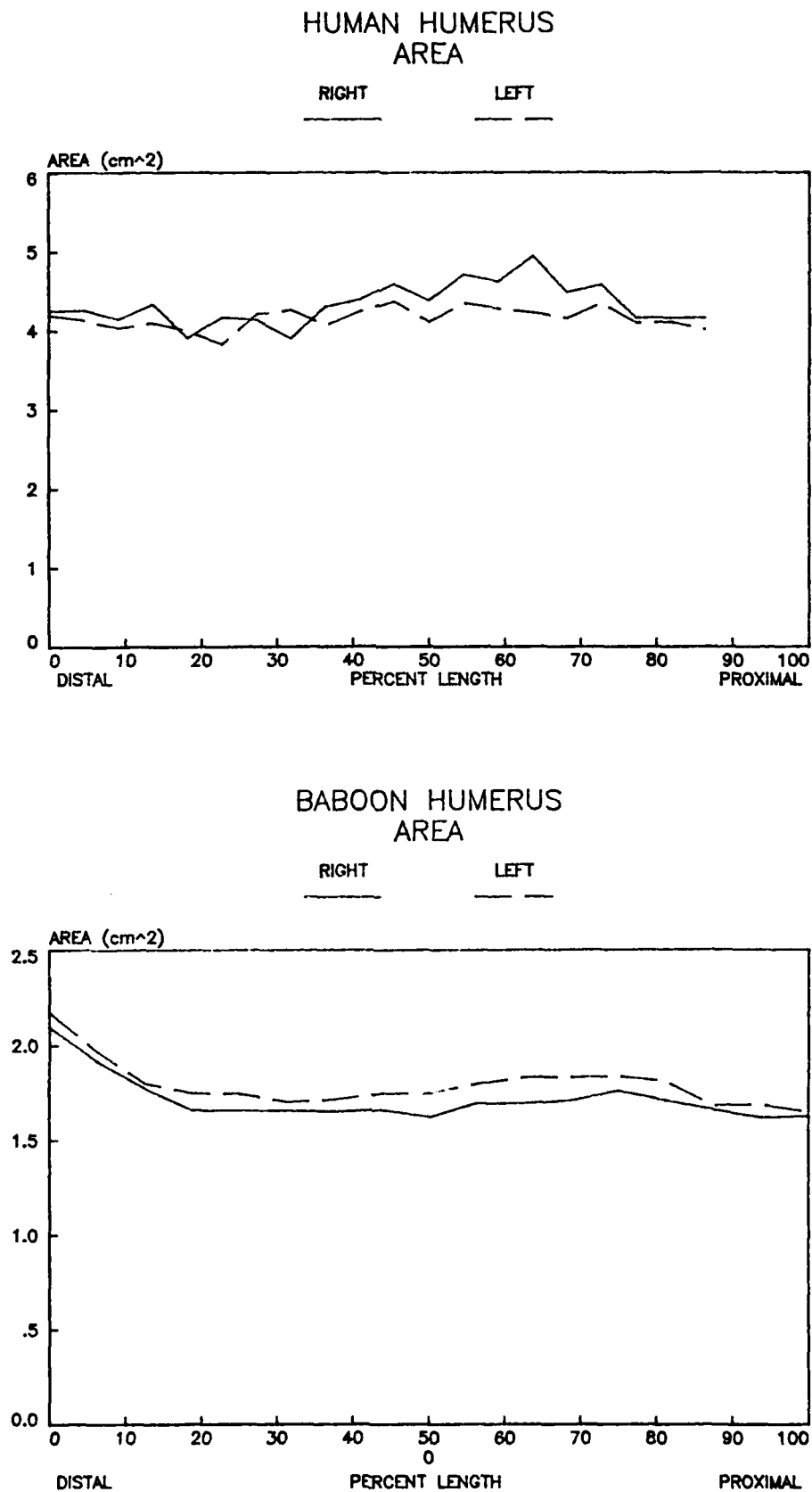


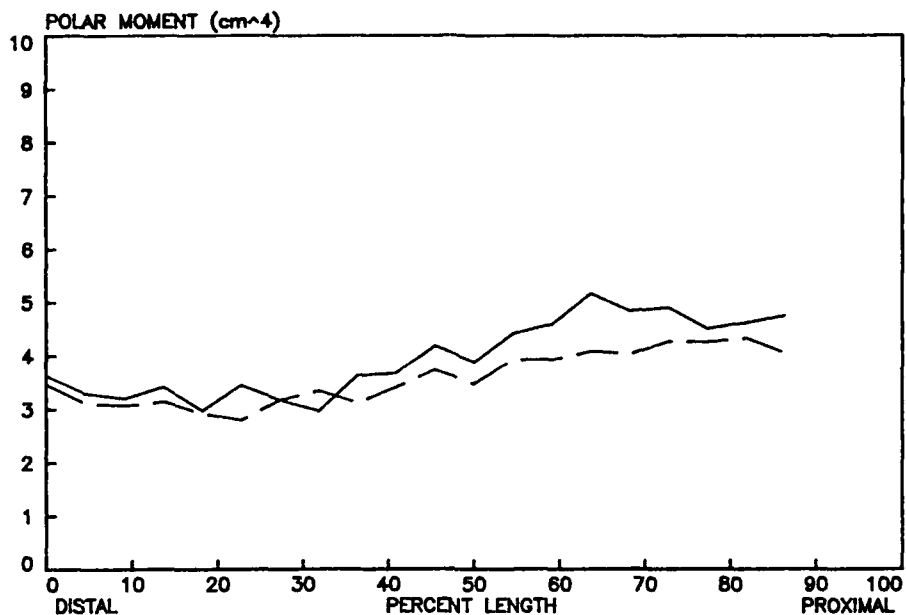
Figure 17

Comparison of Human and Baboon  
Humeral Polar Moments of Inertia

HUMAN HUMERUS  
POLAR MOMENT OF INERTIA

RIGHT

LEFT



BABOON HUMERUS  
POLAR MOMENT OF INERTIA

RIGHT

LEFT

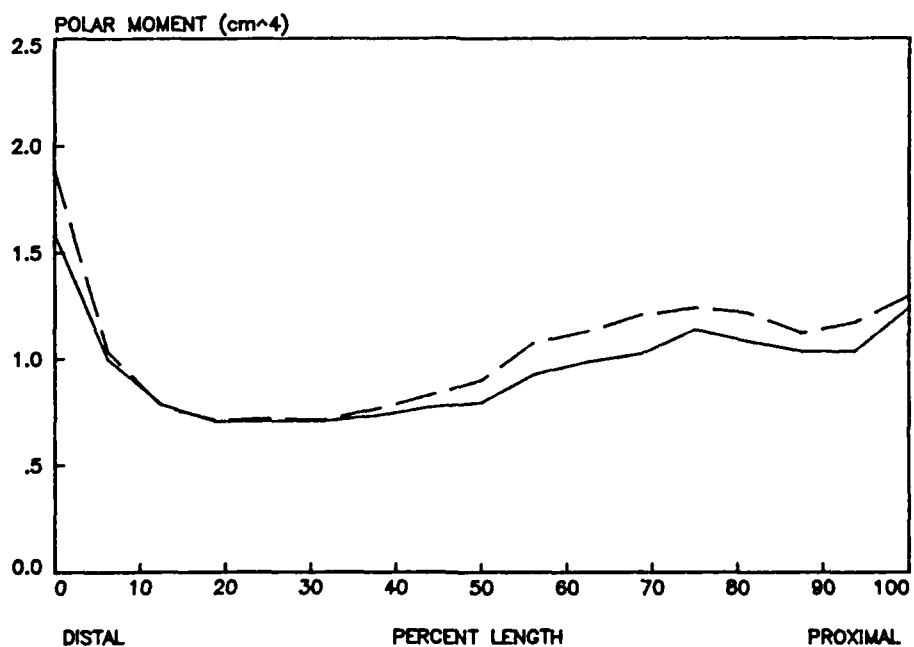


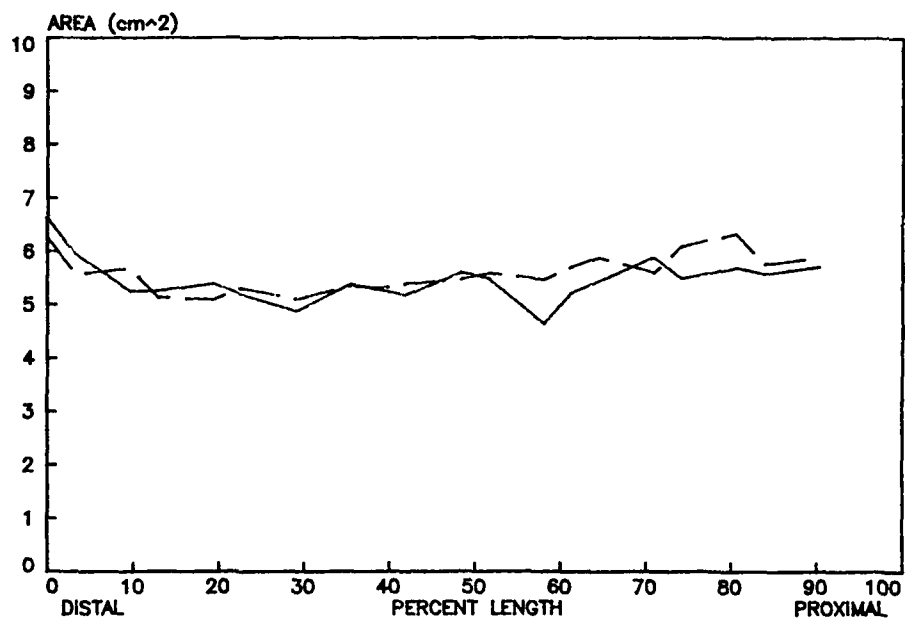
Figure 18

Comparison of Human and Baboon Femoral Areas

HUMAN FEMUR  
AREA

RIGHT

LEFT



BABOON FEMUR  
AREA

RIGHT

LEFT

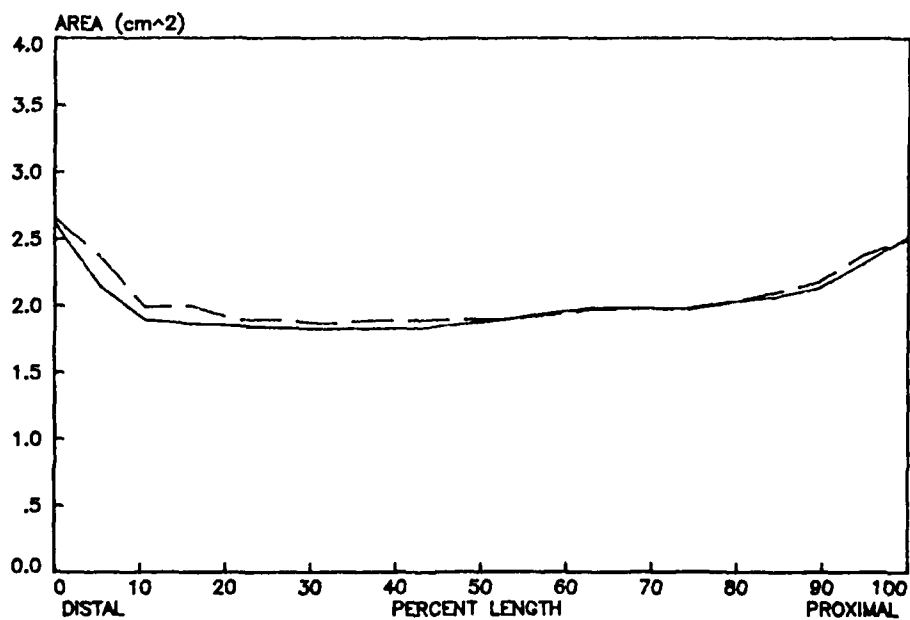
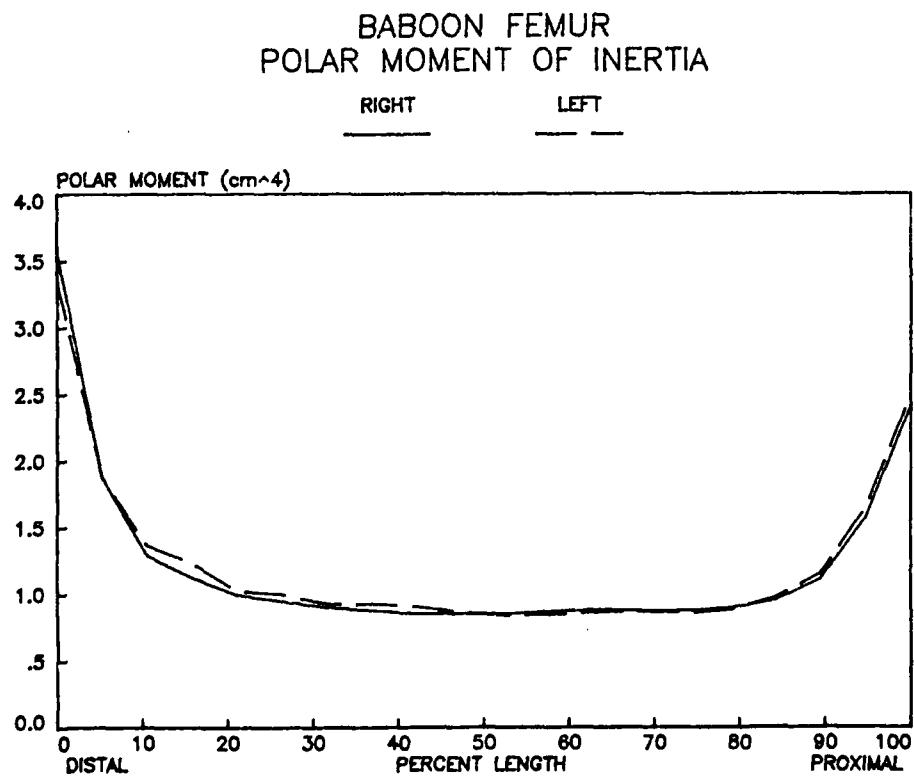
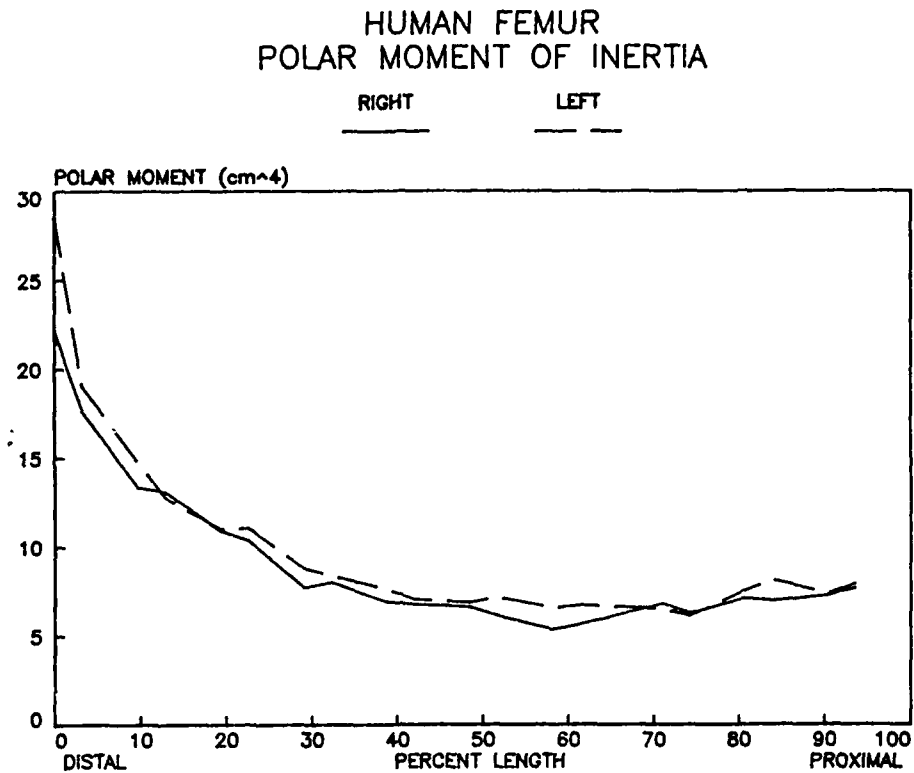


Figure 19  
Comparison of Human and Baboon  
Femoral Polar Moments of Inertia



extremities. This is probably due to the necessity of having increased bony development in the ape to complement its upper body strength. No left-right differences are apparent for man or baboon. In most instances cross sectional properties are at a minimum in the mid-shaft region and increase at the metaphyses.

An attempt was made to compare our cross sectional property results to previous work. Although many researchers have studied techniques to determine these properties, few have actually applied their methods and none have studied all of the skeletal long bones in such detail.

Piziali, Hight and Nagel (1976) presented data on four human tibiae which closely matches our results both in trend and magnitude. Miller and Purkey (1980) in a study of nine pairs of human tibiae, and Minns, Bremble and Campbell's (1975) study of four human tibiae presented similar results which are in general slightly lower in magnitude than the current study and that of Piziali et al. This is probably due to a slightly different interpretation of the location of the cortical-cancellous boundary. Since visual determination of this boundary is quite subjective, it is believed that our technique as illustrated in Figures 11-14a results in more consistent delineation.

CT numbers are generally greatest in the mid-shaft region where the anterior and medial portions are higher than those posterior and lateral. The femur and tibia have the highest CT numbers while the radius and fibula have the lowest. The low CT numbers for the fibula may be due to its small size and the resulting partial volume artifact. Little right-left difference is apparent.

#### IV. CORRELATION AND UTILIZATION

##### 4.1 Relation Between Loading Rate and Cross Sectional Property Studies

To determine the relevance of the studies which have been undertaken, a further experiment was performed. Two specific questions were addressed. First, how do mechanical and cross sectional properties relate to fracture site location, and secondly, what interspecies variables might affect the outcome of the loading rate experiments?

Since the mechanical and cross sectional property evaluation technique is non-destructive, the scanned baboon bones were available for testing. Following procedures outlined in Section 2.2.1 the paired baboon radii were loaded to failure in torsion at loading rates of .053 and 26.7 rpm (Figure 20).

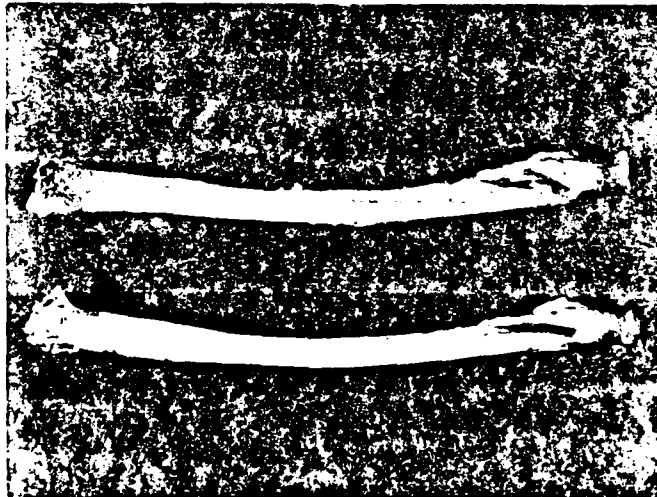


Figure 20

Baboon Radii Fractured at .053 (top) and 26.7 (bottom)  
revolutions per minute

The non-dimensional quantities  $\bar{T}$  and  $\bar{E}$  were calculated to be 1.36 and 1.96, respectively.  $\bar{T}$  agreed quite well (3% difference) with the average value of 1.32 for the canine radii.  $\bar{E}$  was higher than the canine average of 1.40 but much more scatter is experienced in the energy data. The difference in  $\bar{E}$  is mainly accounted for by a large angle of twist. Like the canine radii fracture occurred at the same location on the proximal end of the bone and was not shifted by changing the loading rate. It is difficult to draw a conclusion based on this experiment alone but it appears that it may be possible to draw a direct or scaled correlation between species.

Figure 21 shows the location of the fracture site in relation to CT numbers and polar moment of inertia. It can be seen that the fracture zone occurs at a point of minimum polar moment of inertia.

Coincidentally, the left baboon fibula showed evidence of a fracture in the process of healing. This is demonstrated by the callus formation shown on the baboon fibula cross sectional property graphs in Appendix II. Figure 22 shows a comparison of polar moment of inertia and the CT numbers of the normal (right) fibula. Polar moment of inertia is fairly constant along the length but at the fracture location a CT number minimum exists on the posterior surface of the bone. It appears that polar moment of inertia controlled the fracture site location on the radius but CT number controlled the location on the fibula, assuming that the primary fibular load was torsion.



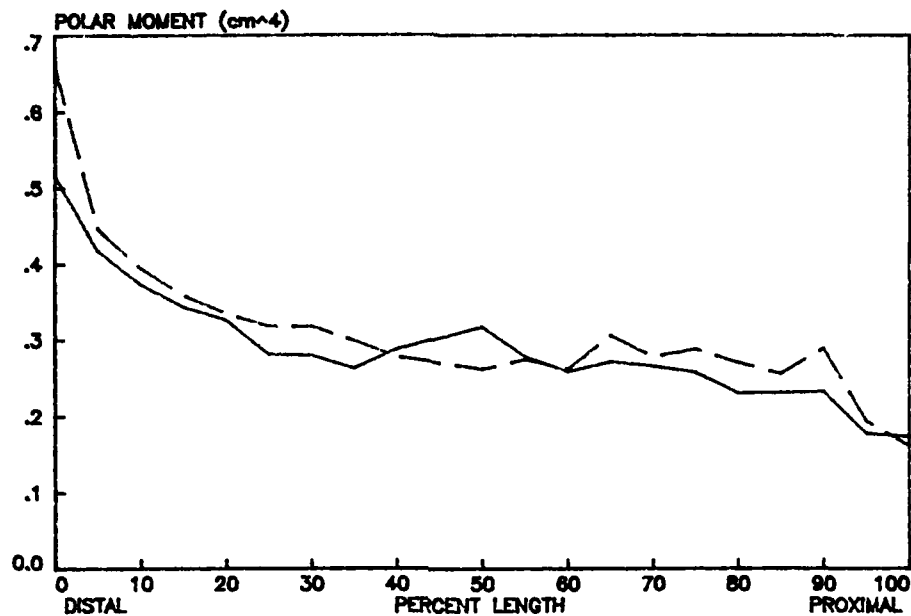
Figure 21

Fracture of the Baboon Radius Occurred  
Between 80% and 100% of the Scanned Length

BABOON RADIUS  
POLAR MOMENT OF INERTIA

RIGHT

LEFT



LEFT BABOON RADIUS  
CT NUMBER

ANTERIOR

MEDIAL

POSTERIOR

LATERAL

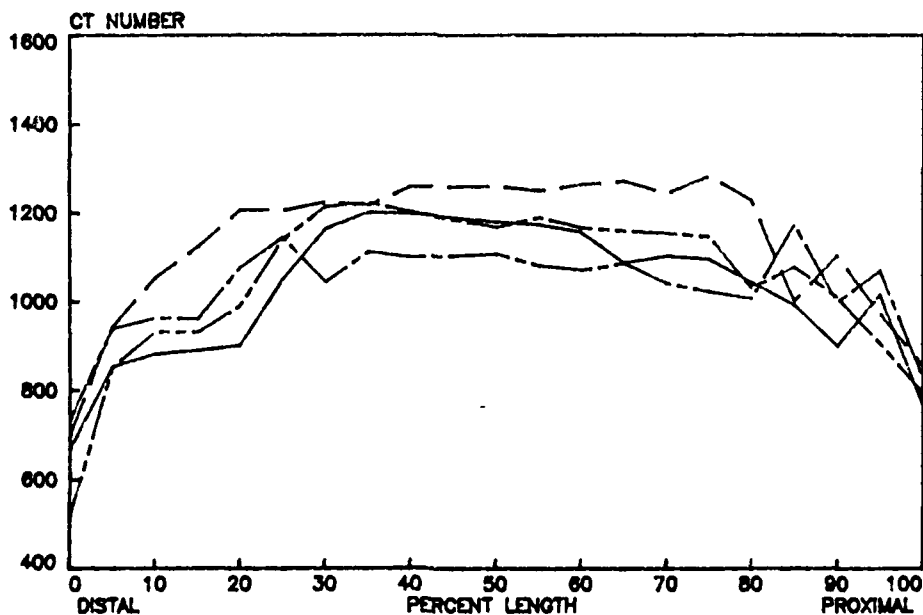
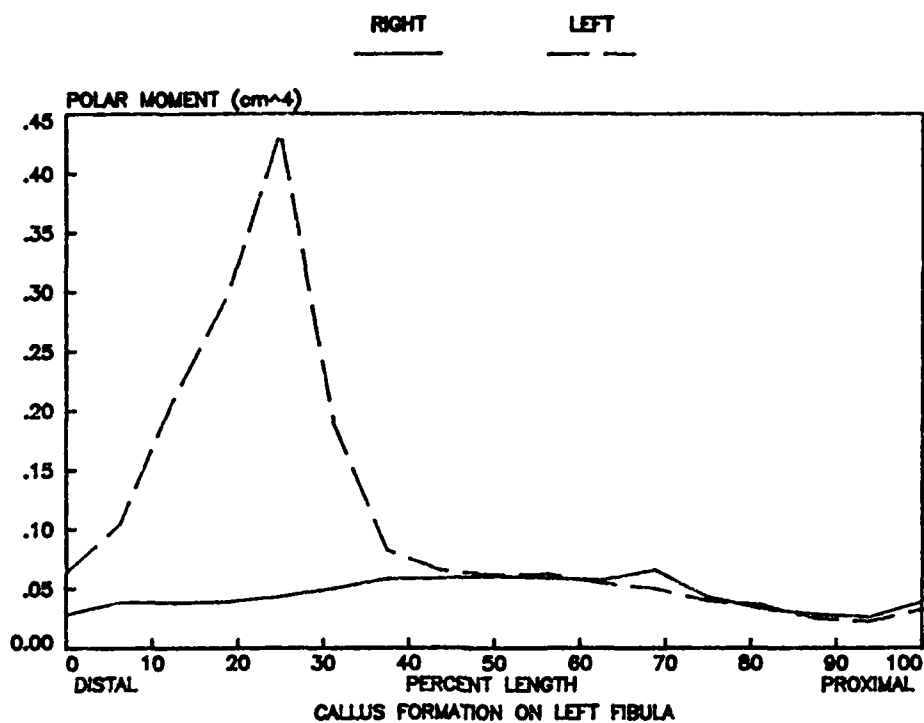


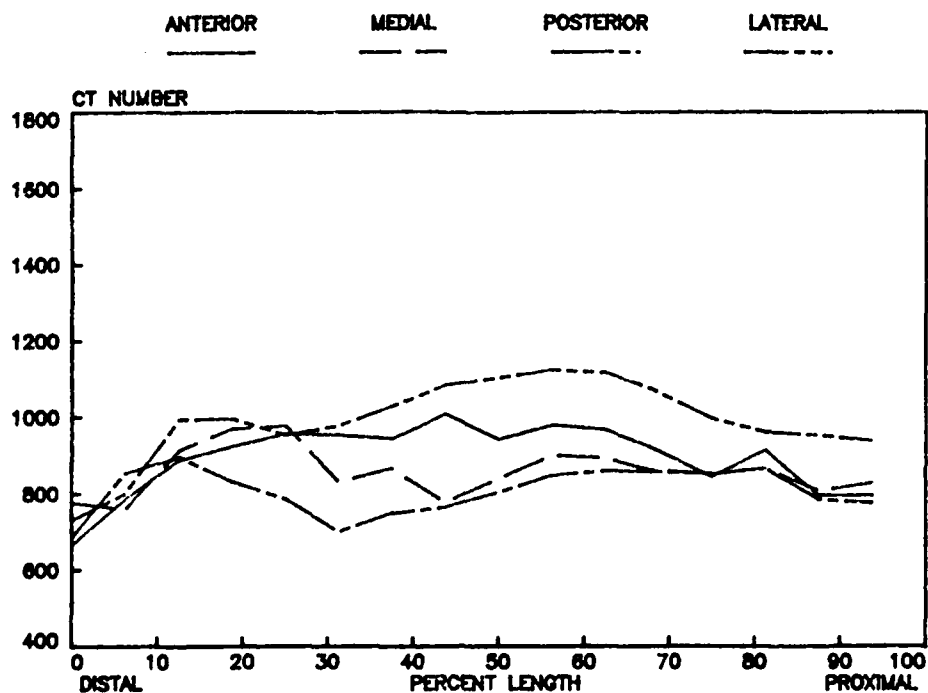
Figure 22

Callus Formation Indicating the Location of a Fracture

BABOON FIBULA  
POLAR MOMENT OF INERTIA



RIGHT BABOON FIBULA  
CT NUMBER



This implies that for a given bone and loading state mechanical or cross sectional properties or both may be determinants of failure.

The combined effect might be determined by means of a "Fracture Score" which quantifies the relative magnitude of cross sectional and material strength. For example, in the most basic form, by assigning a value of one to the maximum polar moment of inertia ( $J_{\max}$ ) and average maximum CT number ( $CT_{\max}$ ) and a value of zero to the minima of these parameters ( $J_{\min}$ ,  $CT_{\min}$ ), the Fracture Score (FS) at any point x along a bone in torsion might be computed by:

$$FS = \frac{1}{2} \left[ \frac{J_x - J_{\min} + CT_x - CT_{\min}}{J_{\max} - J_{\min} \quad CT_{\max} - CT_{\min}} \right]$$

FS would have a value of 1 if x corresponded to a point of maximum CT number and polar moment and 0 if it corresponded to a point of minimum CT number and polar moment. Using this scheme FS was calculated for the left baboon radius in Figure 21 and plotted (Figure 23). This indicates the probability of fracture in torsion at the proximal end which did, in fact, occur.

The preceeding example was done for illustration and could only be adopted for use if proven by comparison with much more experimental data. Fracture Score may have to accommodate different combinations of variables for various loading states and may have to be weighted in some manner. However, it is believed the utility of the concept has been demonstrated.

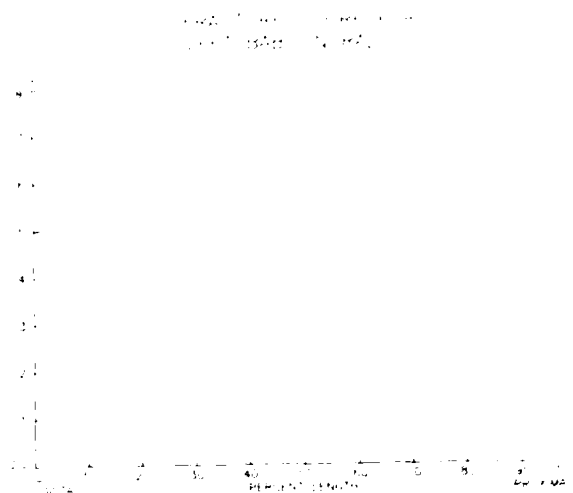


Figure 23

Tabulation of a Candidate Fracture Score  
for the Baboon Radius of Figure 21

## 4.2 Modelling

### 4.2.1 The Canine Fracture Model

The canine radius was chosen for the loading rate studies since it is easily mounted and a large number of fresh paired bones were available. The primate extremities that were obtained sometimes were not paired or had been damaged during dissection. It was felt that since the tests result in non-dimensional data they determine the behavior of bone tissue and the data might be correlated to other species. This was demonstrated by fracture of the paired baboon radii as described in Section 4.1. The baboon bones fractured in the same location as the canine bones and  $\bar{T}$  was in close agreement.  $\bar{E}$  was

considerably larger for the baboon, but the energy data experiences much more scatter (Figures 4 and 5).

In an interesting related study, Strongwater, Goel, Panjabi, and Drinker (1980) investigated the anatomical similarity of human, baboon, dog, and sheep femora. They noted a greater external similarity between dogs and humans and greater internal similarity between baboons and humans. They concluded that either dogs or baboons are suitable implant models, but due to cost, availability, and ease of handling, the dog may be more attractive.

By their nature, biological structures are considerably more variable than engineering structures, both in geometry and composition. This necessitates the evaluation of large sample populations to draw statistically significant conclusions. Specimen availability is of primary importance.

#### 4.2.2 Utilization of Computed Tomography in Modelling

One of the more obvious uses of the computed tomography derived data is in the development of long bone models. These models may be used for long bone fracture studies or in the design of orthopaedic appliances. More advanced models would undoubtedly employ the finite element method. The techniques which have been developed in this contract could readily be adapted to pre-processing of the geometric input necessary for a 3-D long bone model. This is generally the most time consuming and expensive stage of the procedure. Another application

might be the determination of body segment distributed mass properties. If the volume (slice thickness x pixel area) and density of a pixel are known, then the mass of the pixel can be computed. The sum of all these masses would equal the mass of the whole object. This would not require a major programming effort since the scan information may be thought of as stored in a 3 dimensional array where each element is the CT number of a known pixel volume within the object. When a direct conversion from CT number to density has been derived it is intended to test this method by predicting the weight of a bone which has been scanned.

#### 4.3 Relation to Windflail Injury

Current knowledge of the loads to which the human musculoskeletal system is exposed in normal activity is limited. State-of-the-art techniques to obtain this information generally combine a controlled laboratory simulation of the activity and theoretical analysis. Results vary among investigators even under these conditions. The difficulties involved in determining the loading state acting on a human body during ejection from an aircraft can therefore be appreciated.

The first ejection injury occurred over 36 years ago (Fleming, 1979). However, due to its complex nature, the loading environment remains largely undefined. Schneck (1979) calculated dislodging force for a forearm on a restraining surface at an altitude of 10,000 feet and various angles of attack. He

determined that dislodgment would occur at approximately 450 knots since the average grip retention strength of 270 kg is exceeded. This agrees well with Combs' study (1977) of severe (windflail) and minor ejection injuries. Minor injuries occurred at an average of 310 knots while the windflail injuries occurred at an average of 403 knots. Two mid-shaft comminuted fractures of the femur were reported. The cross sectional property data (Appendix II) for the human femur is at a minimum between 50-60% of the scanned length. Additionally, five proximal humerus fractures were reported. The cross sectional properties determined in our study remained constant along the length, but density data, when available, might reveal the reason for the proximal fractures.

Comparison of fractures produced under known loading environments to those produced during ejection may be the most practical method to determine a lower bound on ejection forces and moments.

## V. SUMMARY

The following outlines the primary results of studies performed in this contract.

- 1) For canine radii in pure torsion, increased loading rate produced increased torque and energy to fracture. However, at the high end of our available loading regime a drop in these parameters was noted.
- 2) For canine radii loaded in torsion and compression similar behavior was experienced with the exception that torque and energy to fracture had slightly larger magnitudes.
- 3) The removal of cancellous bone was found not to have as statistically significant effect on torque and energy to fracture or an effect on fracture site location.
- 4) A technique to non-destructively evaluate cross-sectional and physical properties of long bones has been developed.
- 5) This technique has been used to analyze the long bones of a human and a baboon cadaver.
- 6) Physical and cross sectional properties for a pair of baboon radii have been related to an experimentally produced fracture.
- 7) The utilization of this data and its correlation to in vivo fracture situations has been discussed.



## VI. RECOMMENDATIONS

This section briefly describes projected efforts that represent logical extensions of the work performed in this contract. The curves presented in Section II should be extended using a materials testing system capable of loading rates higher than those obtainable with the Instron. It would also be interesting to apply a greater compressive load to exaggerate the effect of a combined axial and torsional state on fracture behavior. Using stress analysis techniques a model could be developed to predict the angle of fracture and to explain why a more complex loading state produces increased magnitudes for torque and energy. Additional specimens should be tested to better define the role of cancellous bone in energy absorption.

The efforts described in Section III and IV should be continued and expanded. Specifically, the cross sectional and physical properties of an increased number of human and animal bone specimens should be determined to examine variations within species. Also, a pair of canine radii should be scanned to determine the reason for consistent fracture at the proximal end of the bone as described in Section II. The relationship between CT number and density must be derived explicitly and verified. Correlation of in vivo and in vitro fracture sites with cross sectional and mechanical properties should be continued.

## VII. REFERENCES

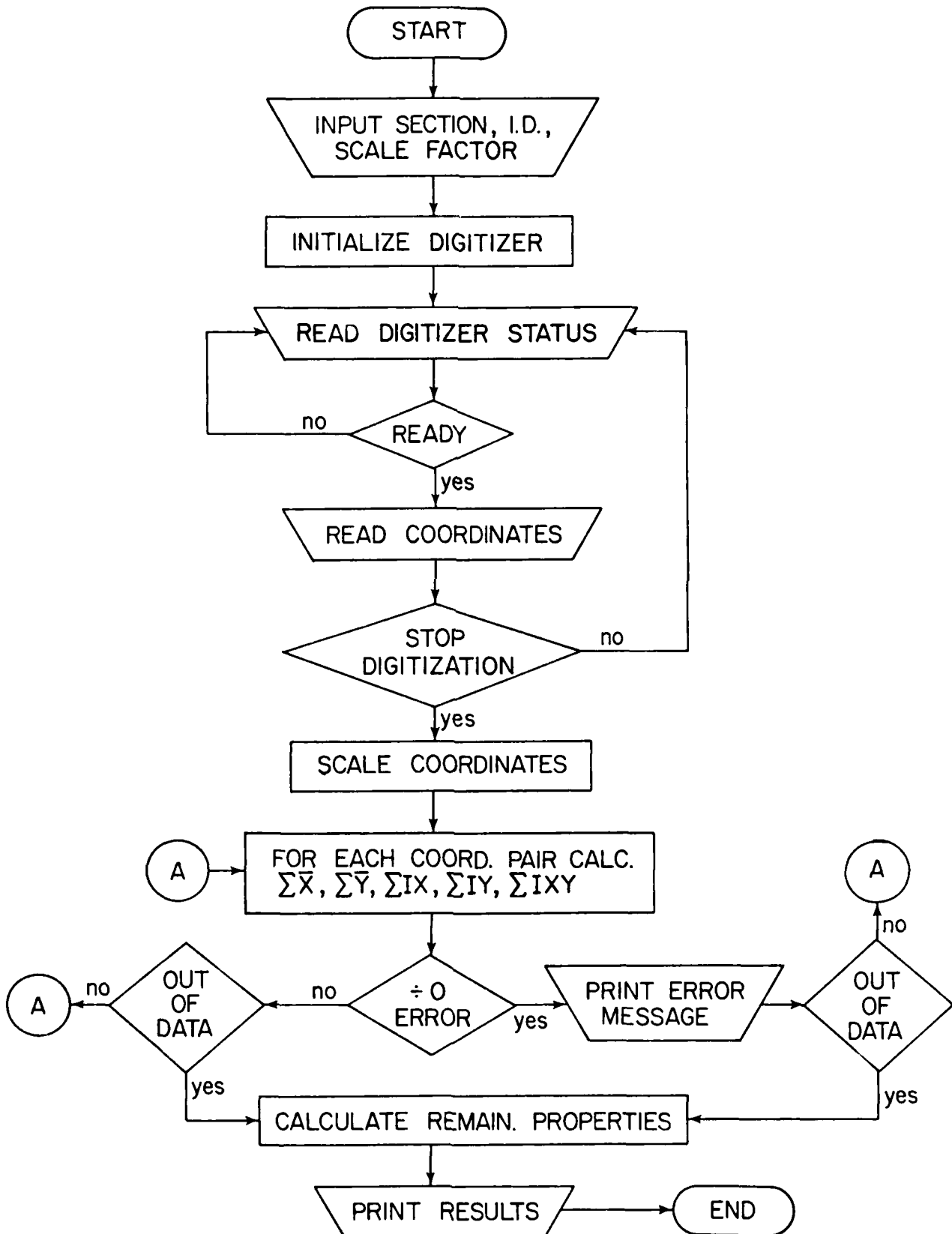
1. Abendshein, W. and Hyatt, G.W.: Ultrasonics and selected physical properties of bone. Clin. Orthop. 69:294-301, 1970.
2. Berry, J.L., Corn, R.C., and Greenwald, A.S.: A technique employing graduated flexible reamers prior to intramedullary fixation of long-bone fractures. Veterinary Medicine & Small Animal Clinician, 73(9):1523-24, 1978.
3. Burstein, A.H. and Frankel, V.H.: The viscoelastic properties of some biological materials. Ann N.Y. Acad. of Sciences, 146:158-165, 1968.
4. Combs, S.P.: Correlation of mechanism of extremity injury and aerodynamic factors in ejections from F-4 aircraft. A.G.A.R.D. Conference Proceedings No. 253.
5. Ducheyne, P., Maartens, M. and DeMeester, P.: Microscopic fracture aspects of impact tested human bones. J. Bioeng., 1(13):197-207, 1977.
6. Evans, F.G.: Stress and strain in bones: their relation to fractures and osteogenesis. Springfield, Charles C. Thomas, 1957.
7. Evans, F.G.: Stress and strain in the long bones of the lower extremity. In Instructional Course Lectures, the American Academy of Orthopaedic Surgeons, 9:264-271. Ann Arbor, J.W. Edwards, 1952.
8. Fleming, C.: Ejection problems and injuries: their causes, effects, treatments, and suggestions for preventative measures. Aviat. Space Environ. Med., 50(8):829-833, 1979.
9. Fryer, D.I.: Operational experience with British seats, a survey of medical aspects. Flying Personnel Research Committee, FPRC/1166, 1961.
10. Lovejoy, C.O., and Barton, T.J.: A simple, rapid method of obtaining geometrical properties from sections or laminograms of long bones. J. Biomechanics, 13:65-67, 1980.
11. Lovejoy, C.O., and Burstein, A.H.: Geometrical properties of bone asections determined by laminography and physical section. J. Biomechanics, 10:527-528, 1977.
12. Martens, M., VanAudekercke, R., DeMeester, P., Mulier, J.C.: The mechanical characteristics of the long bones of the lower extremity in torsional loading. J. Biomechanics, 13:667-76, 1980.

13. Martin, R.B. and Atkinson, P.J.: Age and sex related changes in the structure and strength of the human femoral shaft. J. Biomechanics, 10:223-231, 1977.
14. McElhaney, J.H. and Byars, E.F.: Dynamic response of biological materials. ASME 65 WA/HUF-9, 1965.
15. Miller, G.J., and Piotrowski, G.: A brief note on the variability of the torsional strength of paired bones. J. Biomechanics, 7:247-248, 1974.
16. Miller, G.J., and Purkey, W.W.: The geometric properties of paired human tibiae. J. Biomechanics, 13:1-8, 1980.
17. Minns, R.J., Bremble, G.R., and Campbell, J.: The geometrical properties of the human tibia. J. Biomechanics, 8:253-255, 1975.
18. Nagurka, M.L., and Hayes, W.C.: An interactive graphics package for calculating cross-sectional properties of complex shapes. J. Biomechanics, 13:56-64, 1980.
19. Panjabi, M.M., White, III, A.H., and Southwick, W.O.: Mechanical properties of bone as a function of rate of deformation. J. Bone and Joint Surg., 55-A(2):322-330, 1973.
20. Payne, P.R., and Hawker, F.W.: USAF experience of flail injury for non-combat ejections in the period 1964-1970, AMRL-TR-72-11, Aerospace Medical Research Laboratory, AMD, AFSC, USAF, 1974.
21. Piekarski, K.: Fracture of bone. J. of Applied Physics, 41(1):215-223, 1970.
22. Piziali, R.L. and Hight, T.K.: Dynamic structural analysis of the human tibia. Proc. of the 22nd O.R.S., 3, 1976.
23. Piziali, R.L., Hight, T.K., and Nagel, D.A.: An extended structural analysis of long bones - application to the human tibia. J. Biomechanics, 9:695-701, 1976.
24. Sammarco, G.J., Burstein, A.H., Davis, W.L., and Frankel, V.H.: The biomechanics of torsional fractures; the effect of loading on ultimate properties. J. Biomechanics, 4:113-117, 1971.
25. Schneck, D.J.: Aerodynamic forces exerted on an articulated body subjected to windblast. Technical Report AMRL-TR-76-109, December, 1976, Wright-Patterson Air Force Base, Ohio.

26. Schneck, D.J.: Studies of limb-dislodging forces acting on an ejection seat occupant. Technical Report AMRL-TR-78-103, January, 1979, Wright-Patterson Air Force Base, Ohio.
27. Sedlin, E.D., and Hirsh, C.; Factors affecting the determination of the physical properties of femoral cortical bone. Acta Orthop. Scandinavica, 37:29-48, 1966.
28. Strongwater, A.R., Goel, V.K., Panjabi, M.M., and Drinker, H.: Quantitative anatomical comparison of human, baboon, dog, and sheep femora: suitability for implant fixation studies. Proc. of 4th Am Soc. of Biomec., 1980.
29. Wojciechowski, F.: Properties of plane cross-sections. Machine Design, 48:105-109, 1976.
30. Wright, T.M. and Hayes, W.C.: Tensile testing of bone over a wide range of strain rates: effects of strain rate, microstructure and density. Med. and Bio. Engineering, 14:671-79, 1976.

VIII. APPENDIX I

# "PROPS" FLOW CHART



# FUNDAMENTAL EQUATIONS

$$A = - \sum_{i=0}^n (y_{i+1} - y_i)(x_{i+1} + x_i)/2$$

$$\bar{x} = \frac{-1}{A} \sum_{i=0}^n [(y_{i+1} - y_i)/8] [x_{i+1} + x_i]^2 + (x_{i+1} - x_i)^2/3]$$

$$\bar{y} = \frac{1}{A} \sum_{i=0}^n [(x_{i+1} - x_i)/8] [(y_{i+1} + y_i)^2 + (y_{i+1} - y_i)^2/3]$$

$$I_x = \sum_{i=0}^n [(x_{i+1} - x_i)(y_{i+1} + y_i)/24] [(y_{i+1} + y_i)^2 + (y_{i+1} - y_i)^2]$$

$$I_y = - \sum_{i=0}^n [(y_{i+1} - y_i)(x_{i+1} + x_i)/24] [(x_{i+1} + x_i)^2 + (x_{i+1} - x_i)^2]$$

$$I_{xy} = \sum_{i=0}^n \frac{1}{(x_{i+1} - x_i)} \left[ \frac{1}{8}(y_{i+1} - y_i)^2(x_{i+1} + x_i)(x_{i+1}^2 + x_i^2) \right.$$

$$+ \frac{1}{3}(y_{i+1} - y_i)(x_{i+1}y_i - x_iy_{i+1})(x_{i+1}^2 + x_{i+1}x_i + x_i^2)$$

$$\left. + \frac{1}{4}(x_{i+1}y_i - x_iy_{i+1})^2(x_{i+1} + x_i) \right]$$

$$I_{\bar{x}} = I_x - A\bar{y}^2$$

$$I_{\overline{y}} = I_y - A\overline{x}^2$$

$$I_{\overline{xy}} = I_{xy} - A\overline{x}\overline{y}$$

$$\phi = \frac{1}{2} \tan^{-1} \frac{-2I_{\overline{xy}}}{I_{\overline{x}} - I_{\overline{y}}}$$

$$I_x' = I_{\overline{x}} \cos^2 \phi + I_{\overline{y}} \sin^2 \phi - I_{\overline{xy}} \sin 2\phi$$

$$I_y' = I_{\overline{y}} \cos^2 \phi + I_{\overline{x}} \sin^2 \phi + I_{\overline{xy}} \sin 2\phi$$

$$J = I_x' + I_y'$$

$$I_{xy}' = \frac{(I_{\overline{x}} - I_{\overline{y}})}{2} \sin 2\phi + I_{\overline{xy}} \cos 2\phi$$

where:

$x_{i+1}$  = x coordinate of current point

$x_i$  = x coordinate of previous point

$y_{i+1}$  = y coordinate of current point

$y_i$  = y coordinate of previous point

A = Area



$\bar{x}$  = x coordinate of centroid

$\bar{y}$  = y coordinate of centroid

$I_x$  = moment of inertia about the x-axis

$I_y$  = moment of inertia about the y-axis

$I_{\bar{x}}$  = moment of inertia about the x-centroidal axis

$I_{\bar{y}}$  = moment of inertia about the y-centroidal axis

$I_{x'}$  = moment of inertia about the principal x-axis

$I_{y'}$  = moment of inertia about the principal y-axis

$I_{xy}$  = product of inertia

$I_{\bar{xy}}$  = product of inertia about the centroidal axis

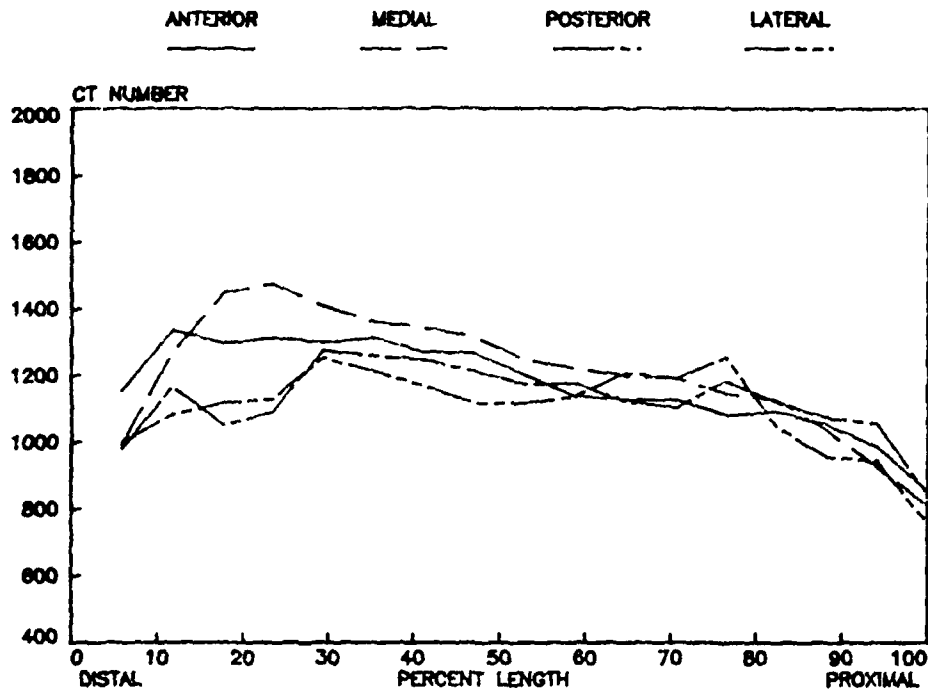
$\phi$  = angle between the translated centroidal axis and the principal axis

$J$  = polar moment of inertia

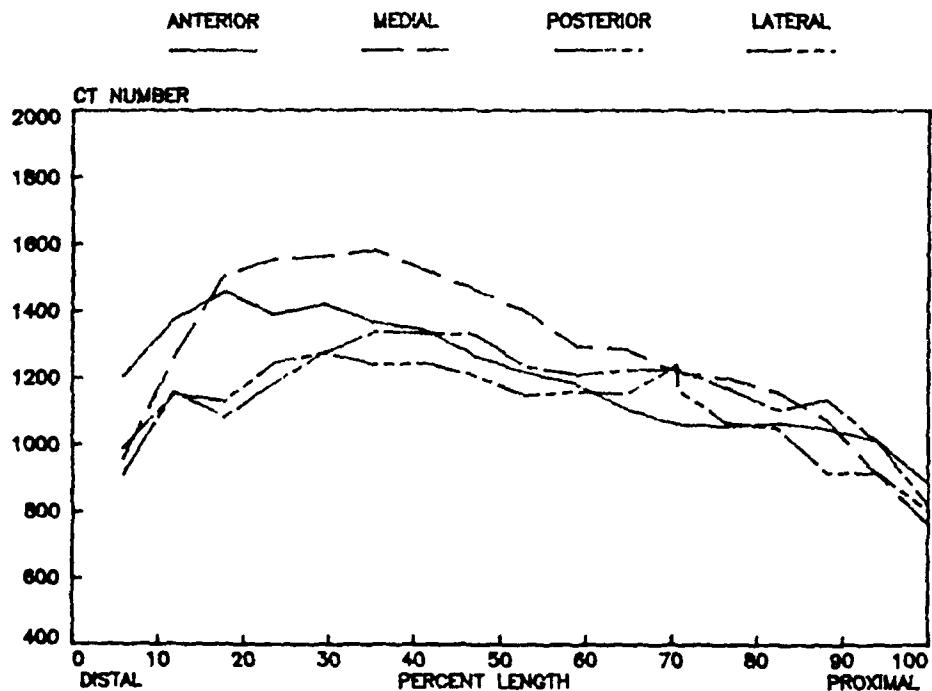
$n$  = total number of coordinate pairs

IX. APPENDIX II

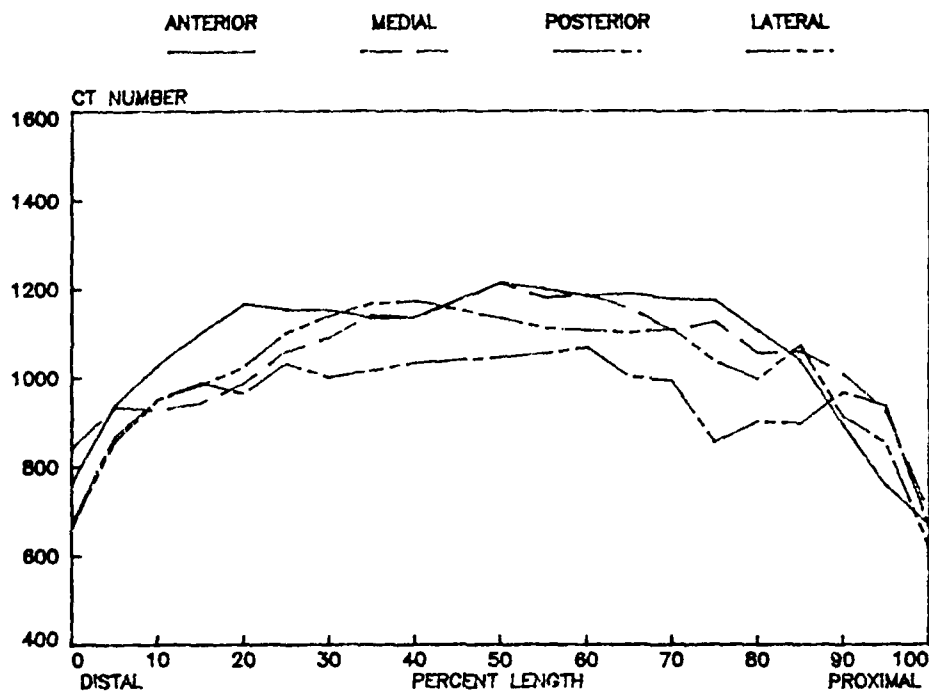
# RIGHT BABOON HUMERUS CT NUMBER



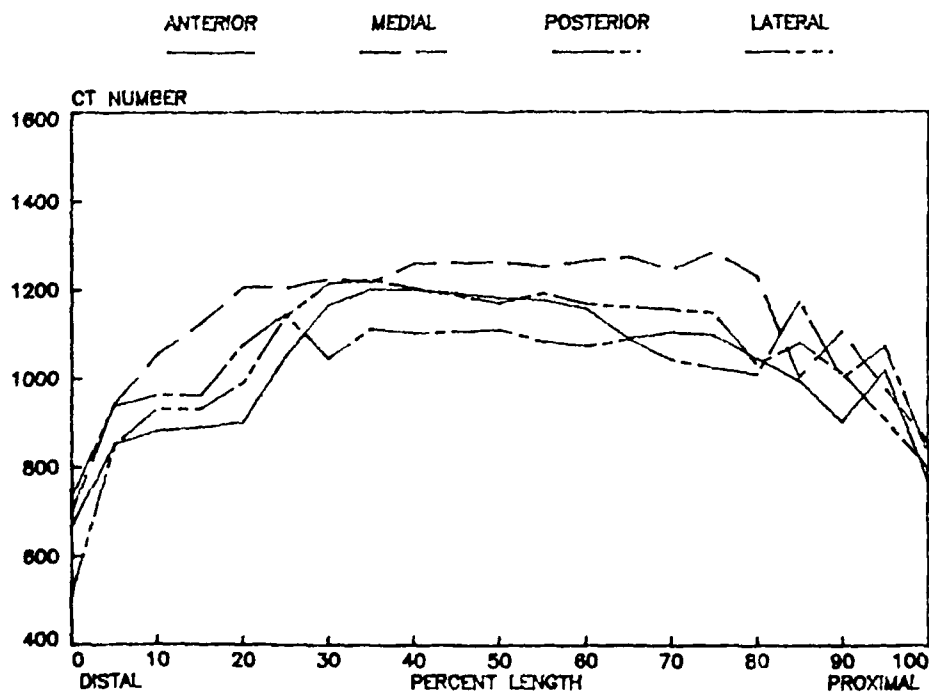
# LEFT BABOON HUMERUS CT NUMBER



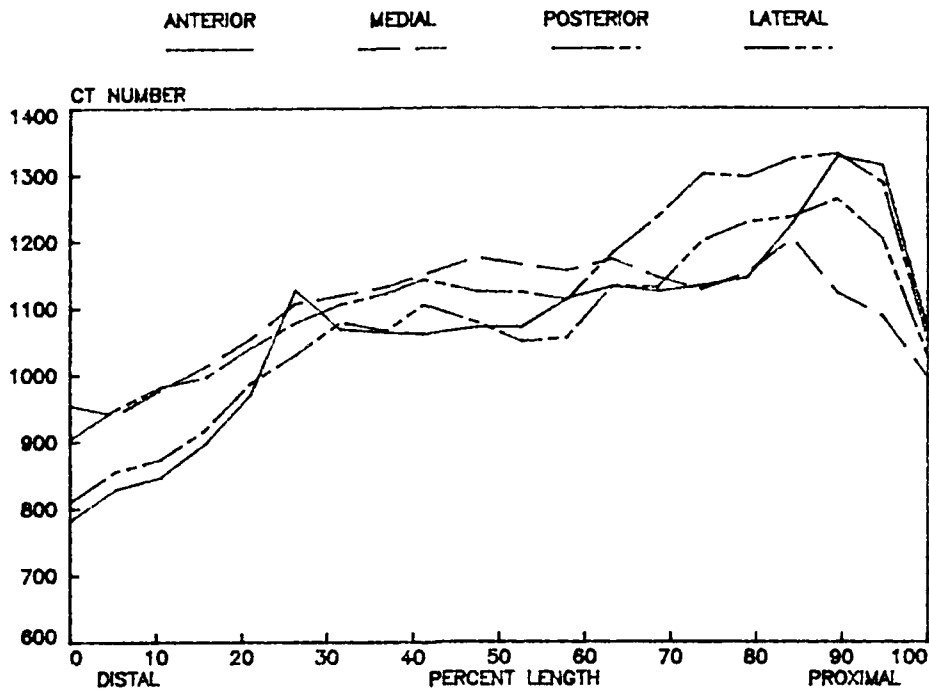
# RIGHT BABOON RADIUS CT NUMBER



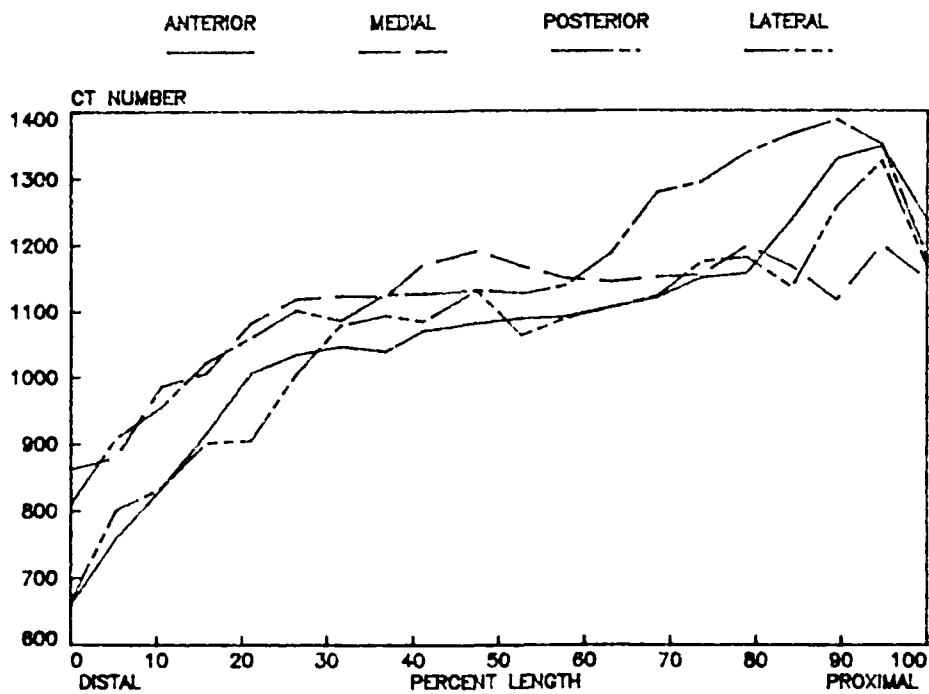
# LEFT BABOON RADIUS CT NUMBER



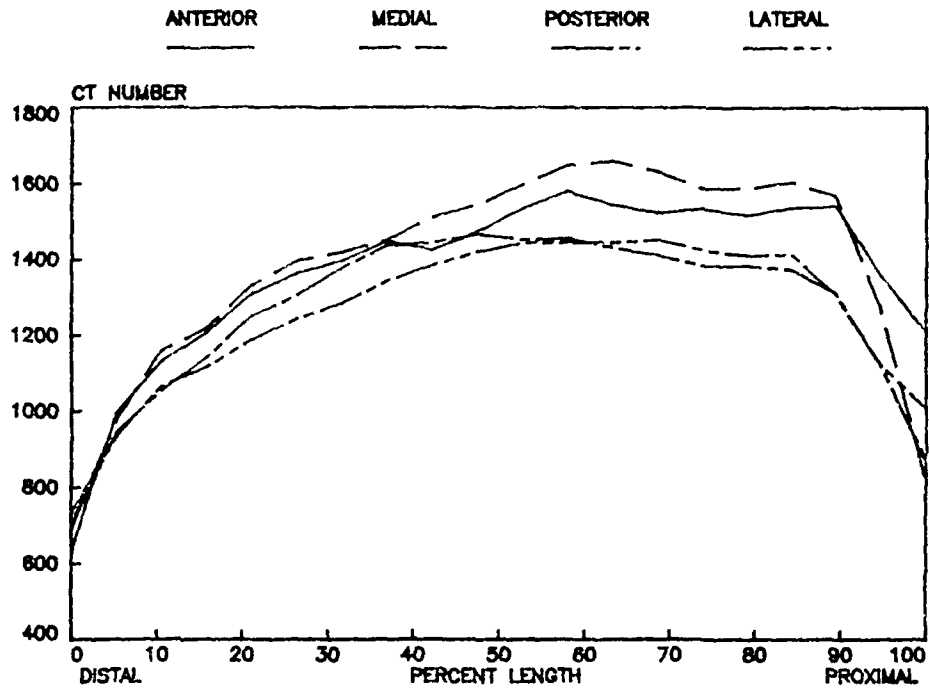
# RIGHT BABOON ULNA CT NUMBER



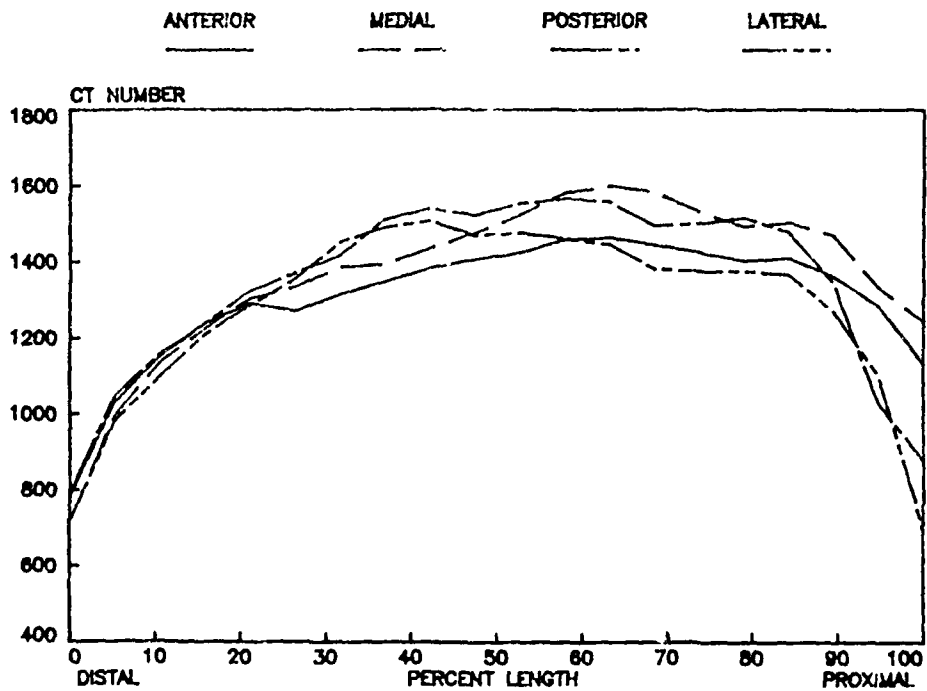
# LEFT BABOON ULNA CT NUMBER



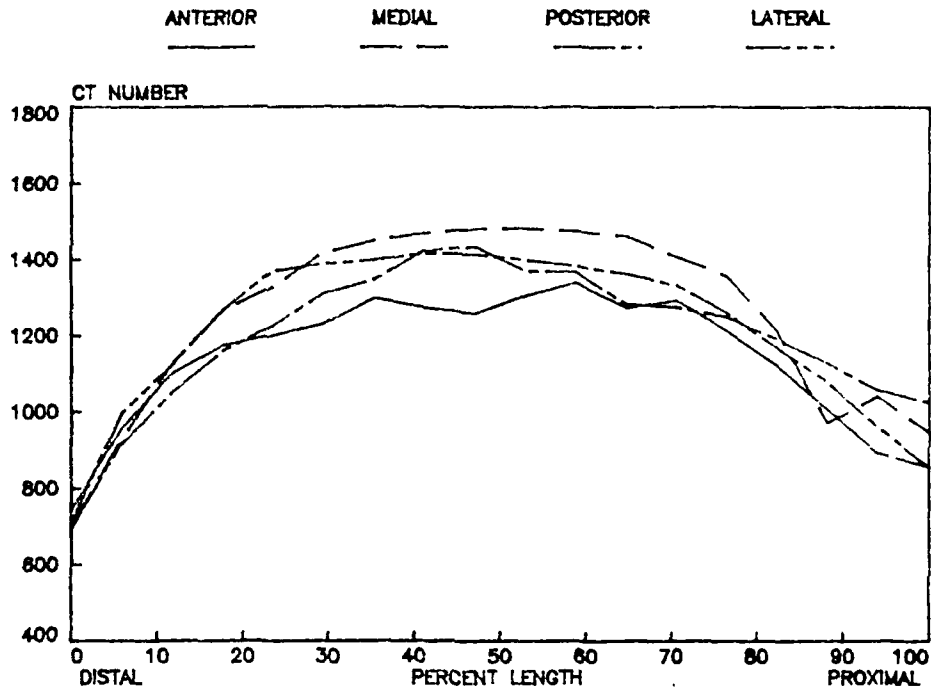
# RIGHT BABOON FEMUR CT NUMBER



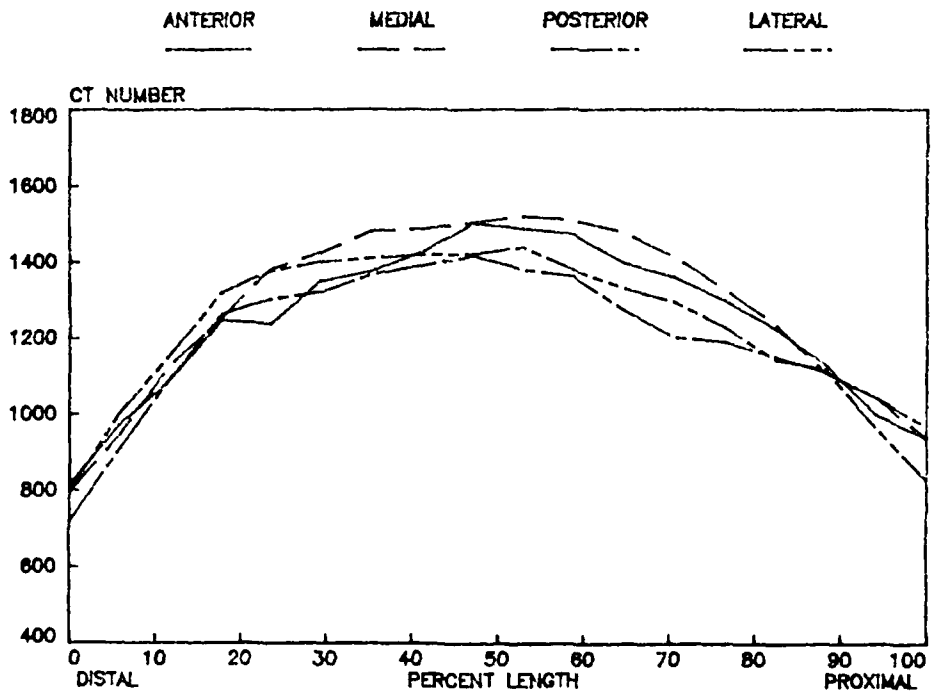
# LEFT BABOON FEMUR CT NUMBER



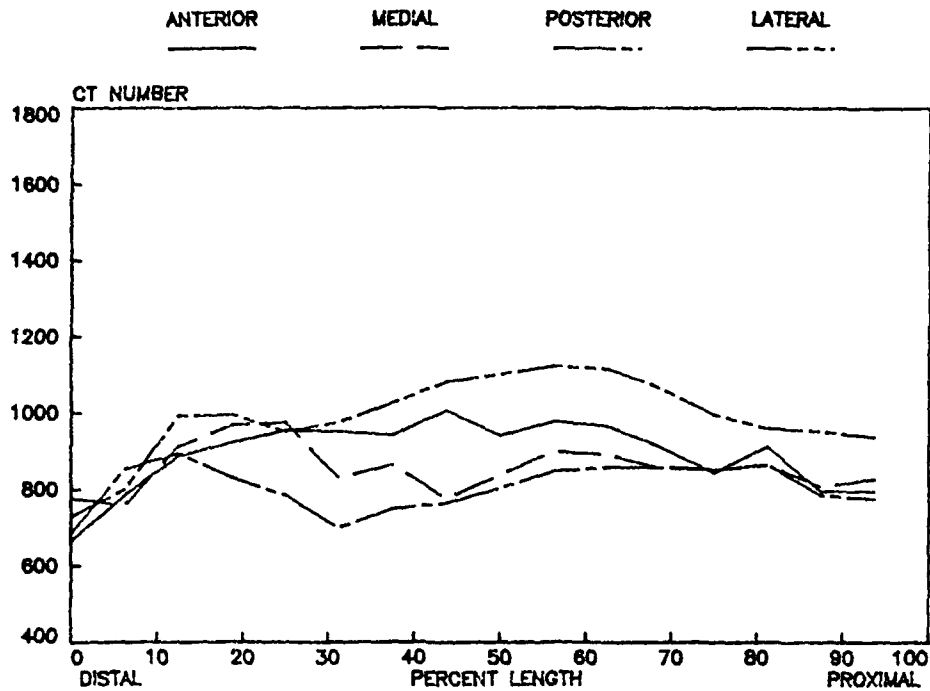
# RIGHT BABOON TIBIA CT NUMBER



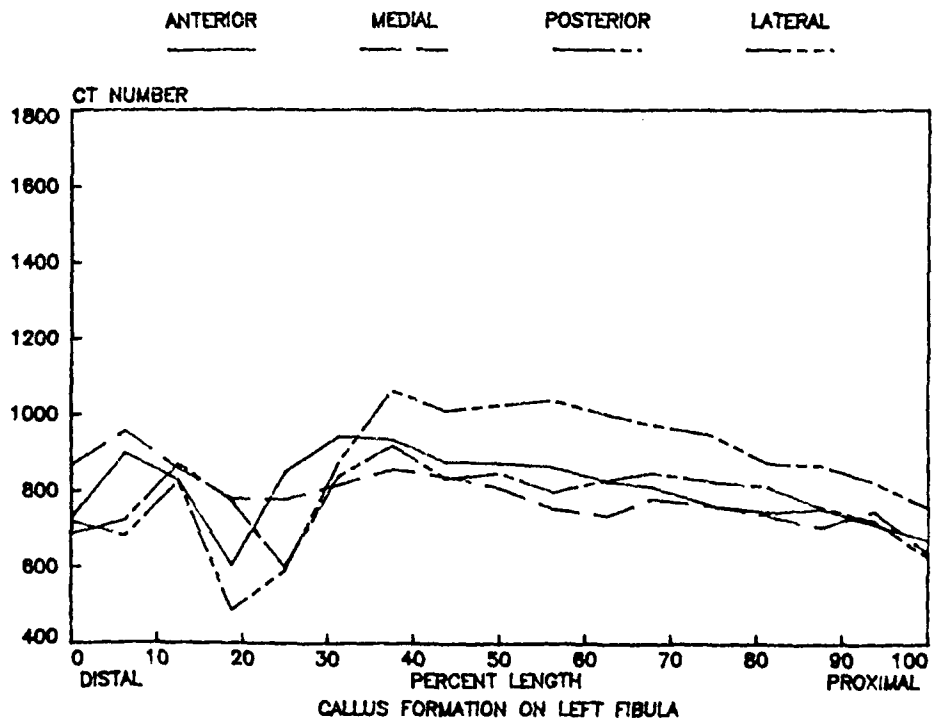
# LEFT BABOON TIBIA CT NUMBER



# RIGHT BABOON FIBULA CT NUMBER



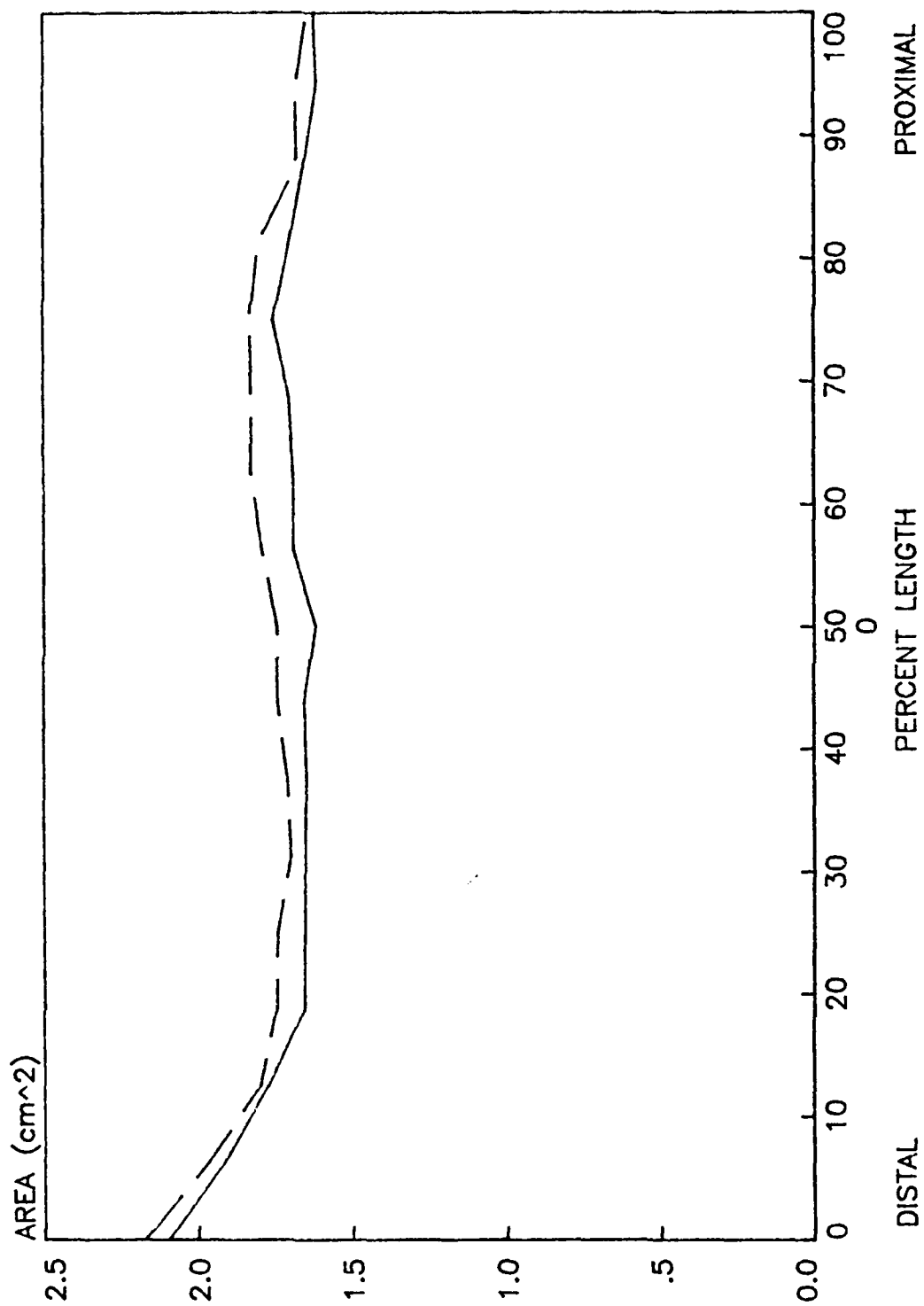
# LEFT BABOON FIBULA CT NUMBER





# BABOON HUMERUS AREA

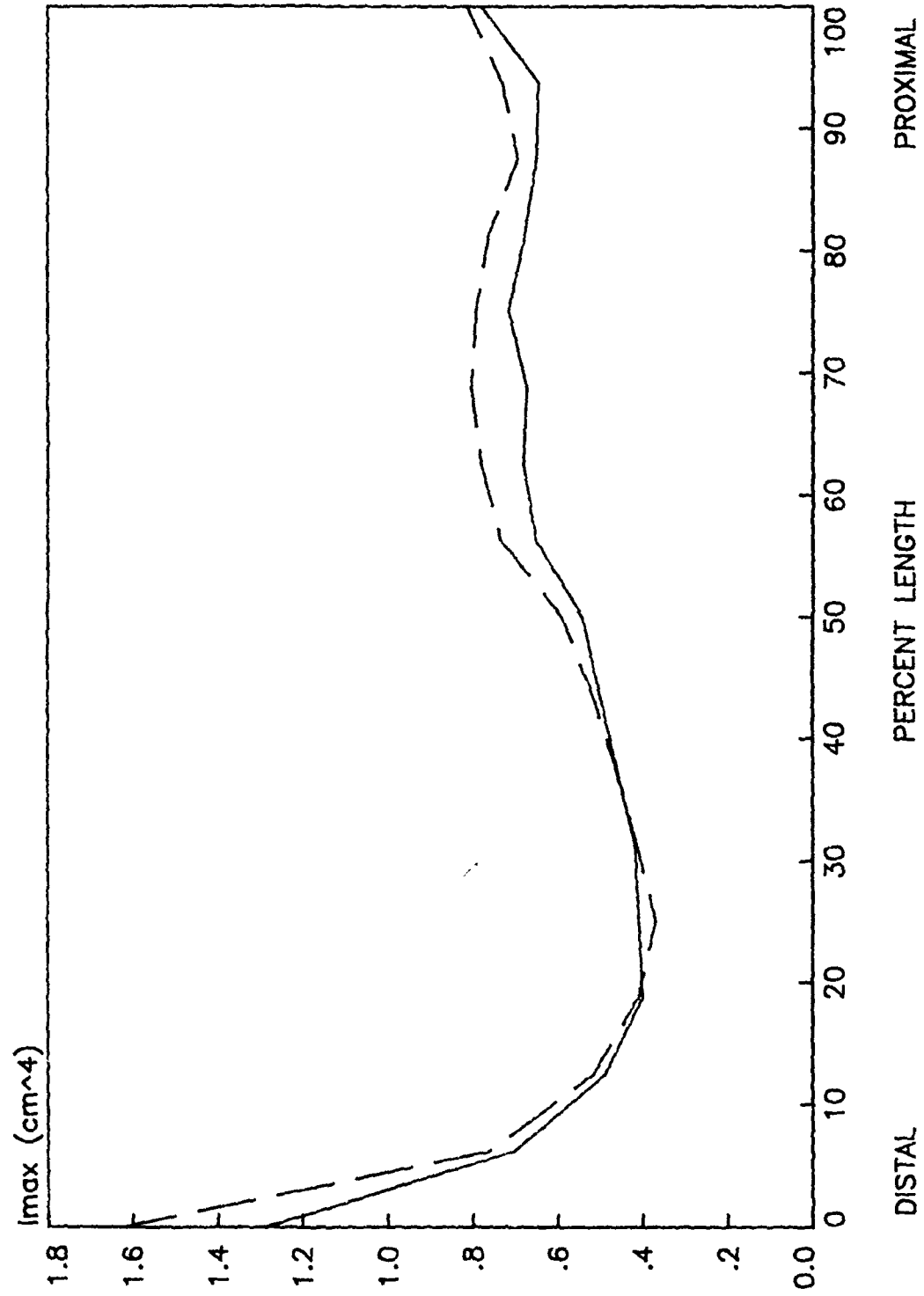
RIGHT      LEFT



# BABOON HUMERUS MAXIMUM MOMENT OF INERTIA

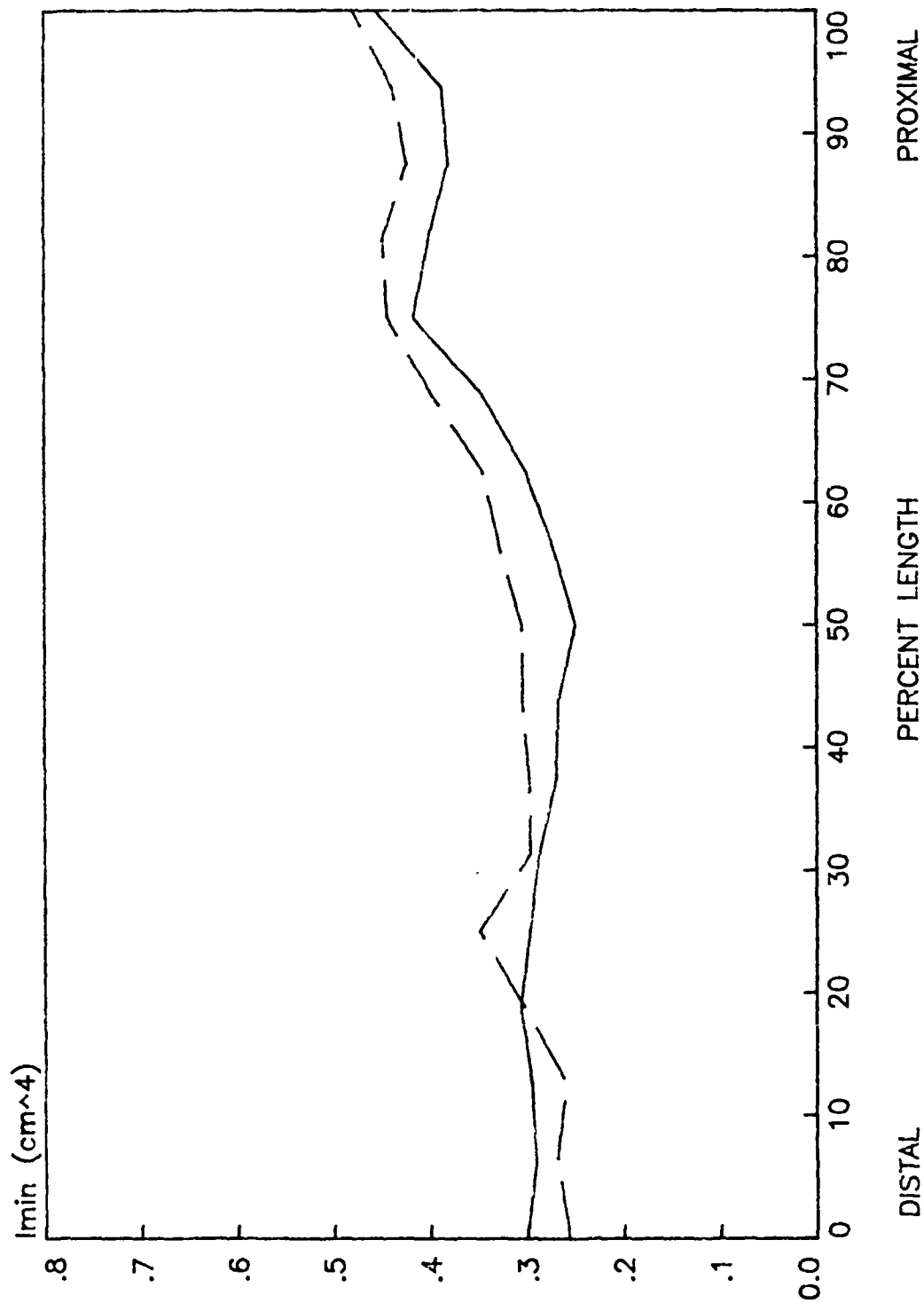
RIGHT

LEFT



# BABOON HUMERUS MINIMUM MOMENT OF INERTIA

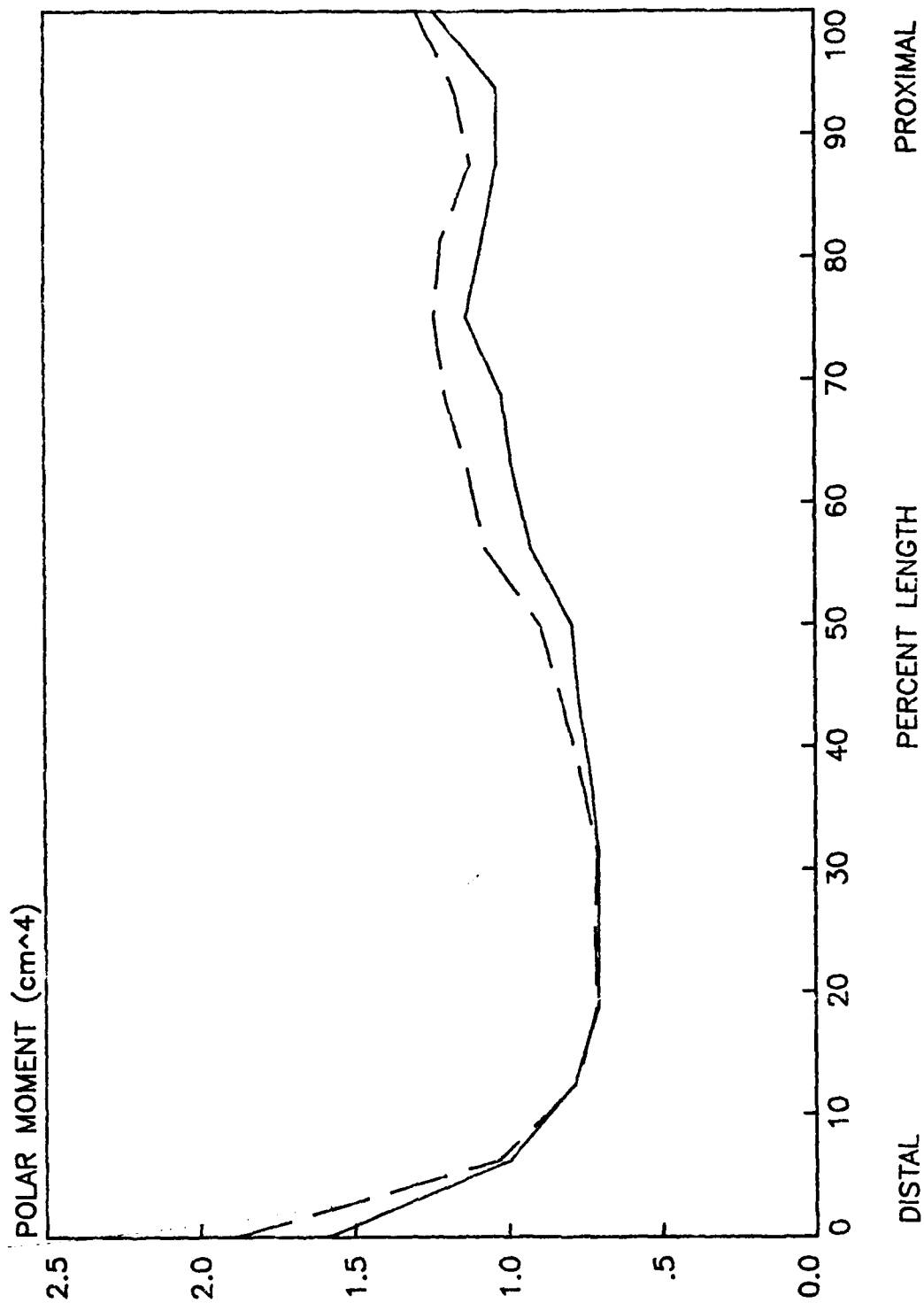
RIGHT      LEFT



# BABOON HUMERUS POLAR MOMENT OF INERTIA

RIGHT

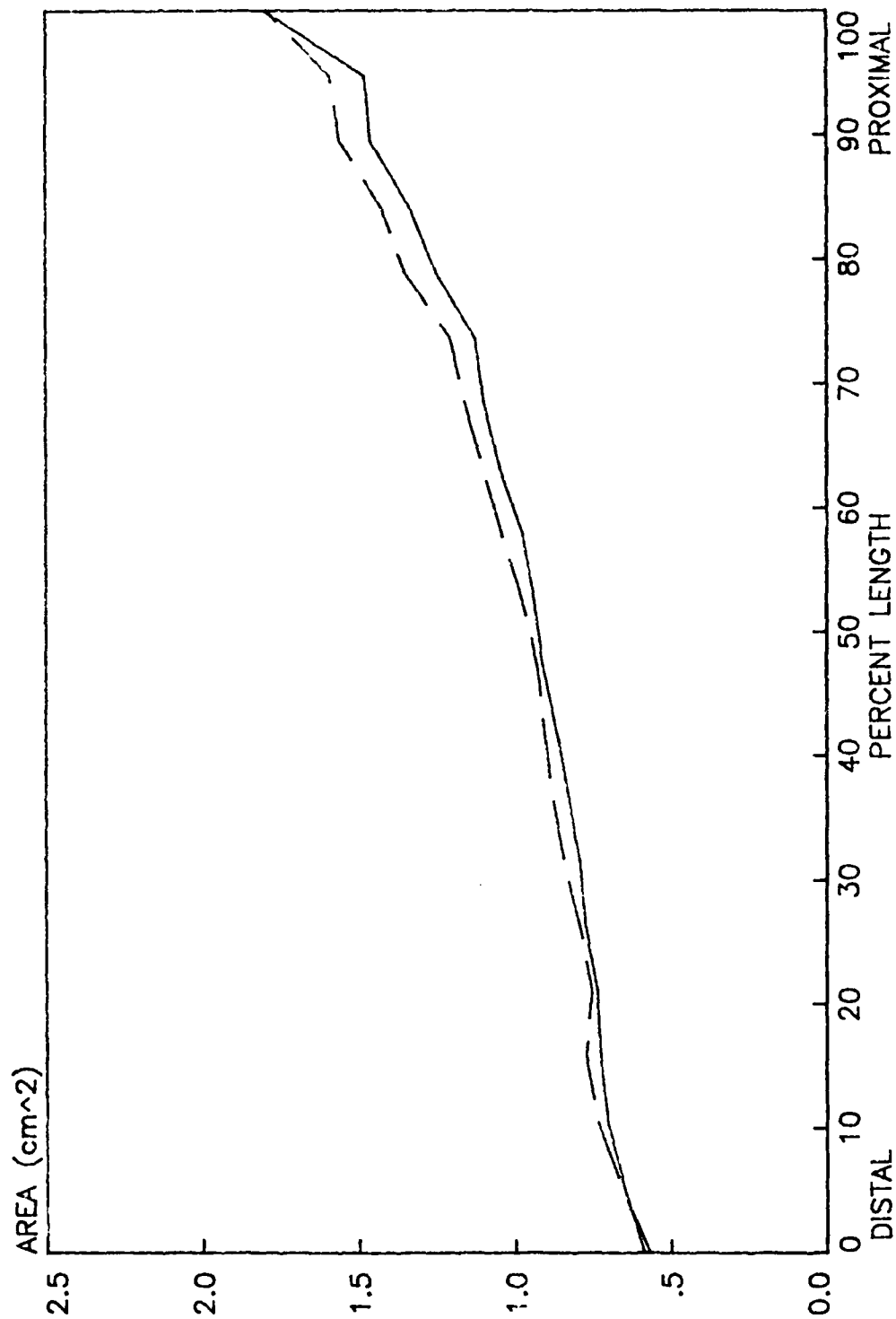
LEFT



# BABOON ULNA AREA

RIGHT

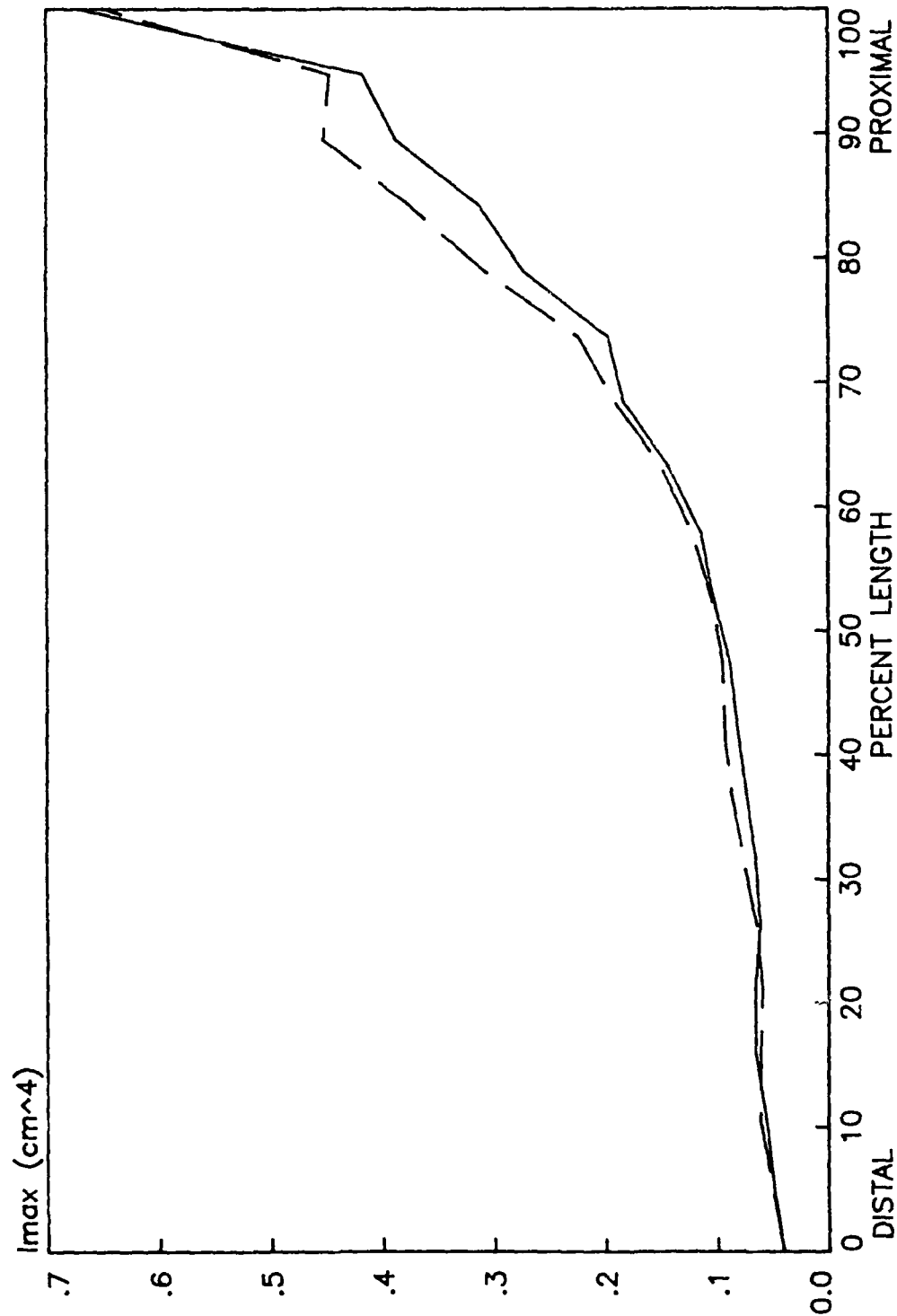
LEFT



# BABOON ULNA MAXIMUM MOMENT OF INERTIA

RIGHT      LEFT

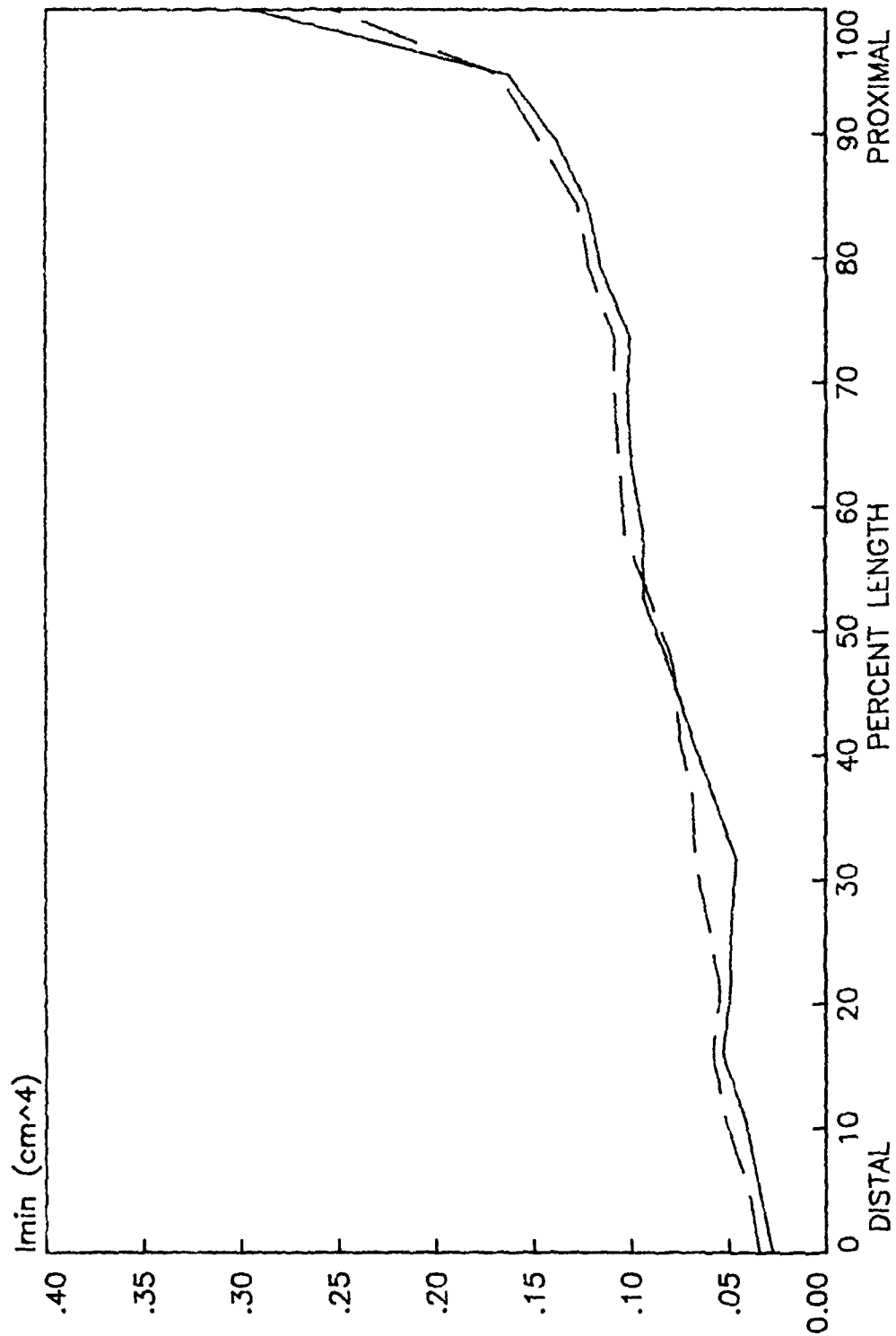
—      - - -



BABOON ULNA  
MINIMUM MOMENT OF INERTIA

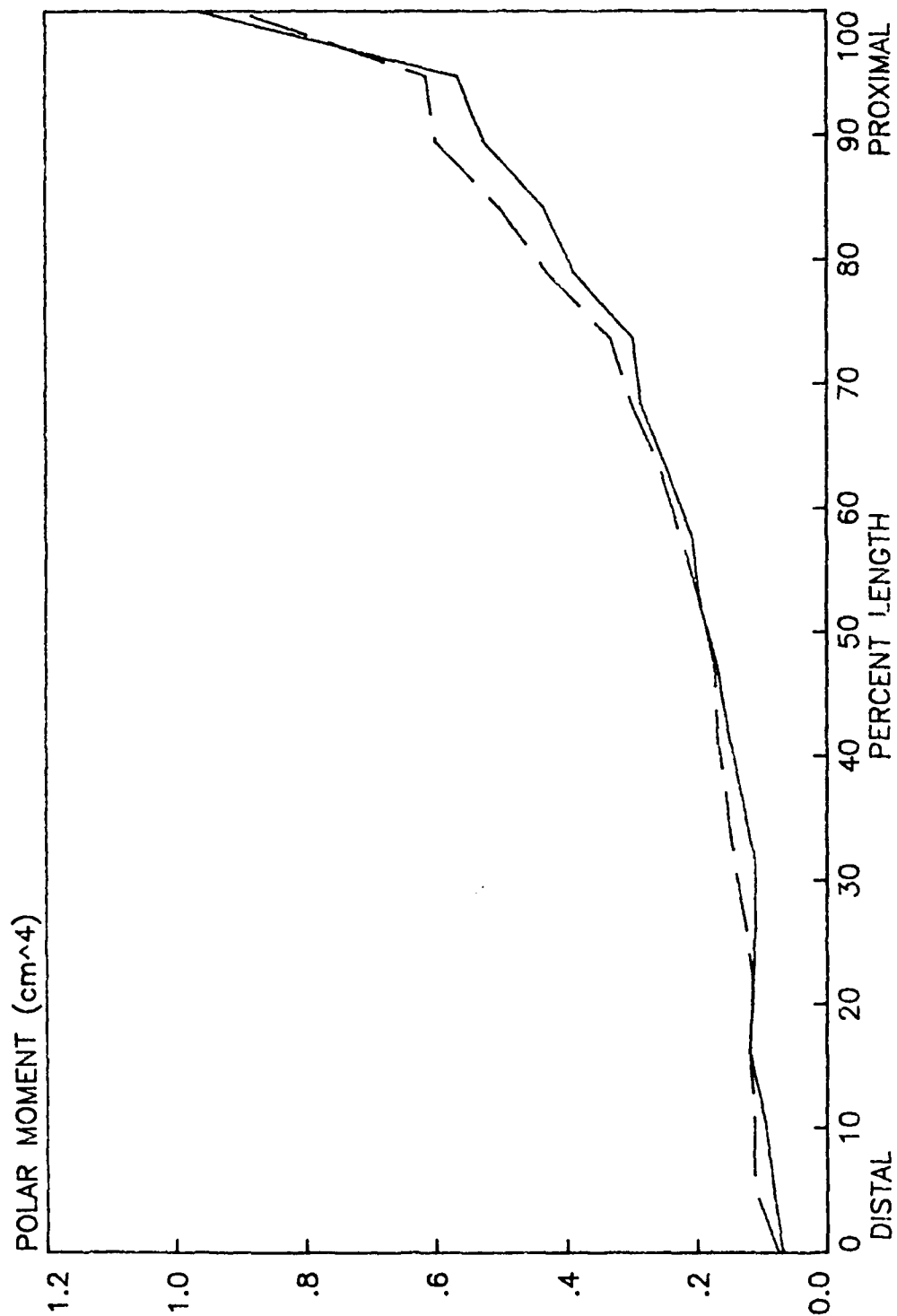
RIGHT      LEFT

\_\_\_\_\_



BABOON ULNA  
POLAR MOMENT OF INERTIA

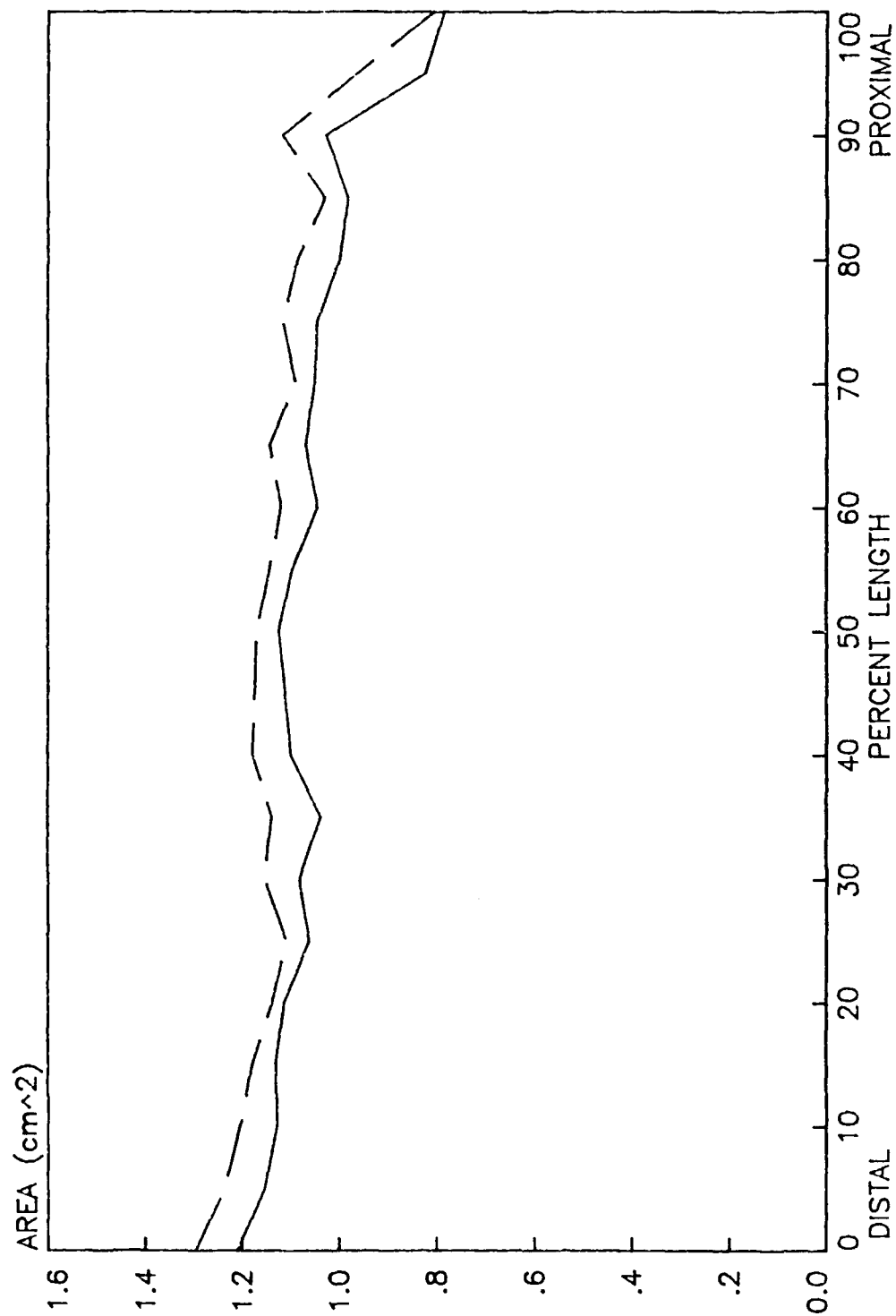
RIGHT      LEFT  
——      - - -





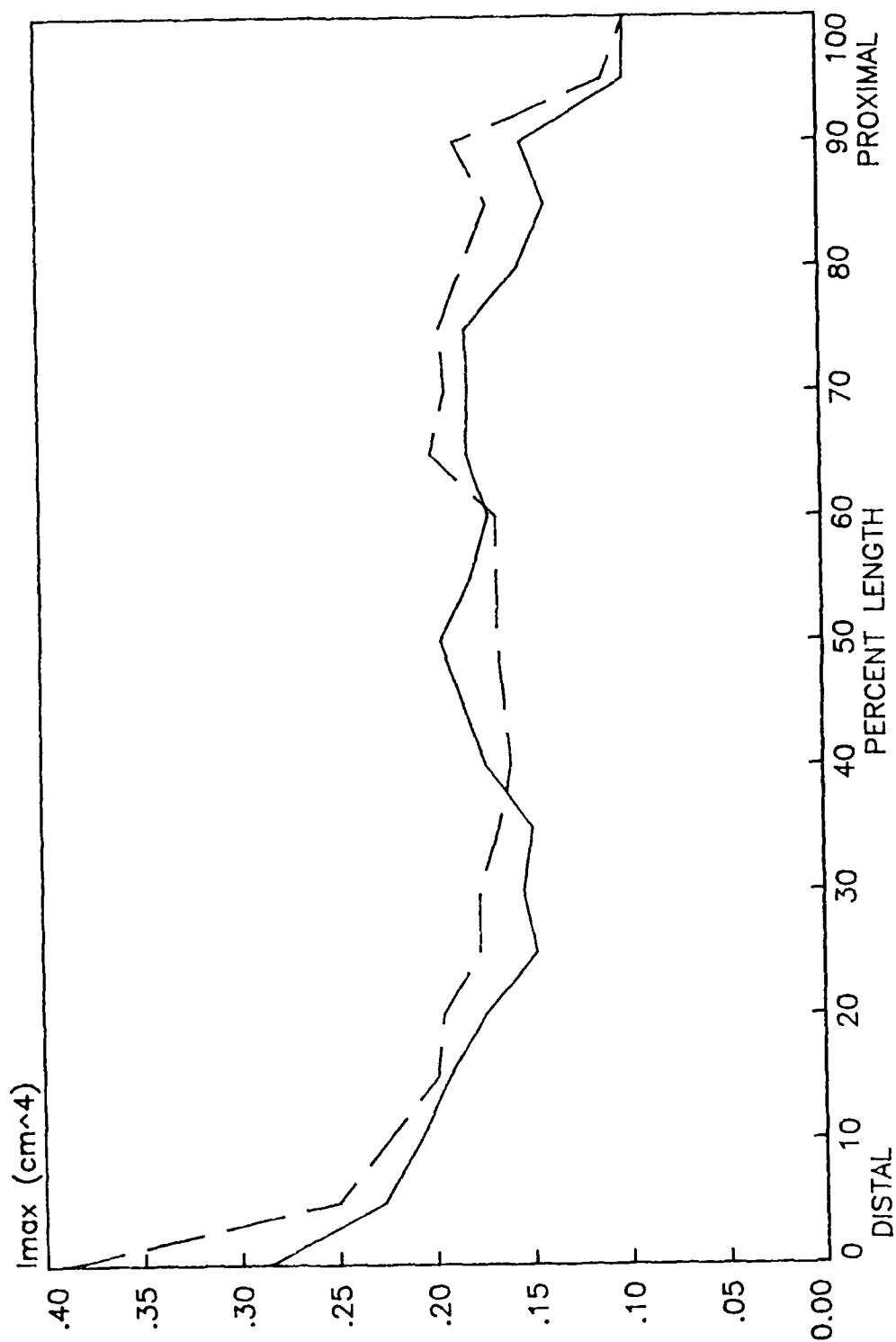
# BABOON RADIUS AREA

RIGHT      LEFT



# BABOON RADIUS MAXIMUM MOMENT OF INERTIA

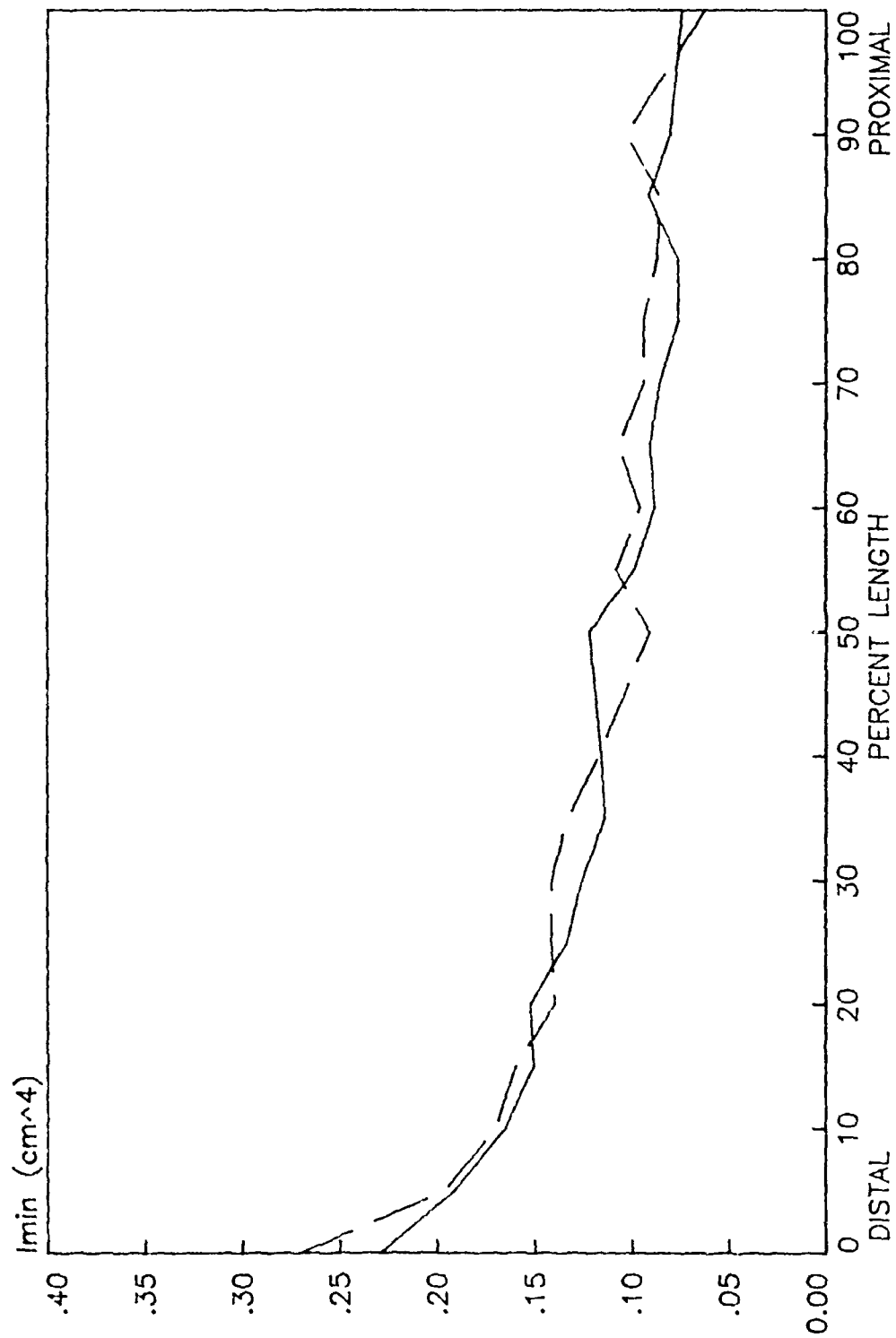
RIGHT      LEFT



# BABOON RADIUS MINIMUM MOMENT OF INERTIA

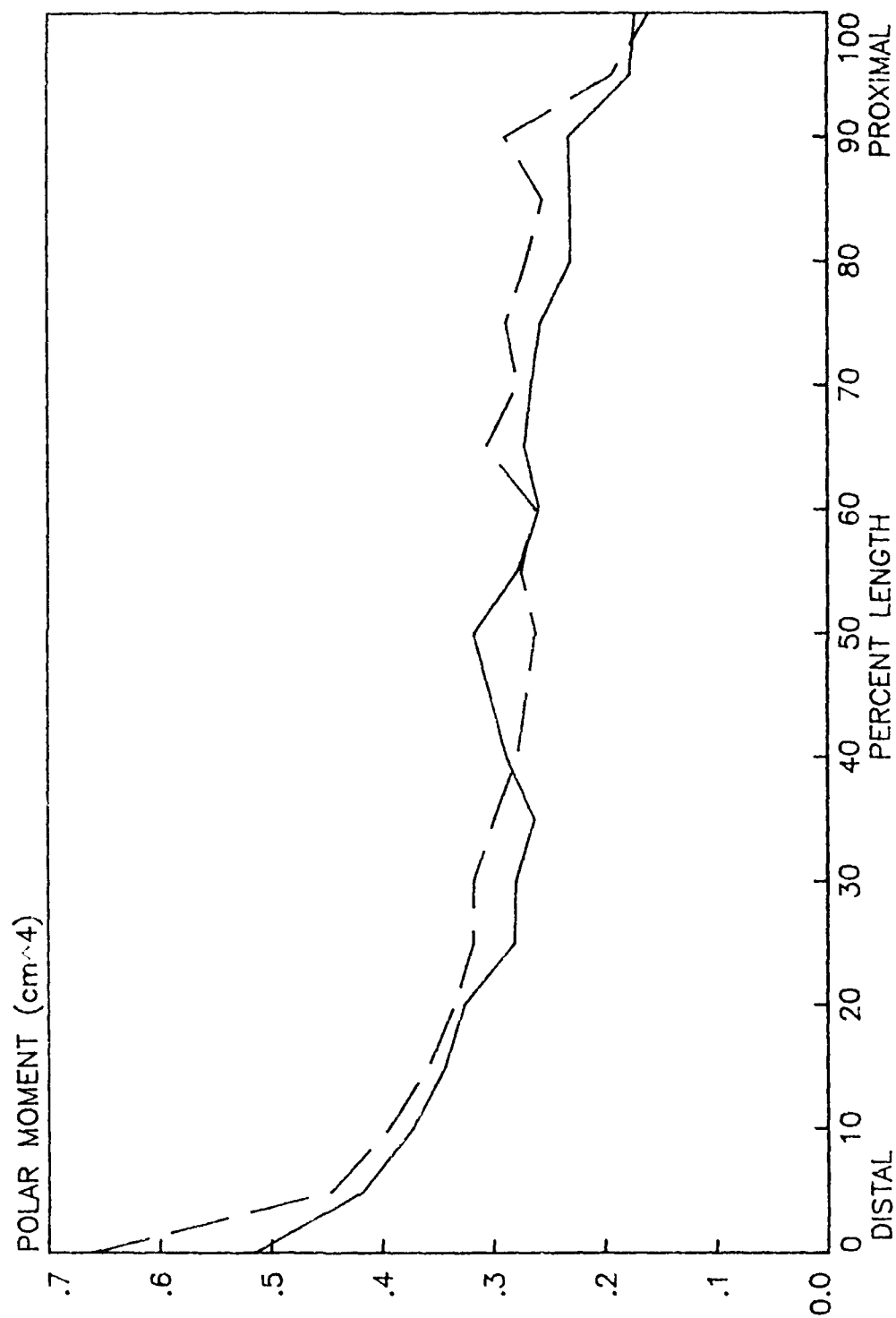
RIGHT      LEFT

— — —



# BABOON RADIUS POLAR MOMENT OF INERTIA

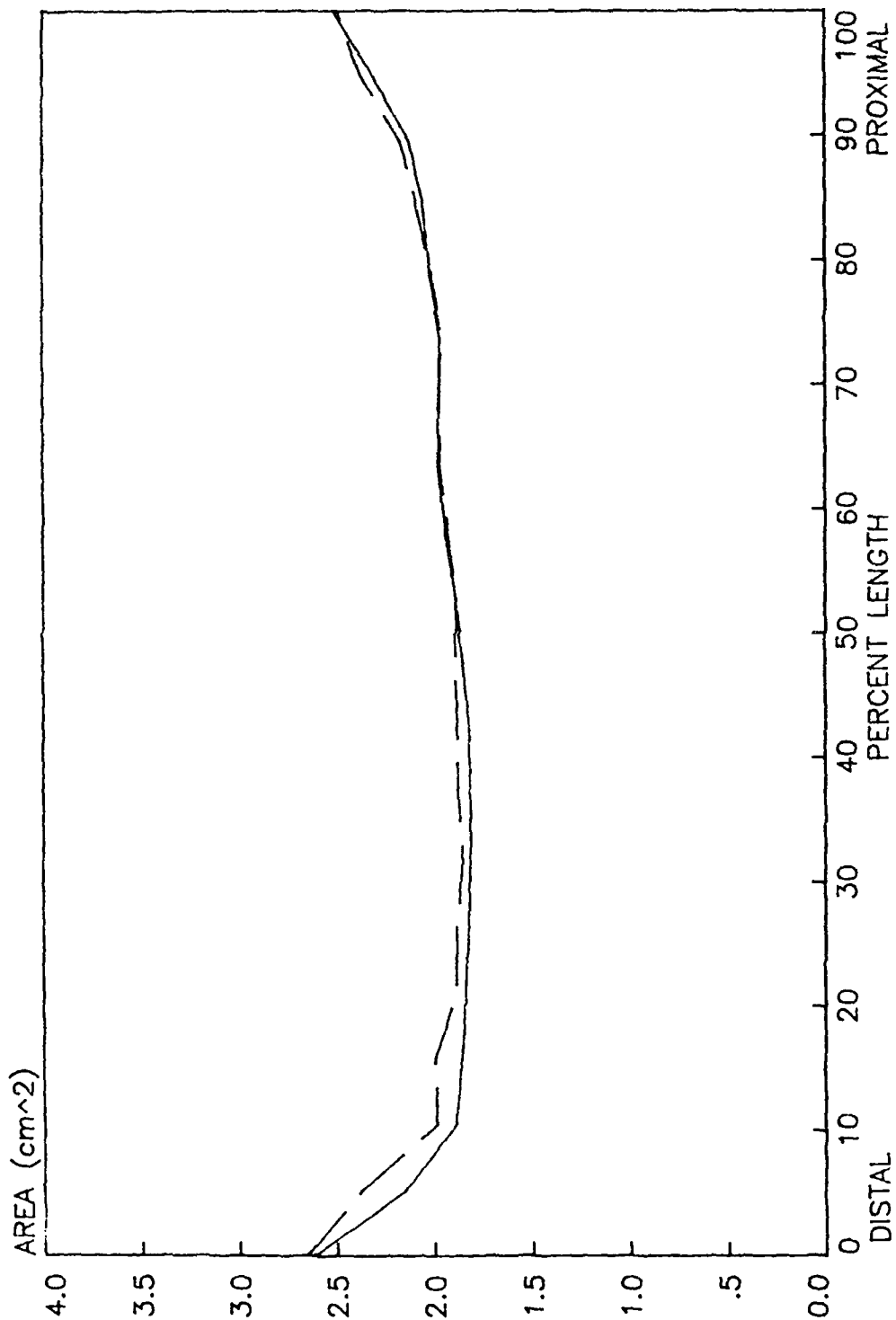
RIGHT      LEFT  
—      —



# BABOON FEMUR AREA

RIGHT

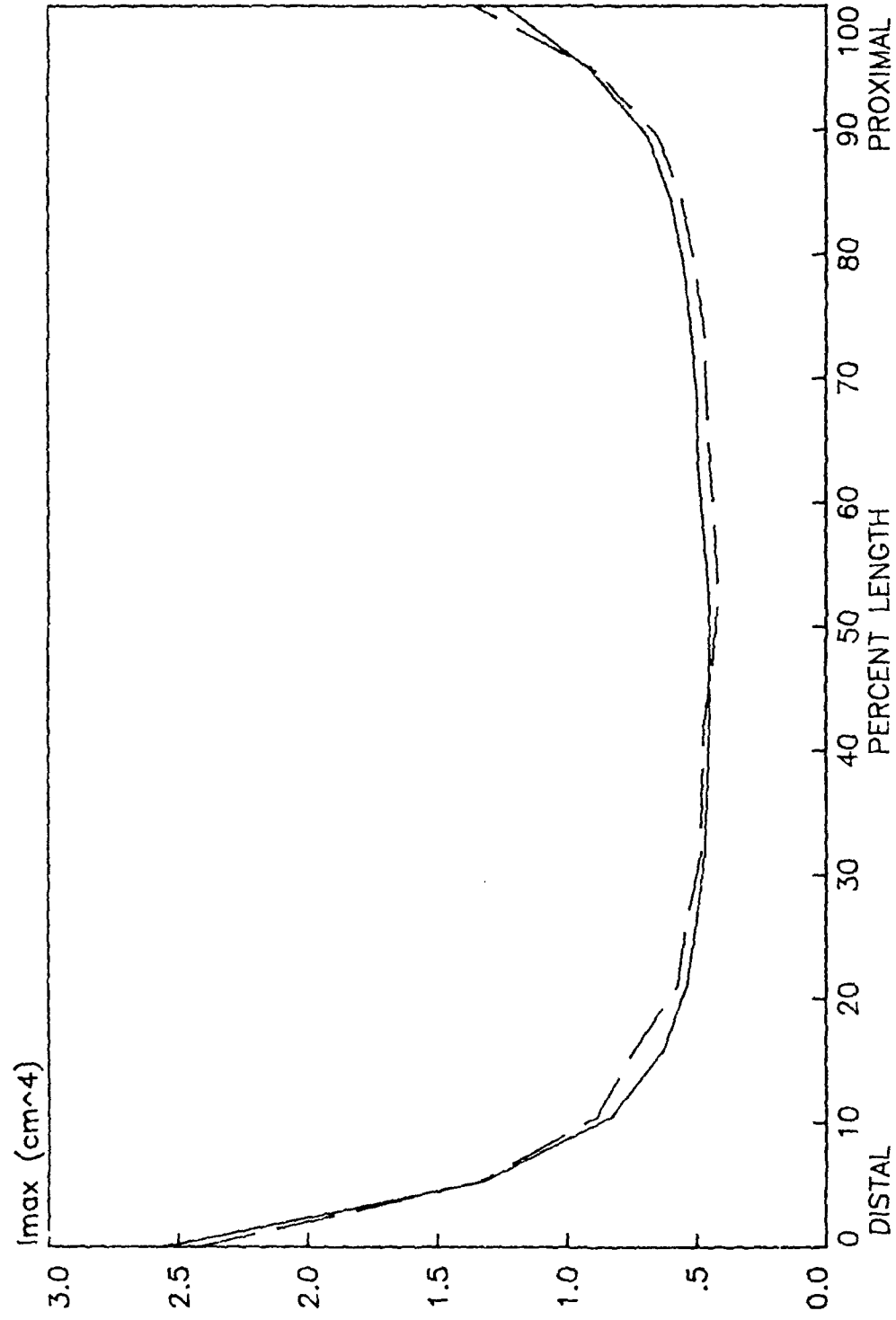
LEFT



# BABOON FEMUR MAXIMUM MOMENT OF INERTIA

RIGHT

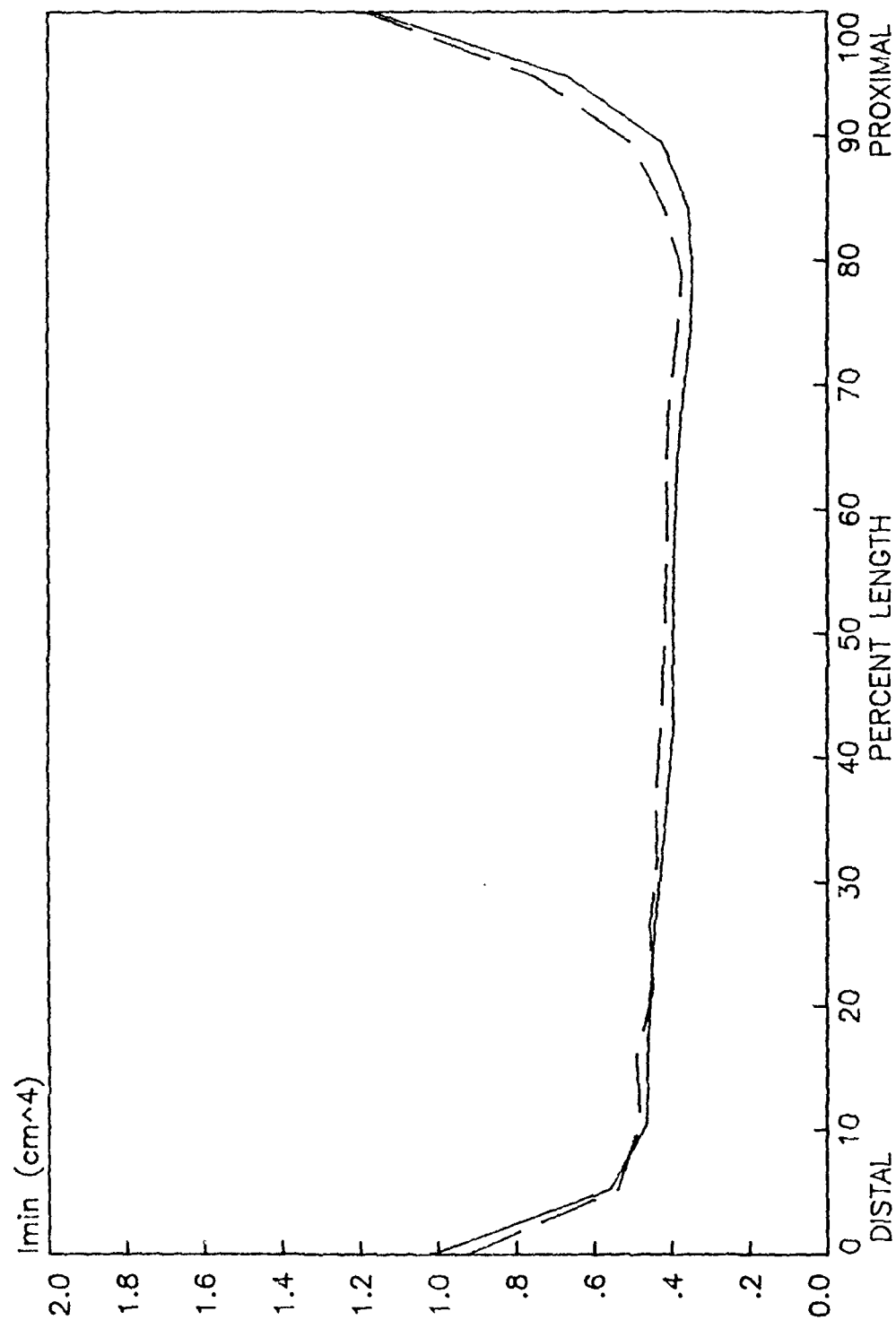
LEFT



# BABOON FEMUR MINIMUM MOMENT OF INERTIA

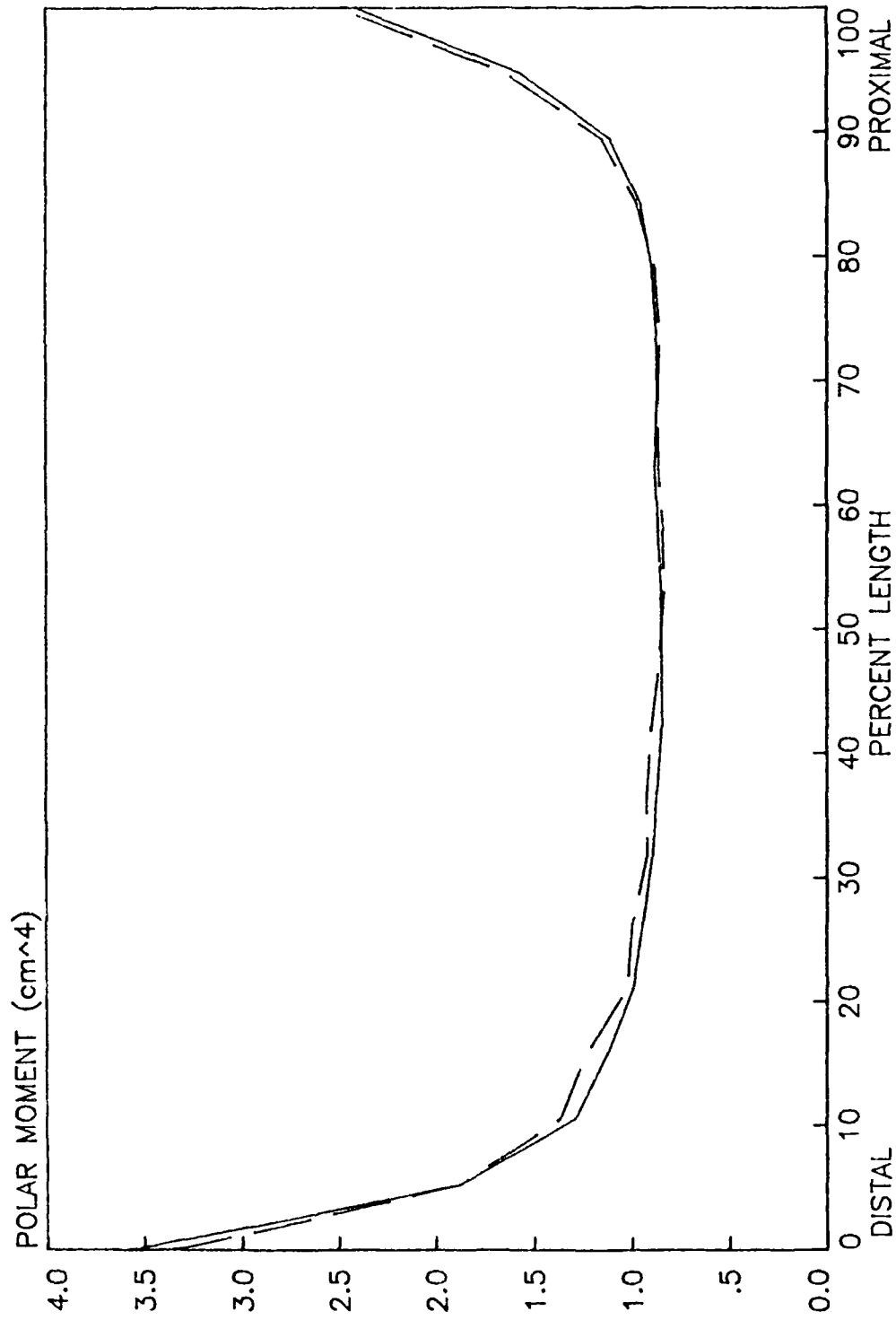
RIGHT

LEFT



# BABOON FEMUR POLAR MOMENT OF INERTIA

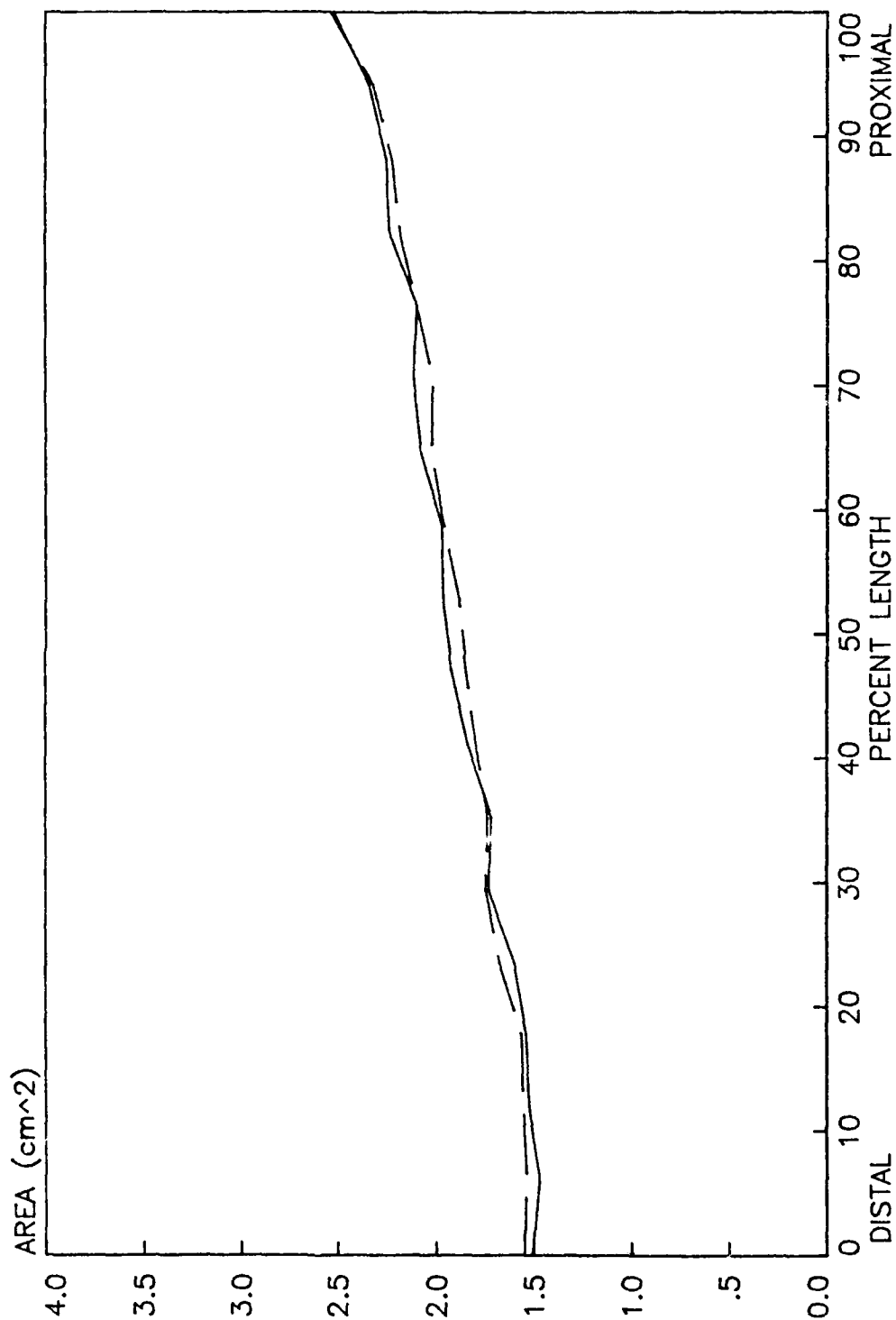
RIGHT      LEFT





# BABOON TIBIA AREA

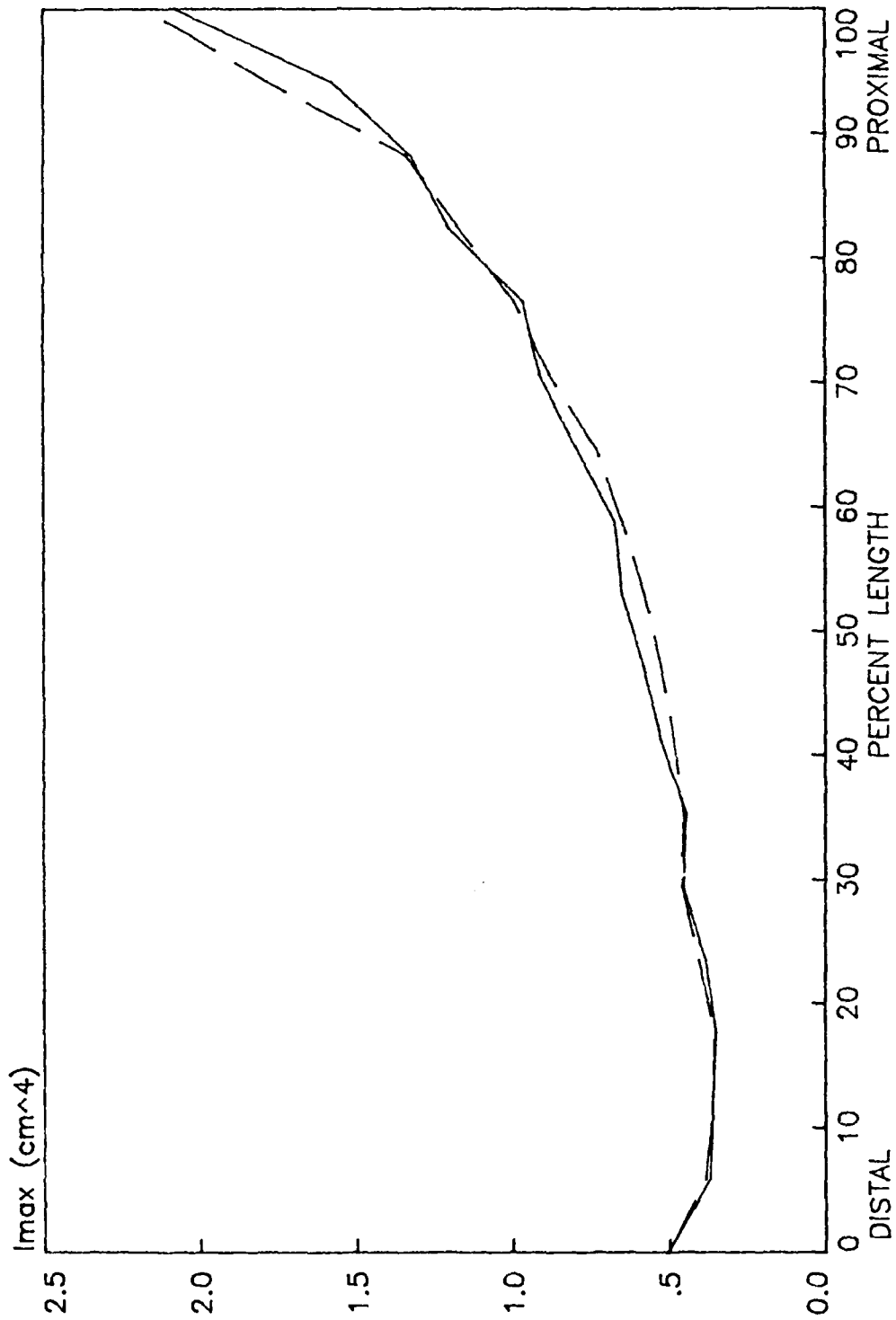
RIGHT      LEFT



BABOON TIBIA  
MAXIMUM MOMENT OF INERTIA

RIGHT

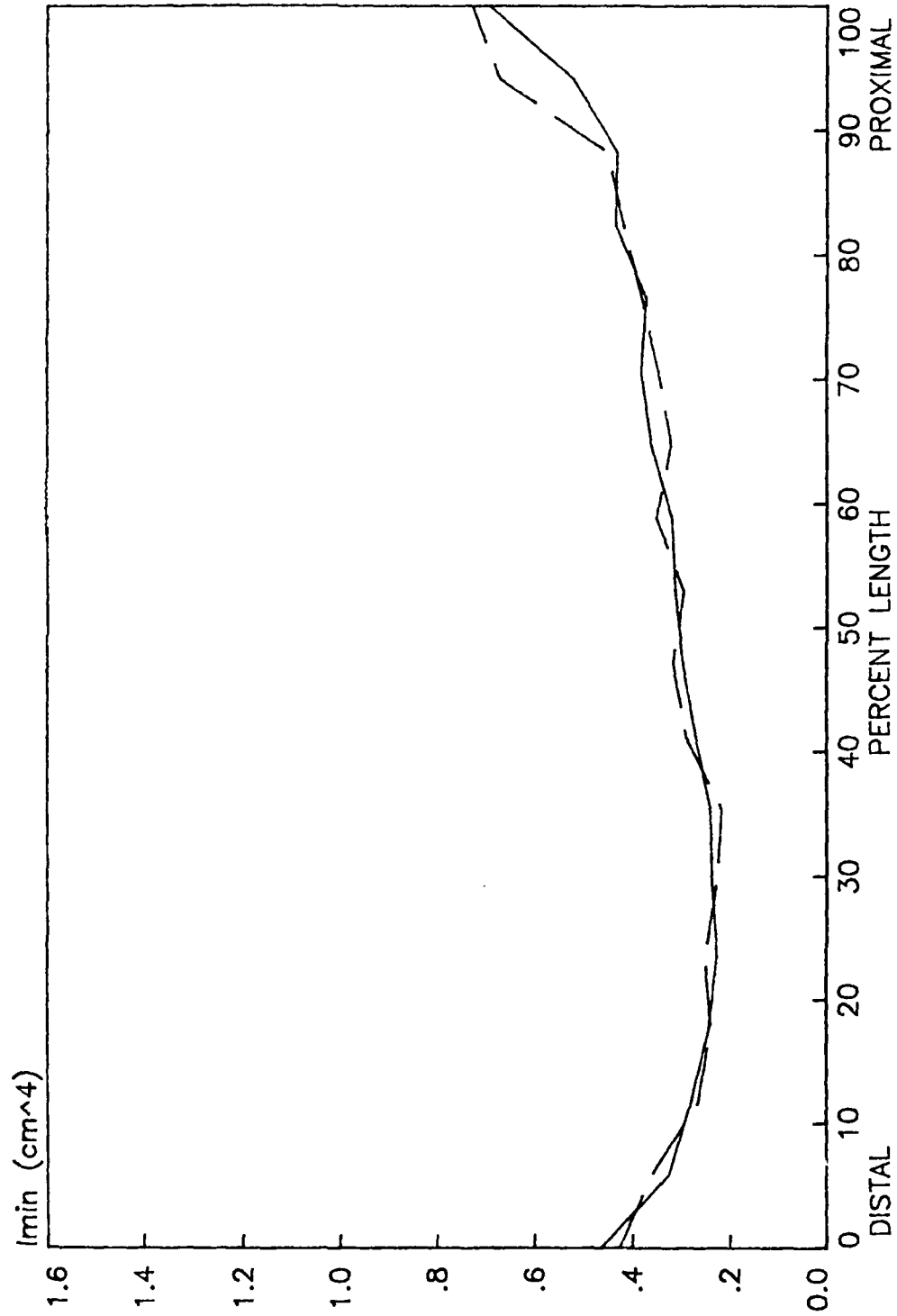
LEFT



# BABOON TIBIA MINIMUM MOMENT OF INERTIA

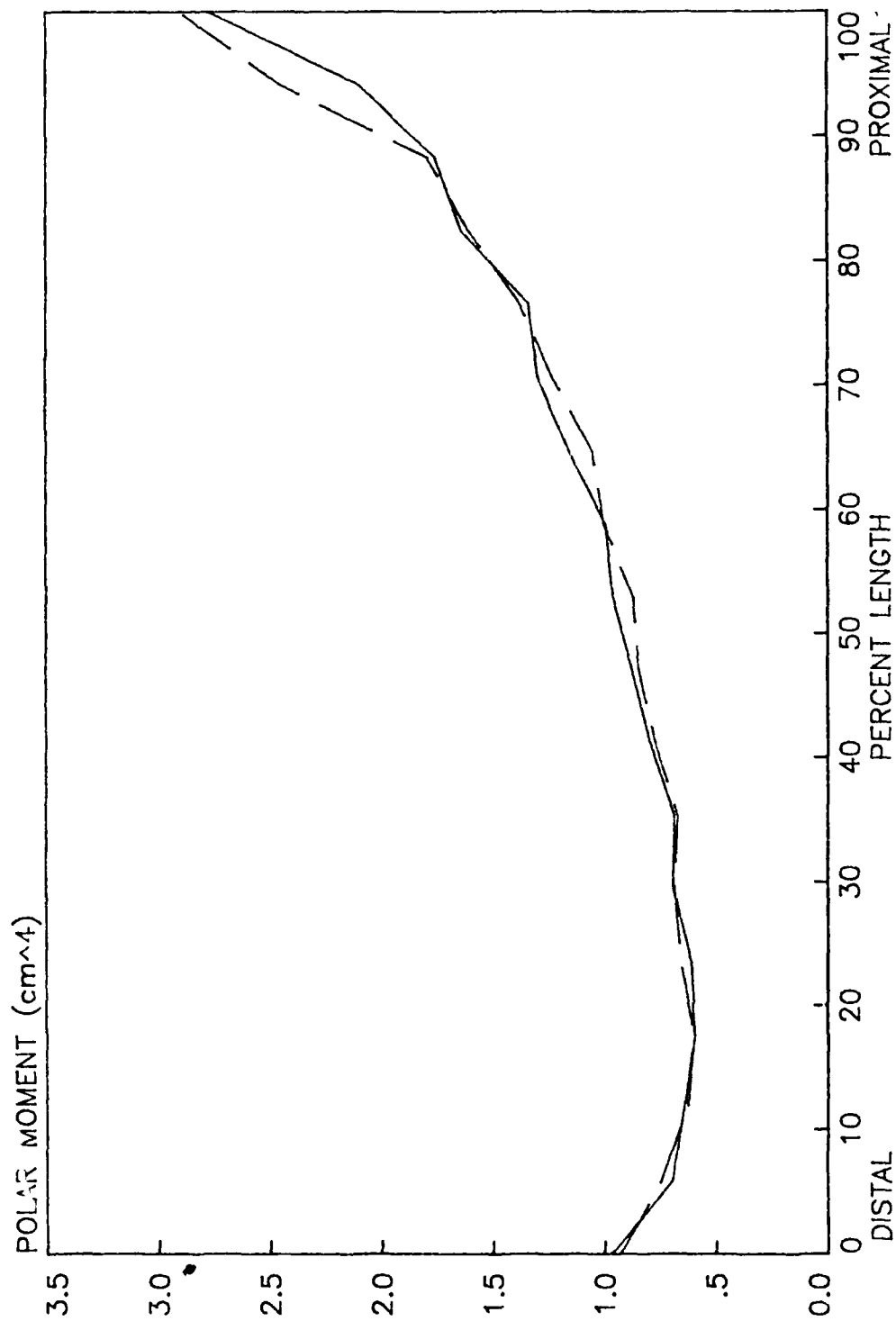
RIGHT

LEFT



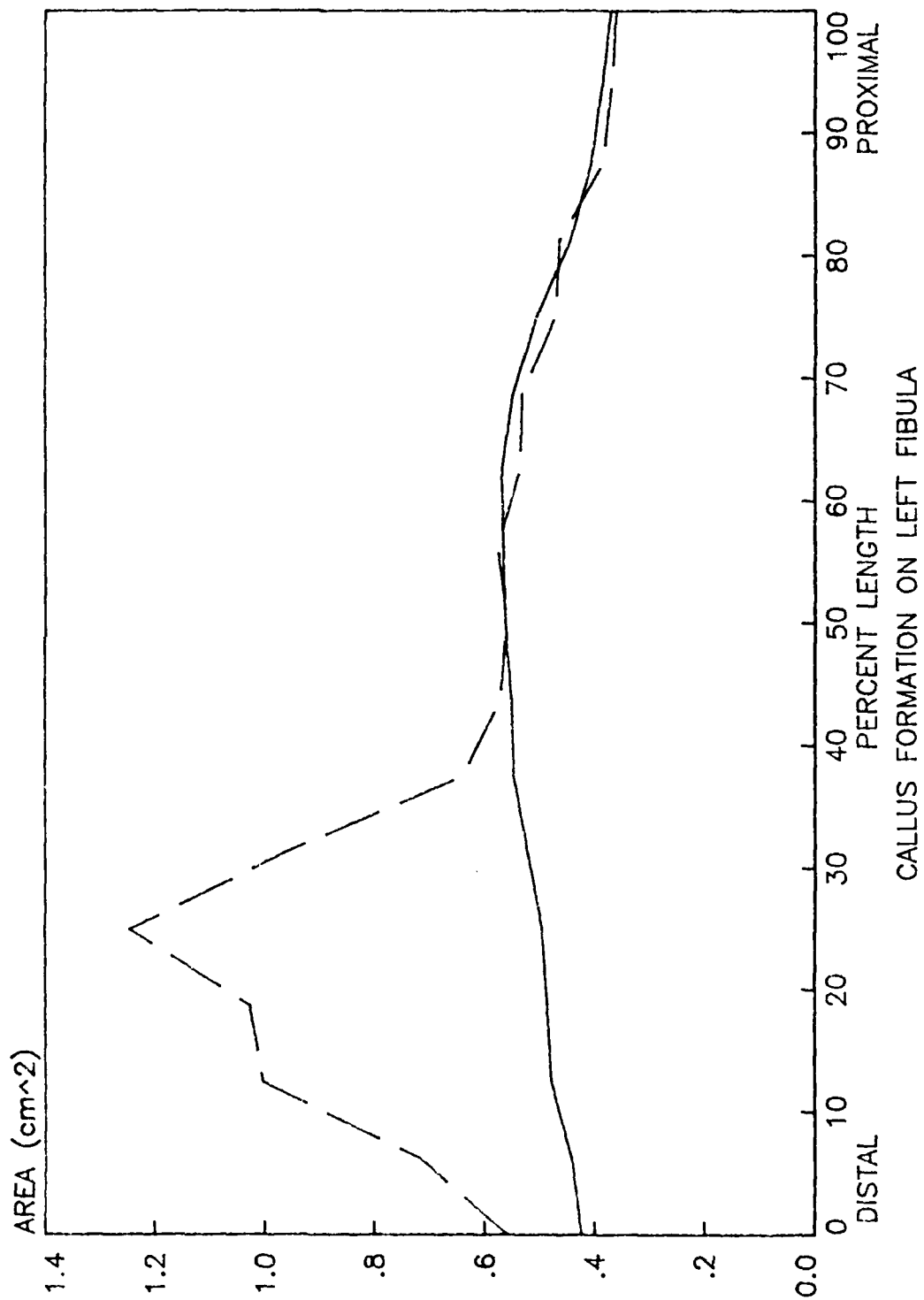
# BABOON TIBIA POLAR MOMENT OF INERTIA

RIGHT      LEFT



# BABOON FIBULA AREA

RIGHT      LEFT



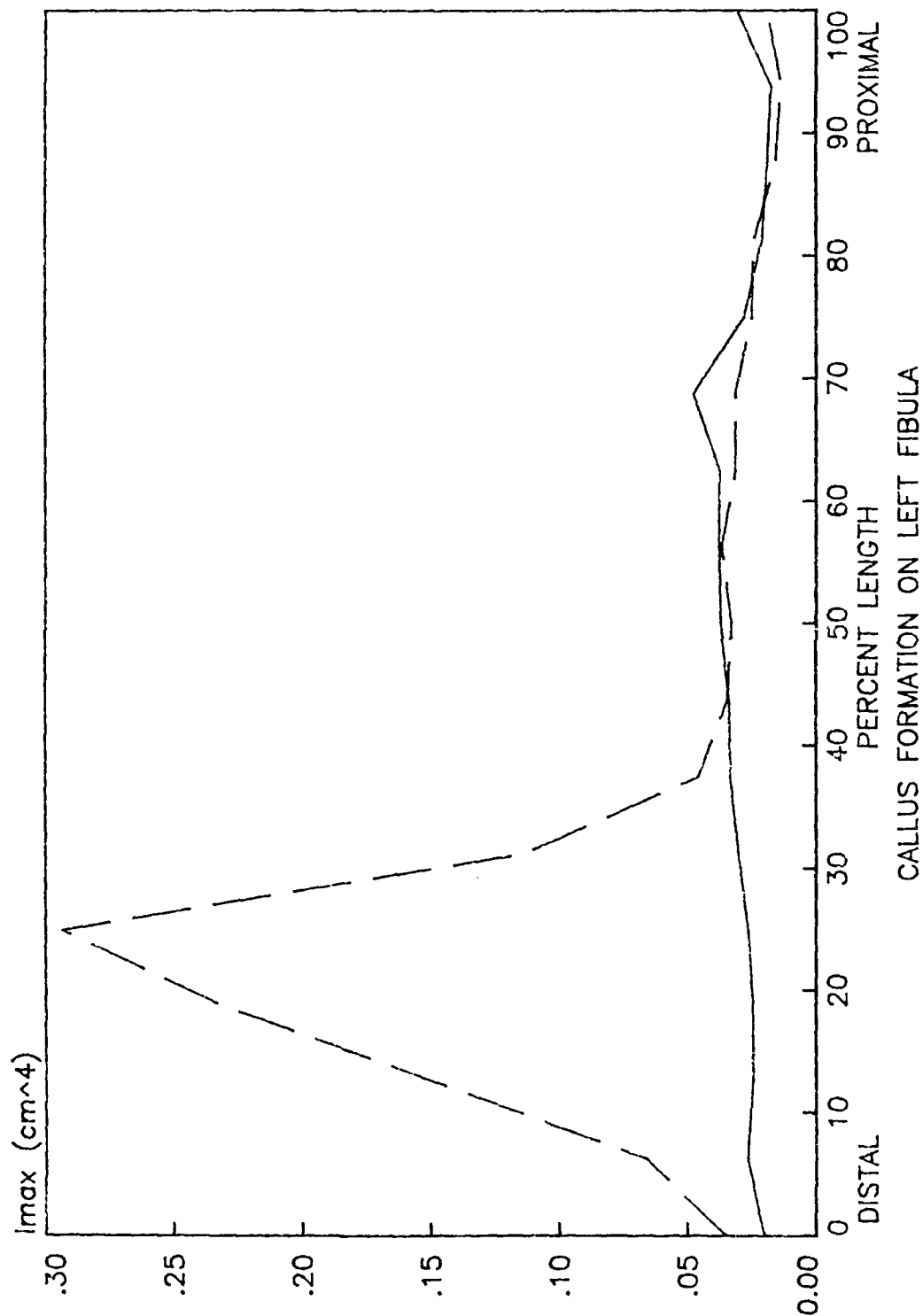
# BABOON FIBULA MAXIMUM MOMENT OF INERTIA

RIGHT

LEFT

\_\_\_\_\_

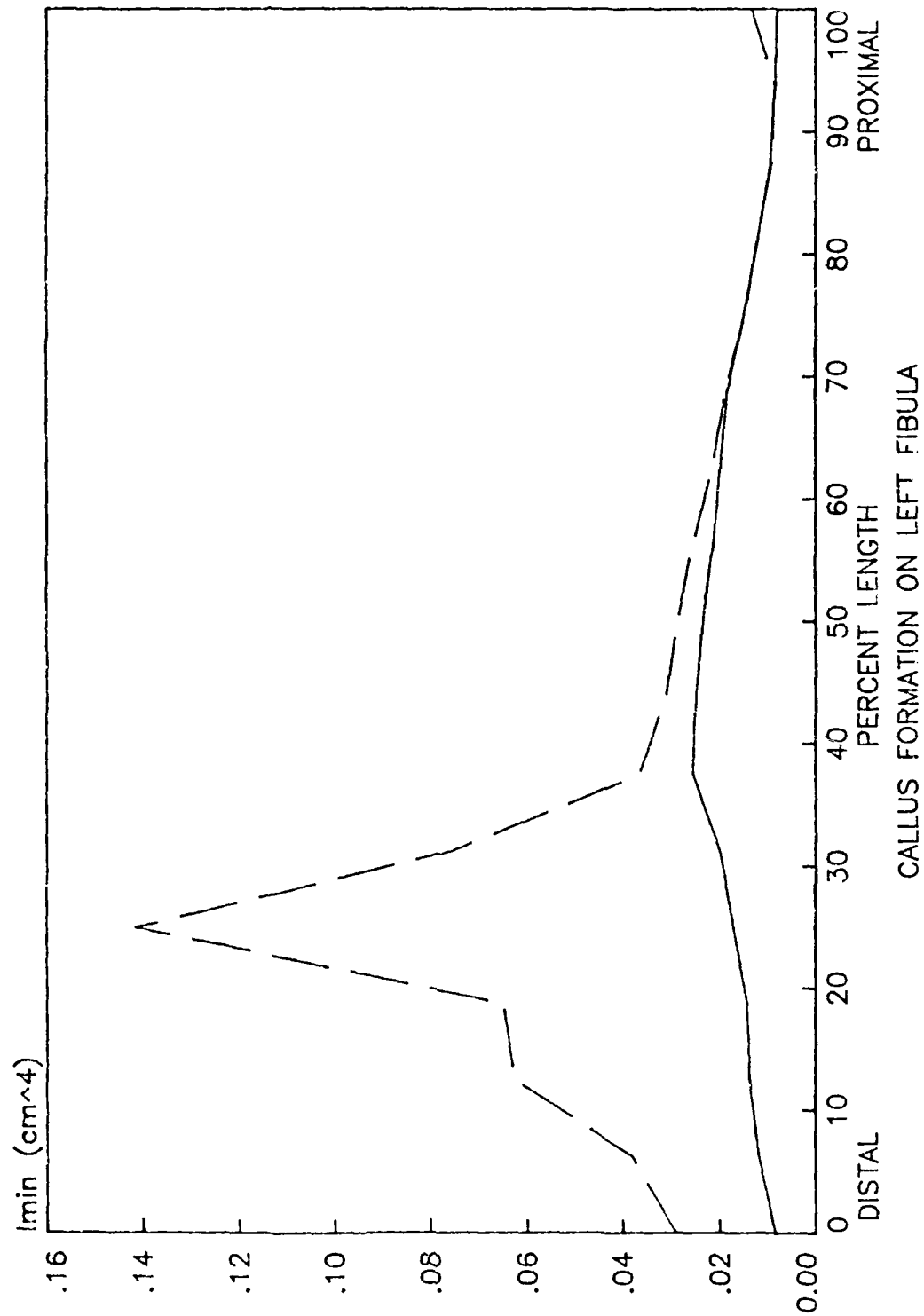
\_\_\_\_\_



# BABOON FIBULA MINIMUM MOMENT OF INERTIA

RIGHT

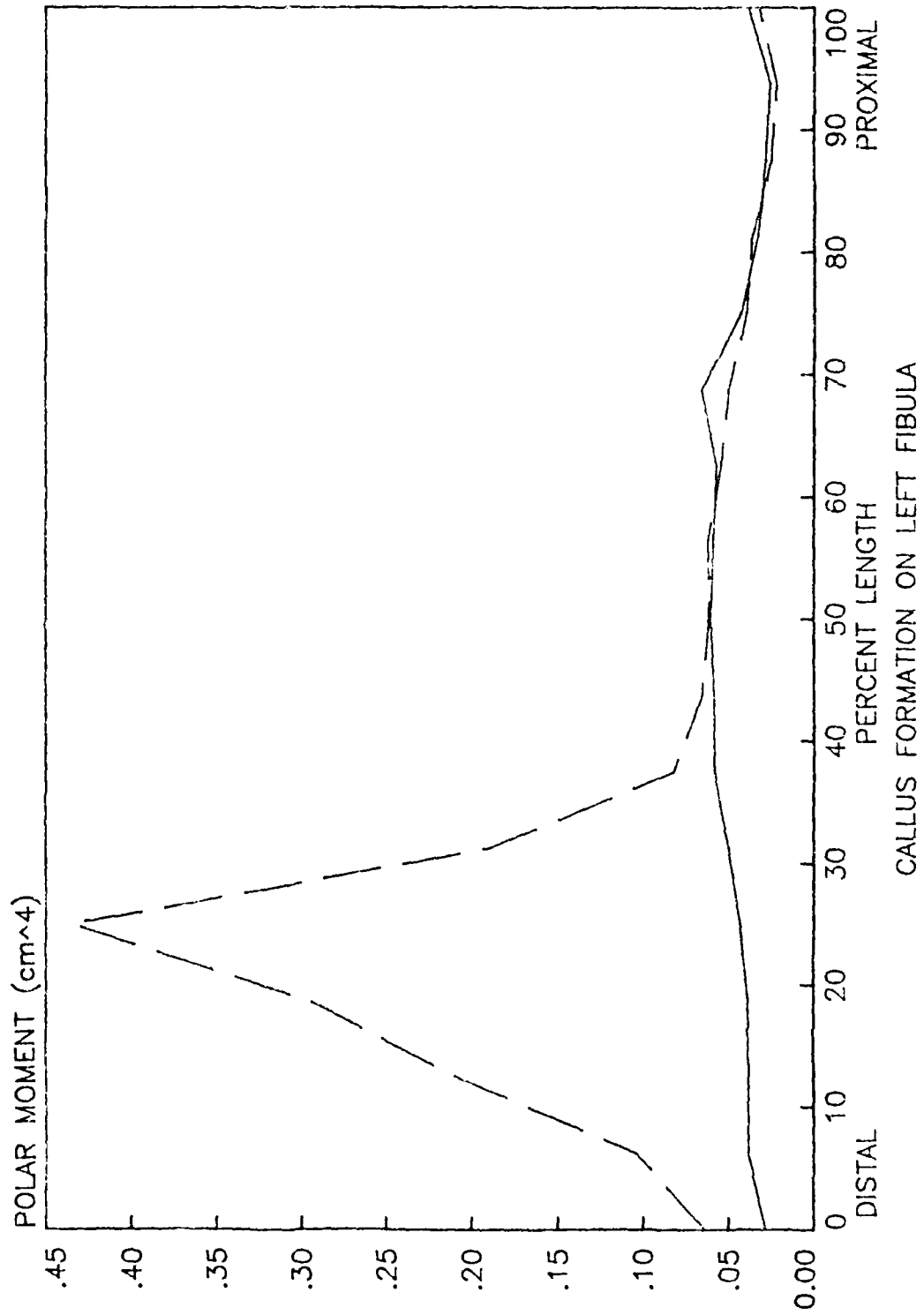
LEFT



# BABOON FIBULA POLAR MOMENT OF INERTIA

RIGHT

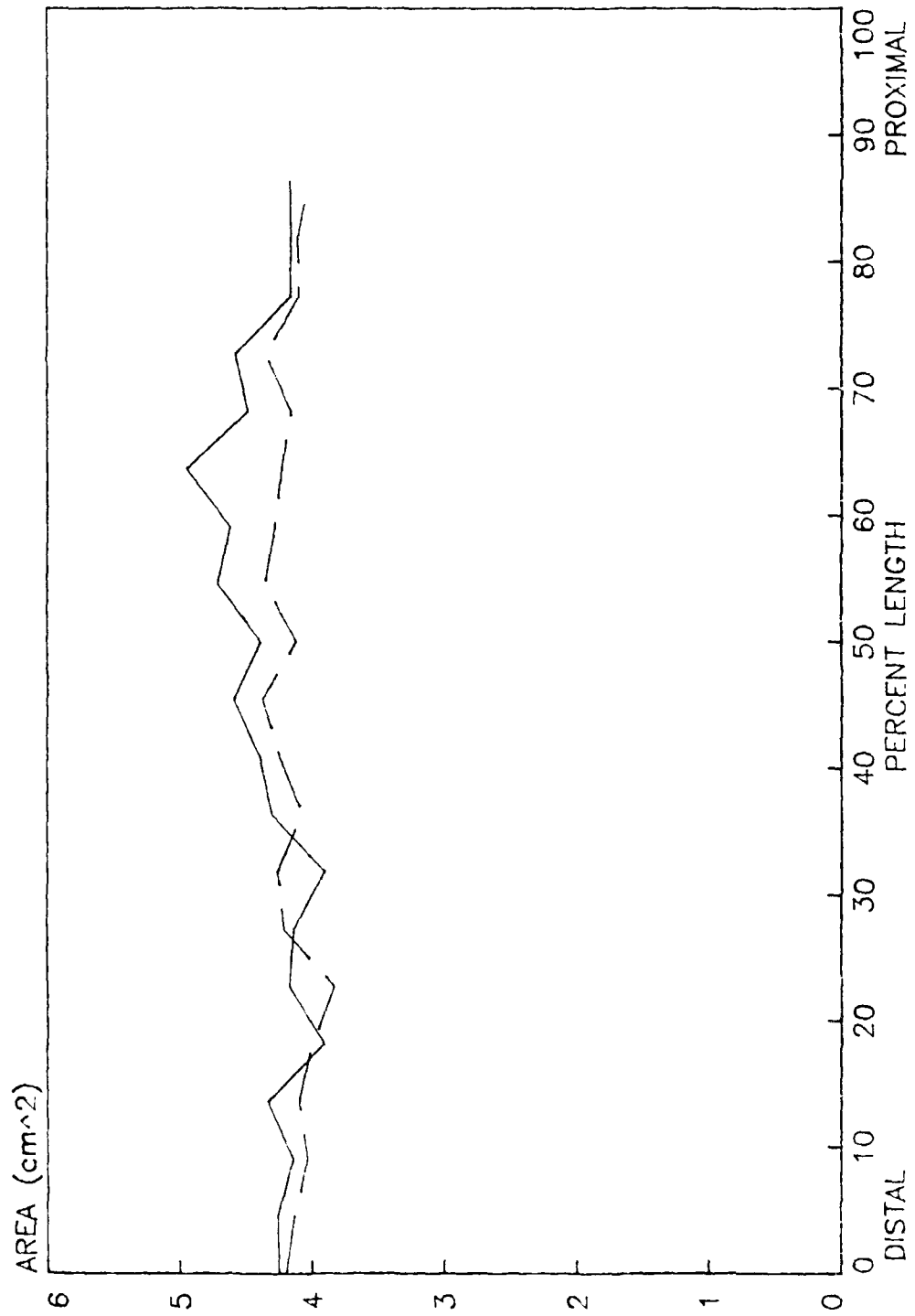
LEFT





# HUMAN HUMERUS AREA

RIGHT      LEFT



AD-A096 983 CLEVELAND CLINIC FOUNDATION OHIO DEPT OF RADIOLOGY  
THE MECHANICS OF LONG BONE FRACTURES

F/G 45

31 JAN 81 MORAN, JAMES M.

F49620-79-C-0112

UNCLASSIFIED

PROJ. 2312 TASK A2 AFOSR TR-81-0294

NL

1 of 2  
20 pages

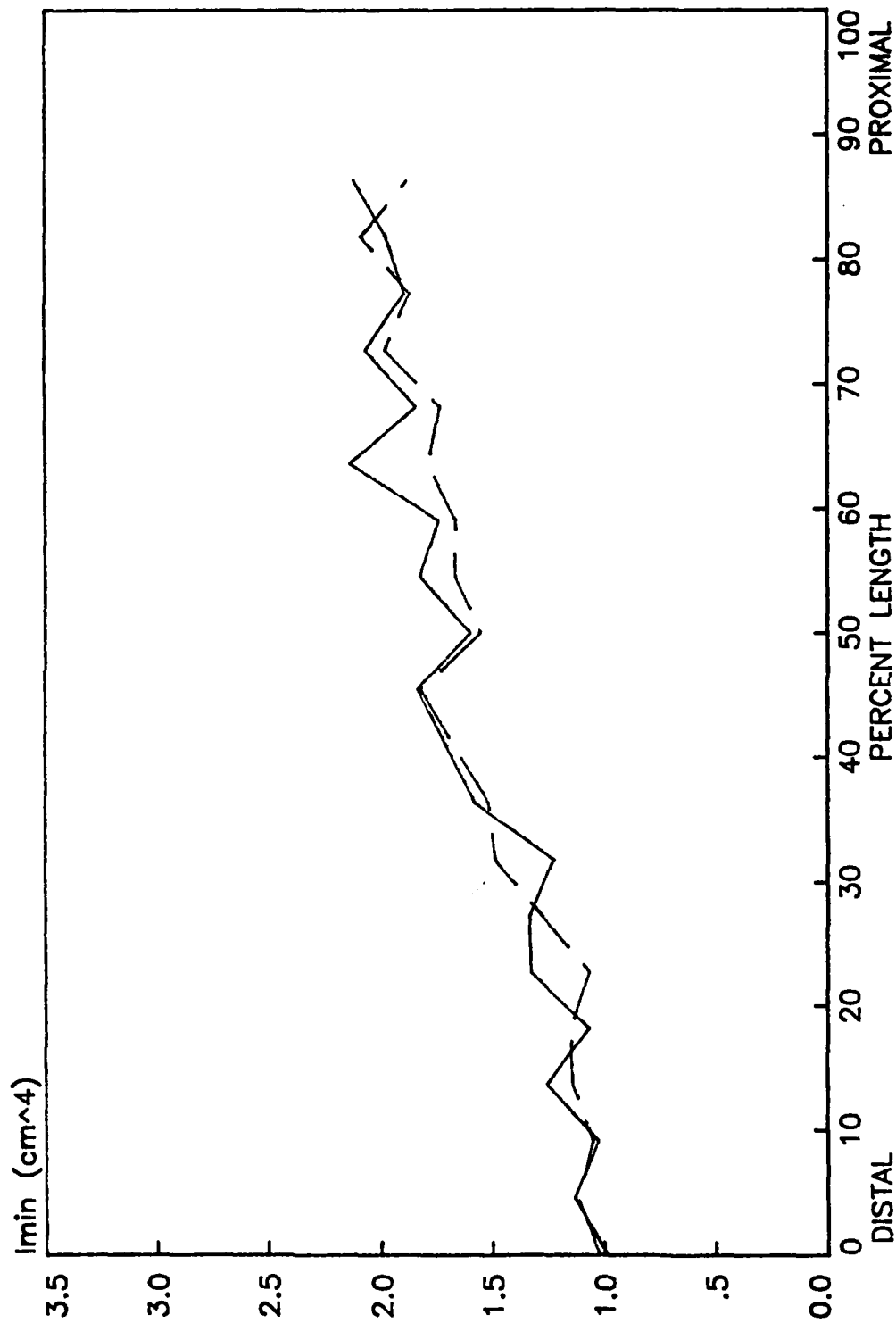


END  
DATE  
FILMED  
4-81  
DTIC

# HUMAN HUMERUS MINIMUM MOMENT OF INERTIA

RIGHT

LEFT



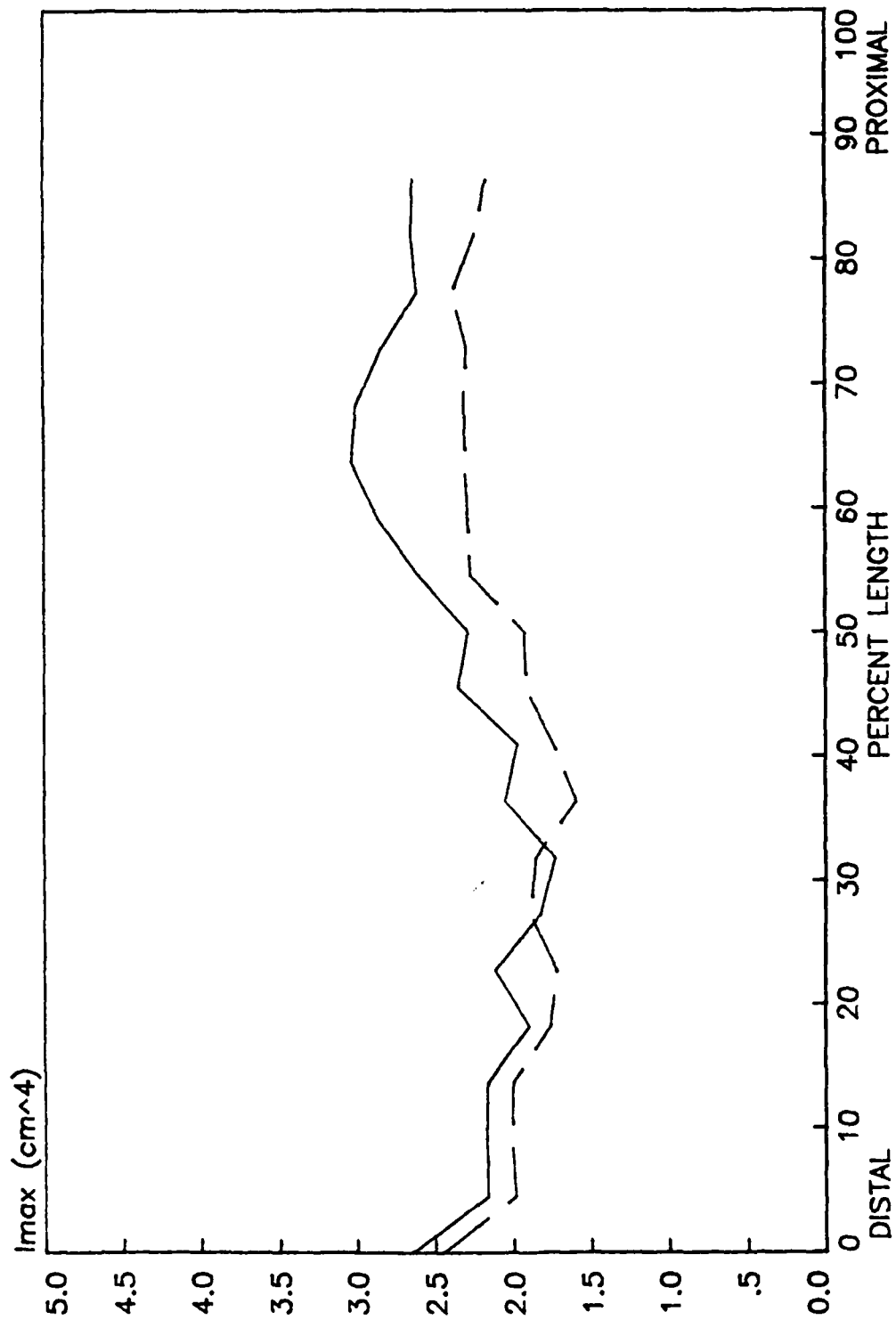
# HUMAN HUMERUS MAXIMUM MOMENT OF INERTIA

RIGHT

LEFT

\_\_\_\_\_

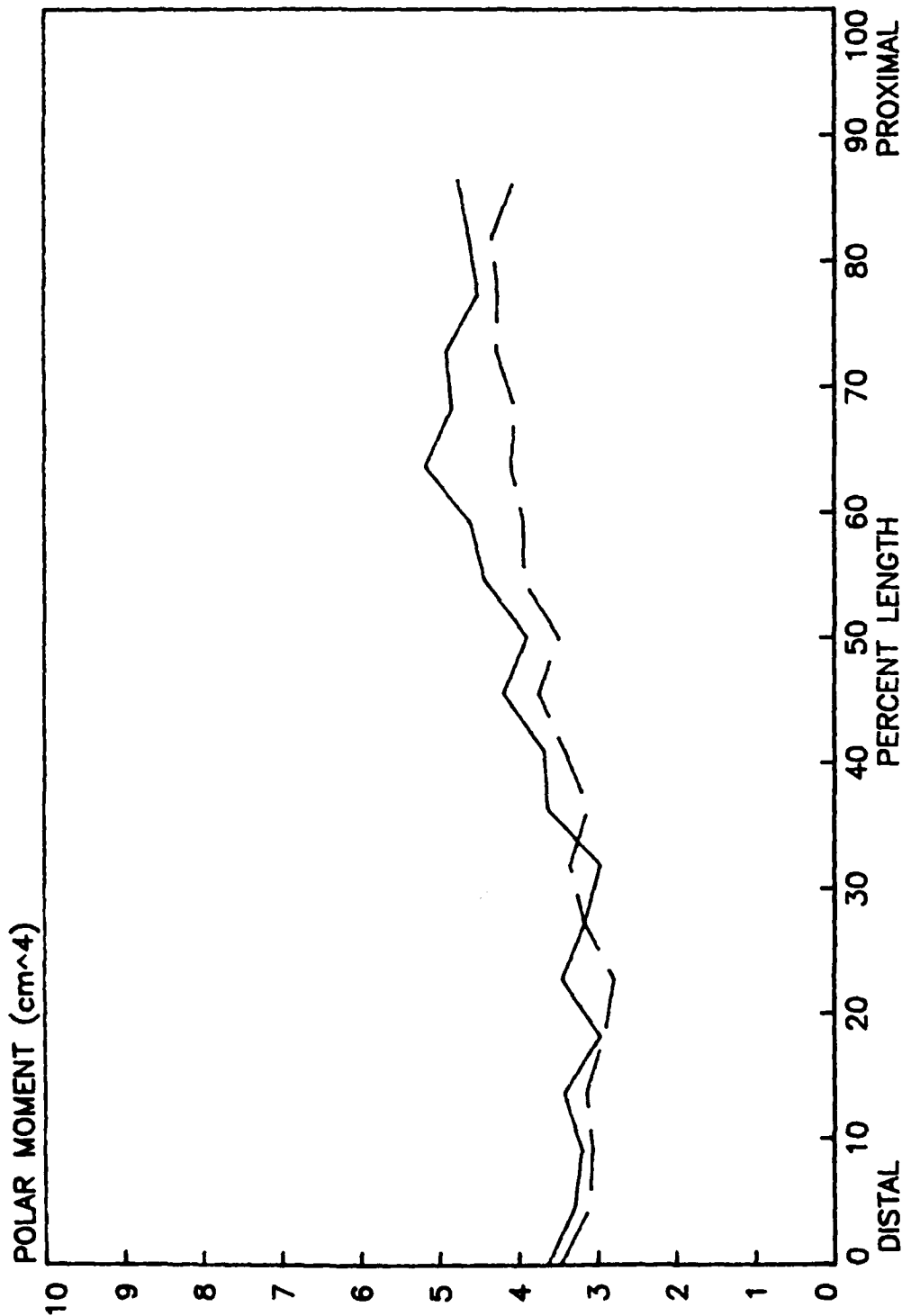
\_\_\_\_\_



# HUMAN HUMERUS POLAR MOMENT OF INERTIA

RIGHT

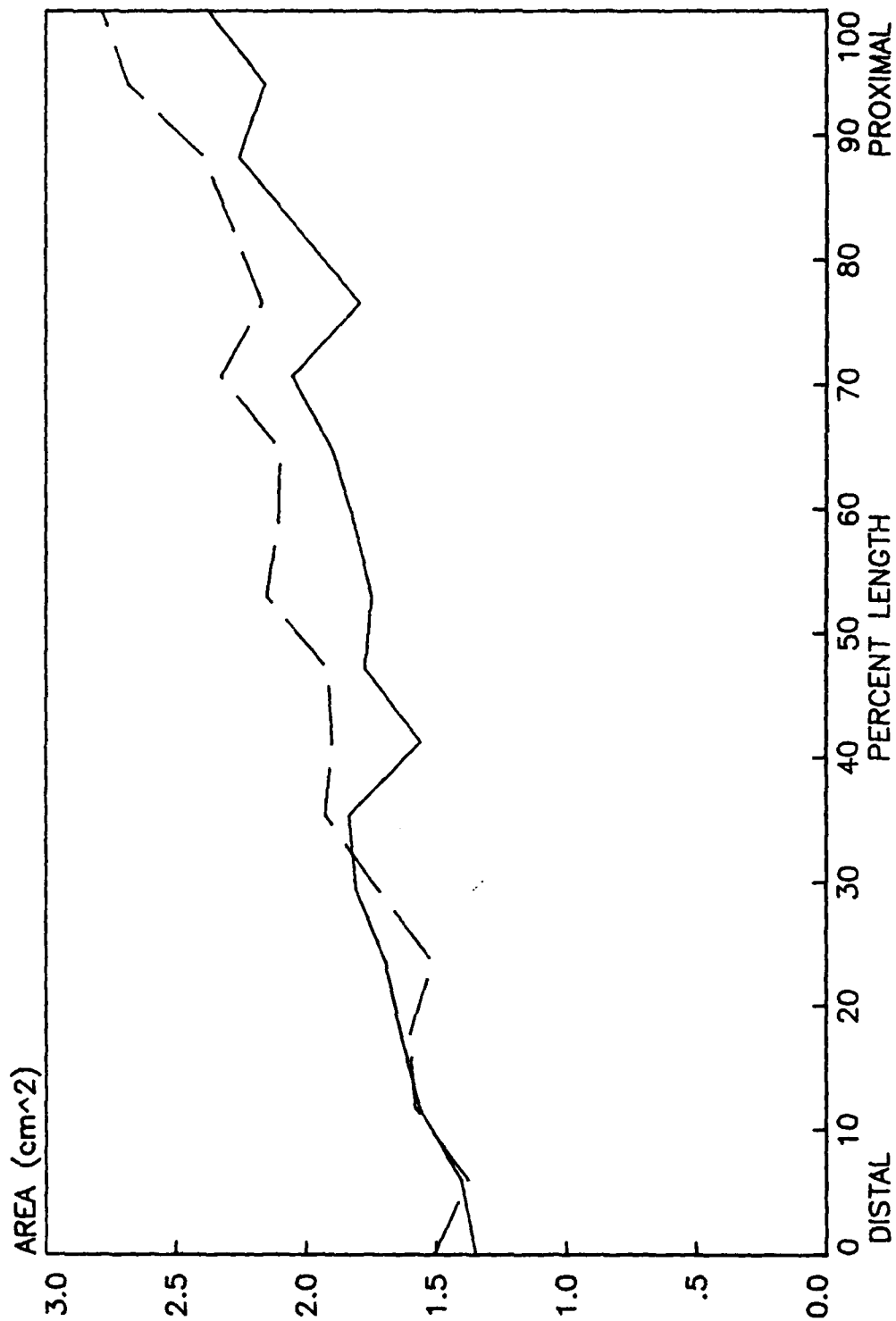
LEFT



# HUMAN ULNA AREA

RIGHT      LEFT

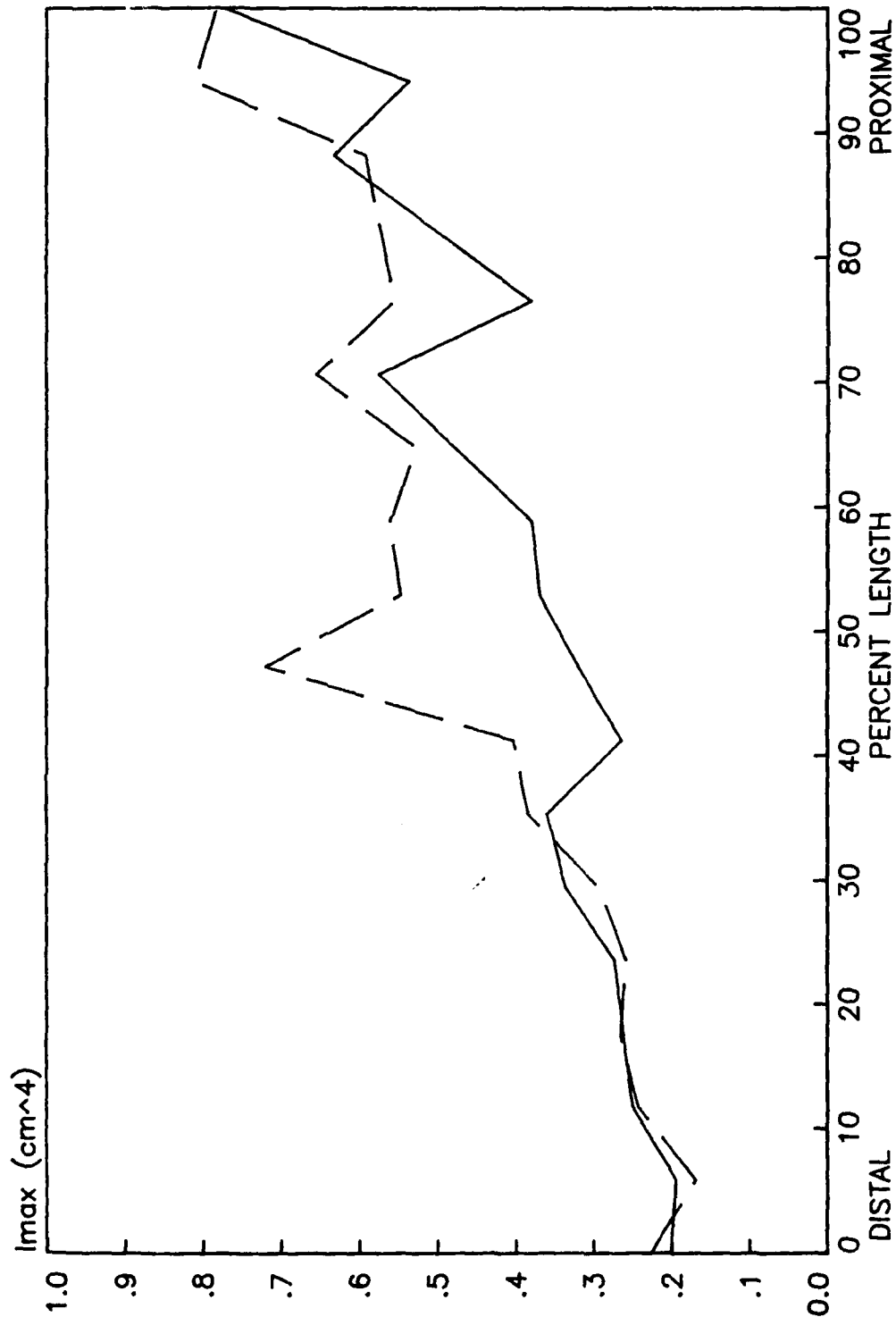
—      - - -



# HUMAN ULNA MAXIMUM MOMENT OF INERTIA

RIGHT      LEFT

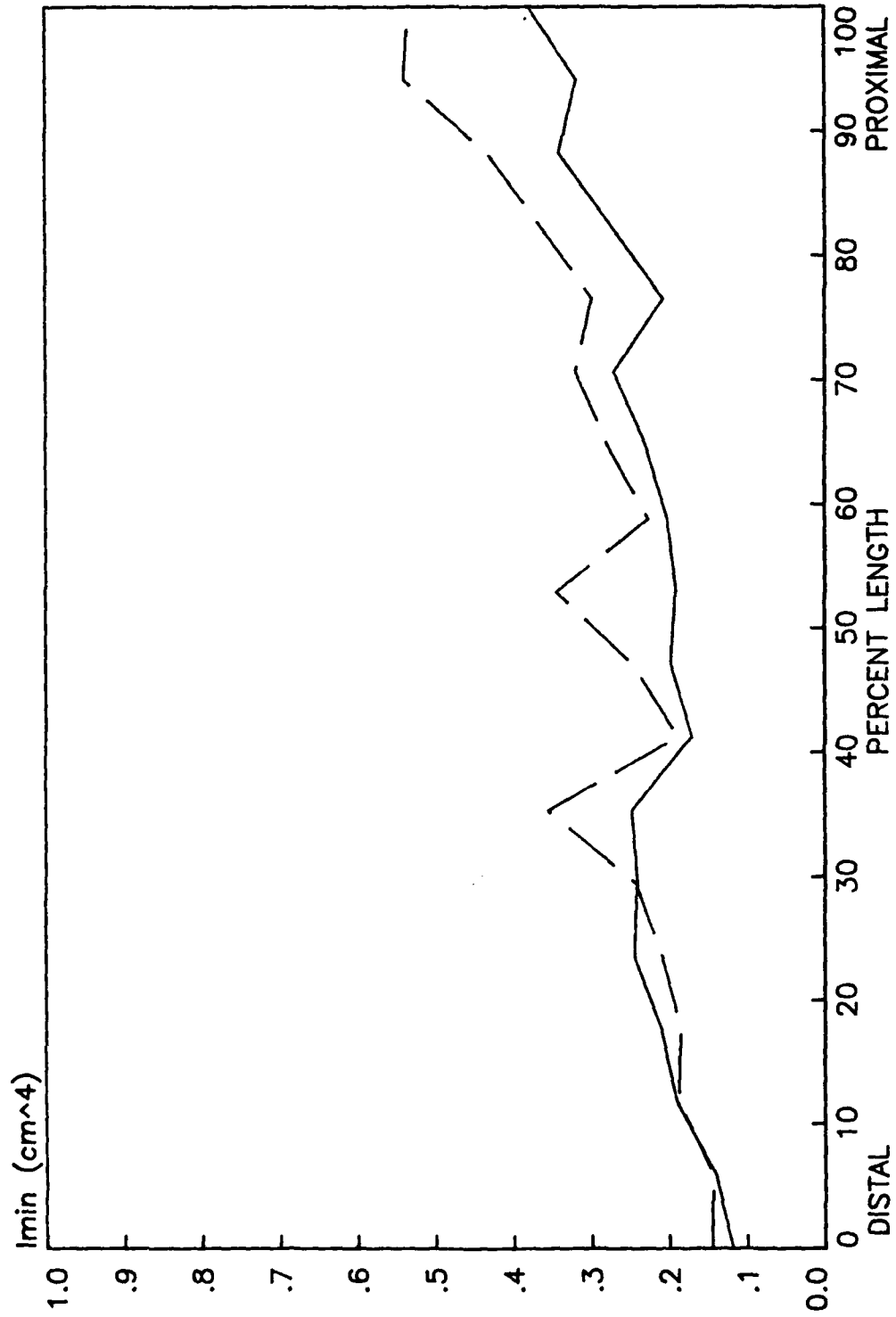
—      - - -



# HUMAN ULNA MINIMUM MOMENT OF INERTIA

RIGHT

LEFT

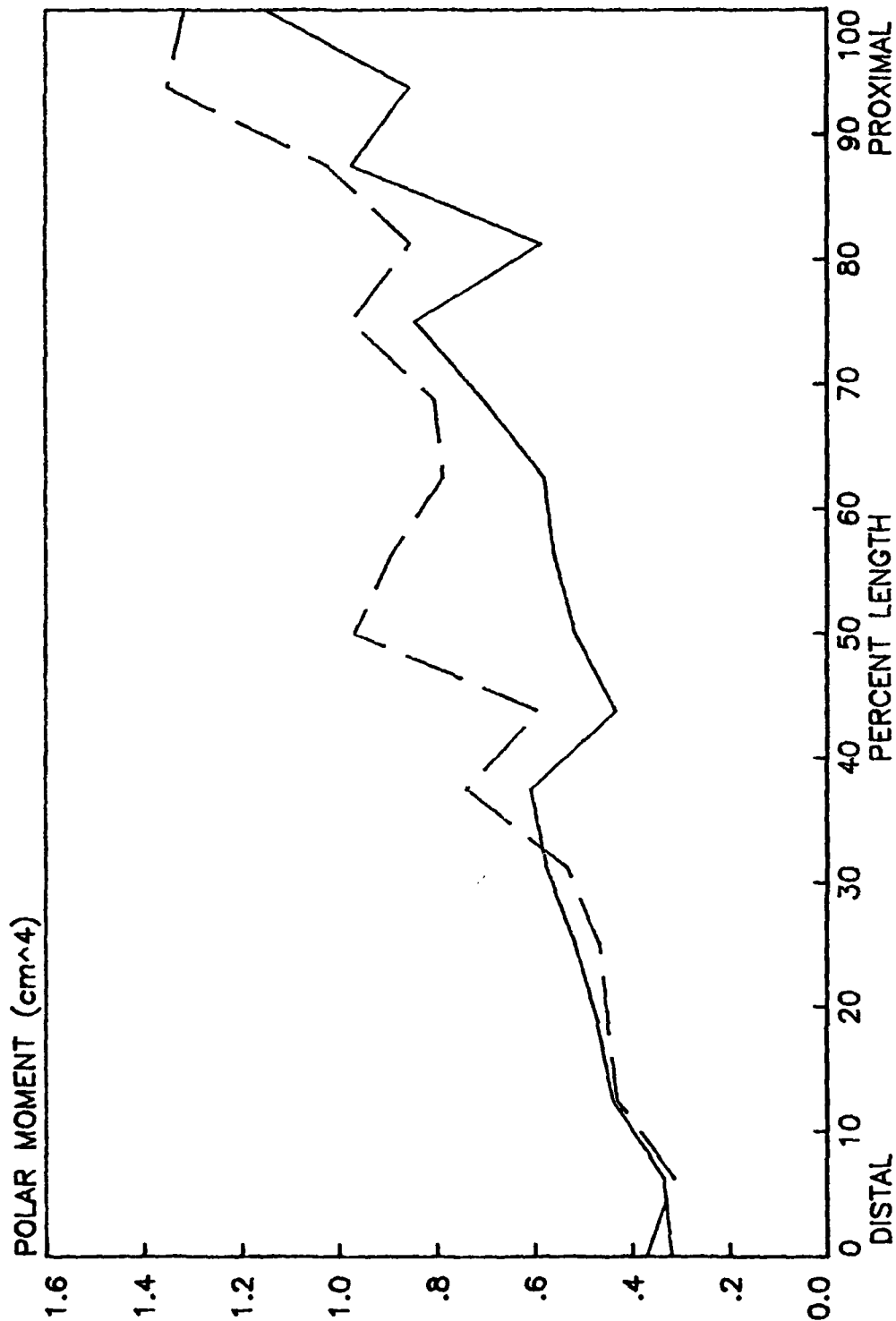




# HUMAN ULNA POLAR MOMENT OF INERTIA

RIGHT

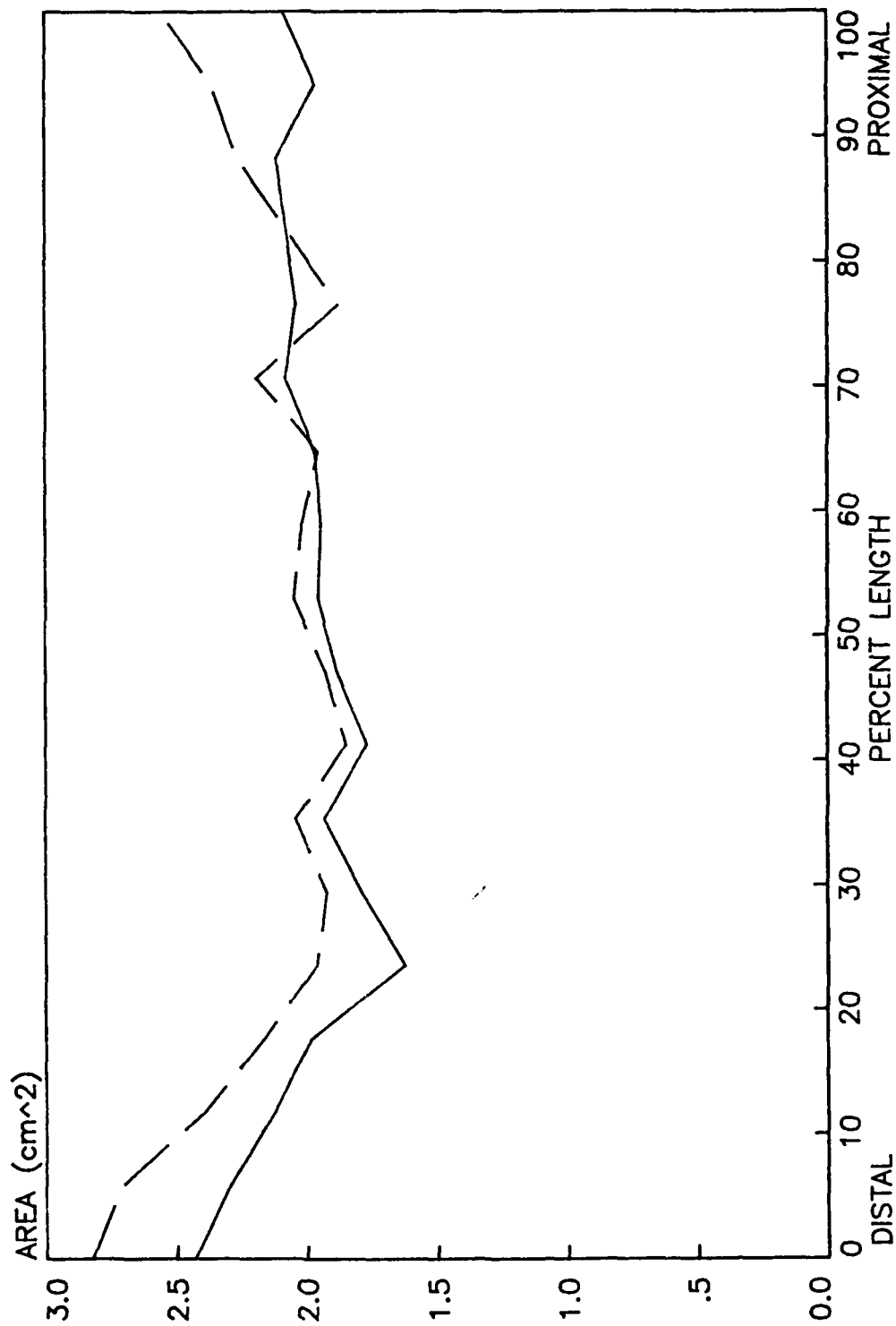
LEFT



# HUMAN RADIUS AREA

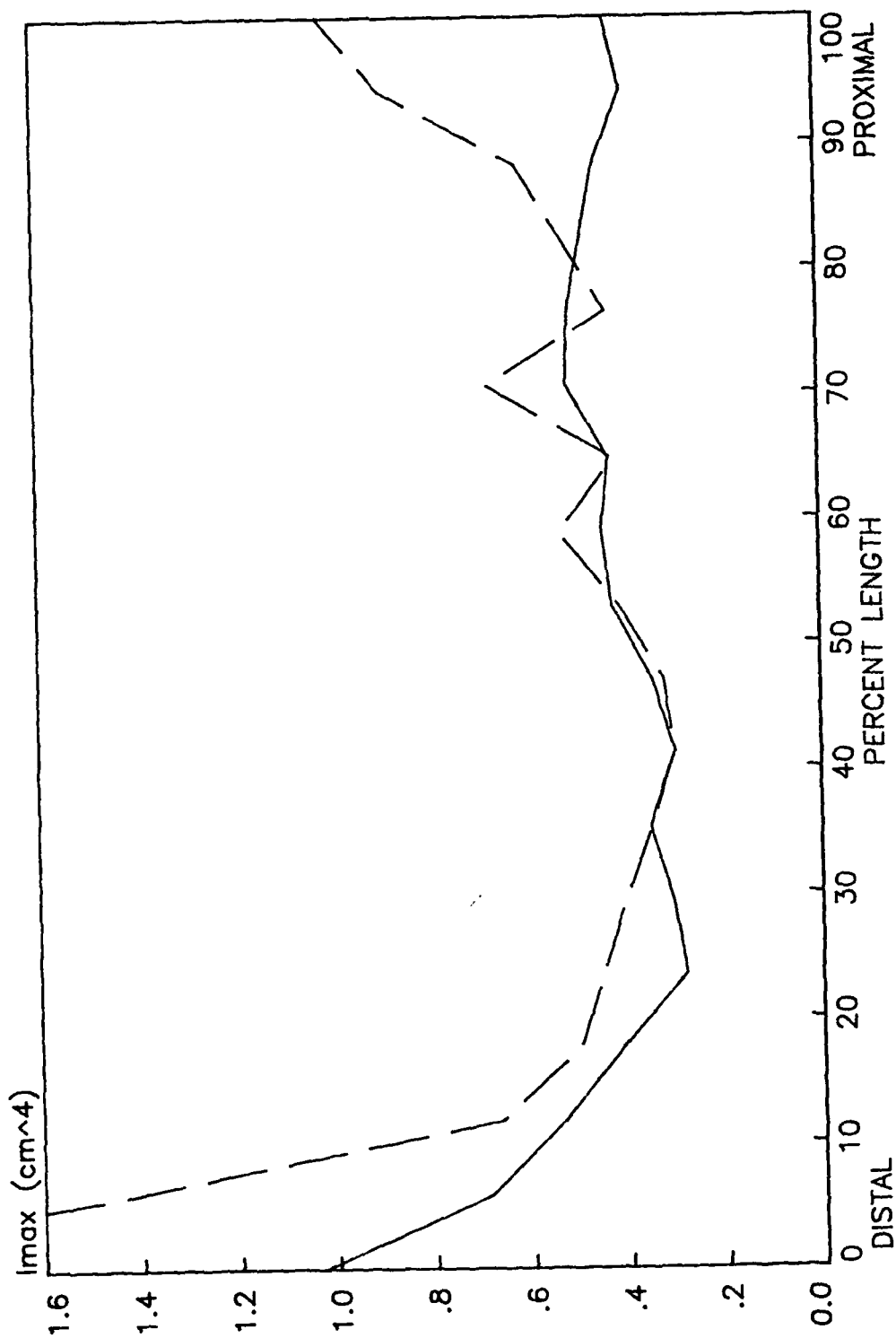
RIGHT

LEFT



# HUMAN RADIUS MAXIMUM MOMENT OF INERTIA

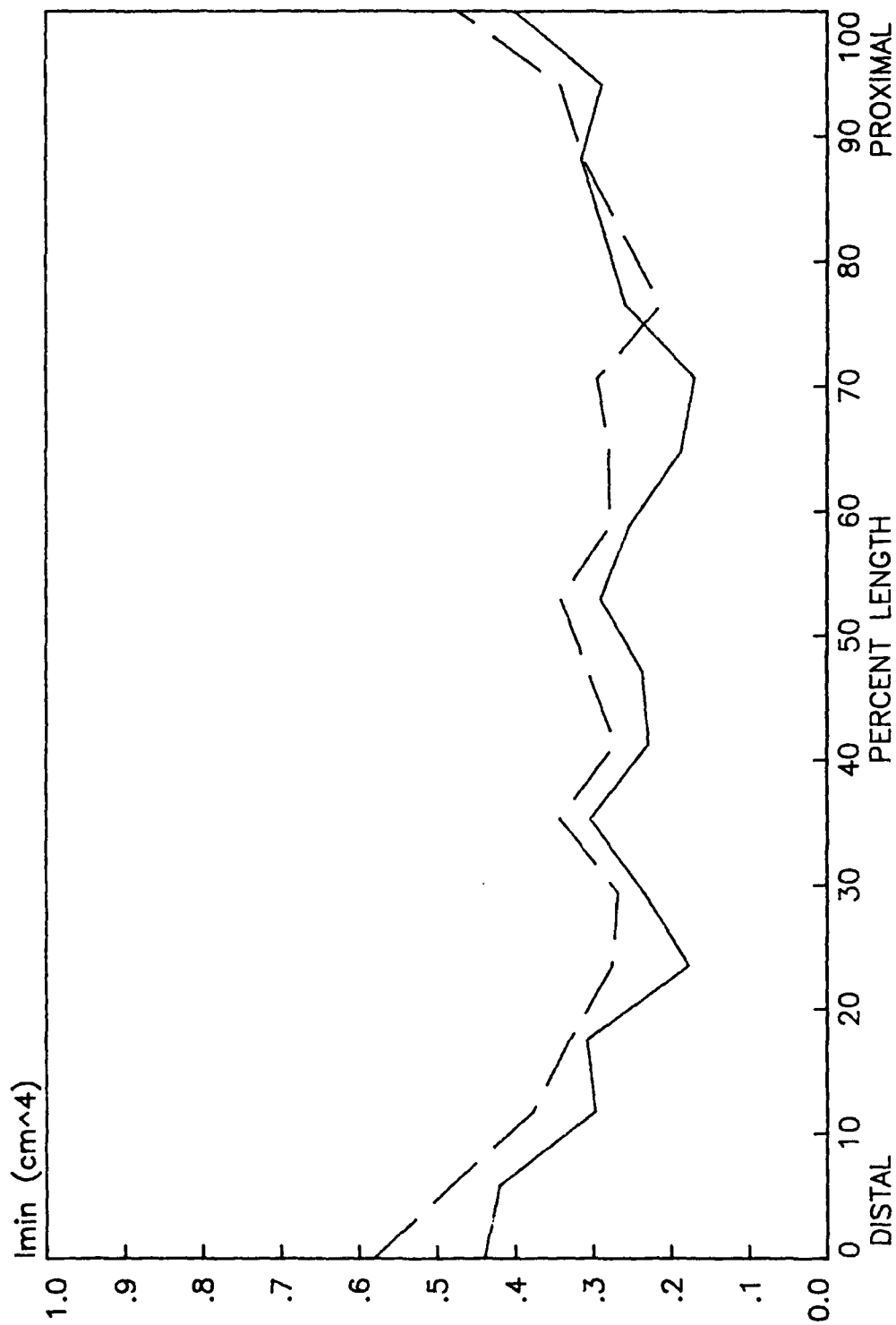
RIGHT      LEFT



# HUMAN RADIUS MINIMUM MOMENT OF INERTIA

RIGHT

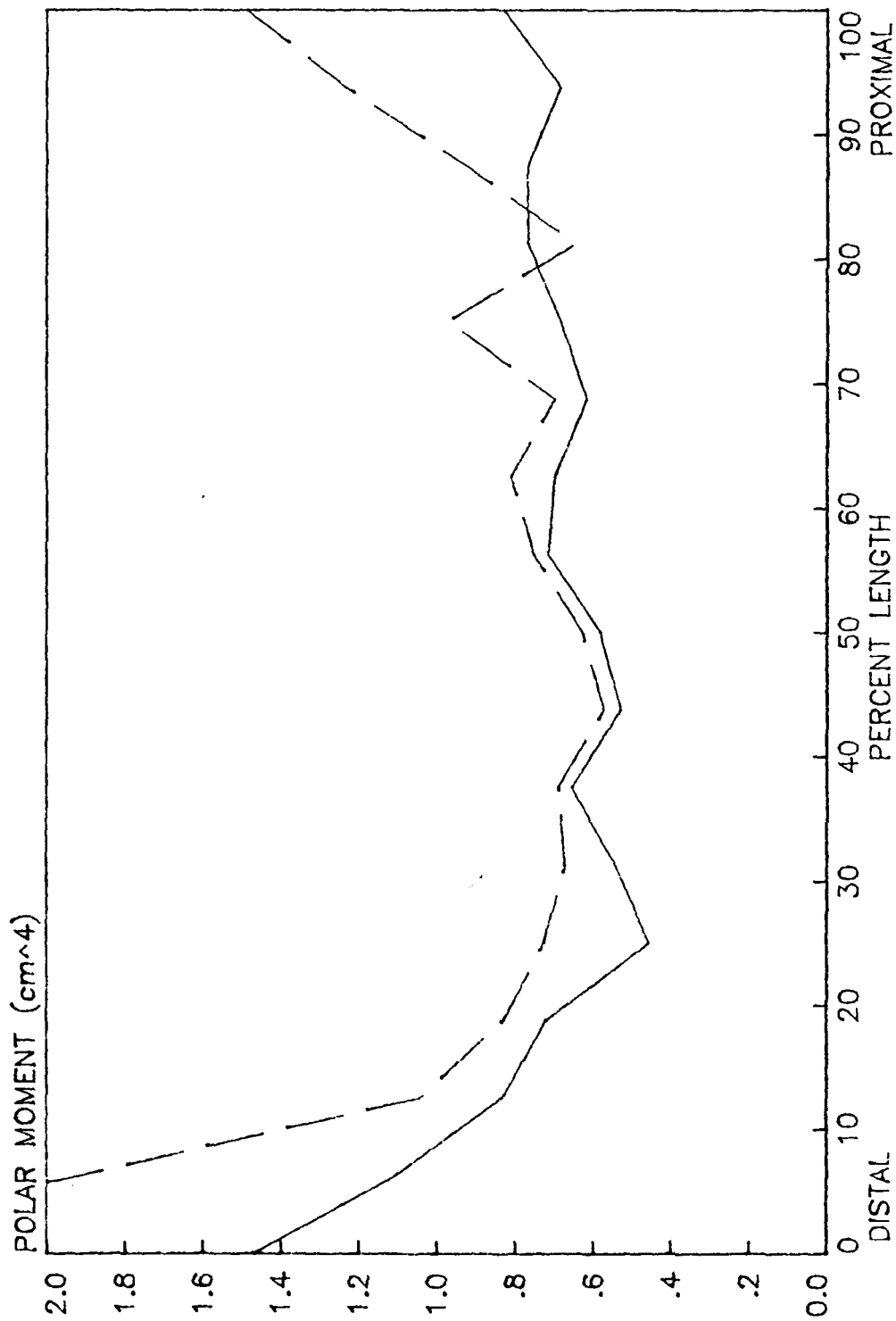
LEFT



HUMAN RADIUS  
POLAR MOMENT OF INERTIA

RIGHT

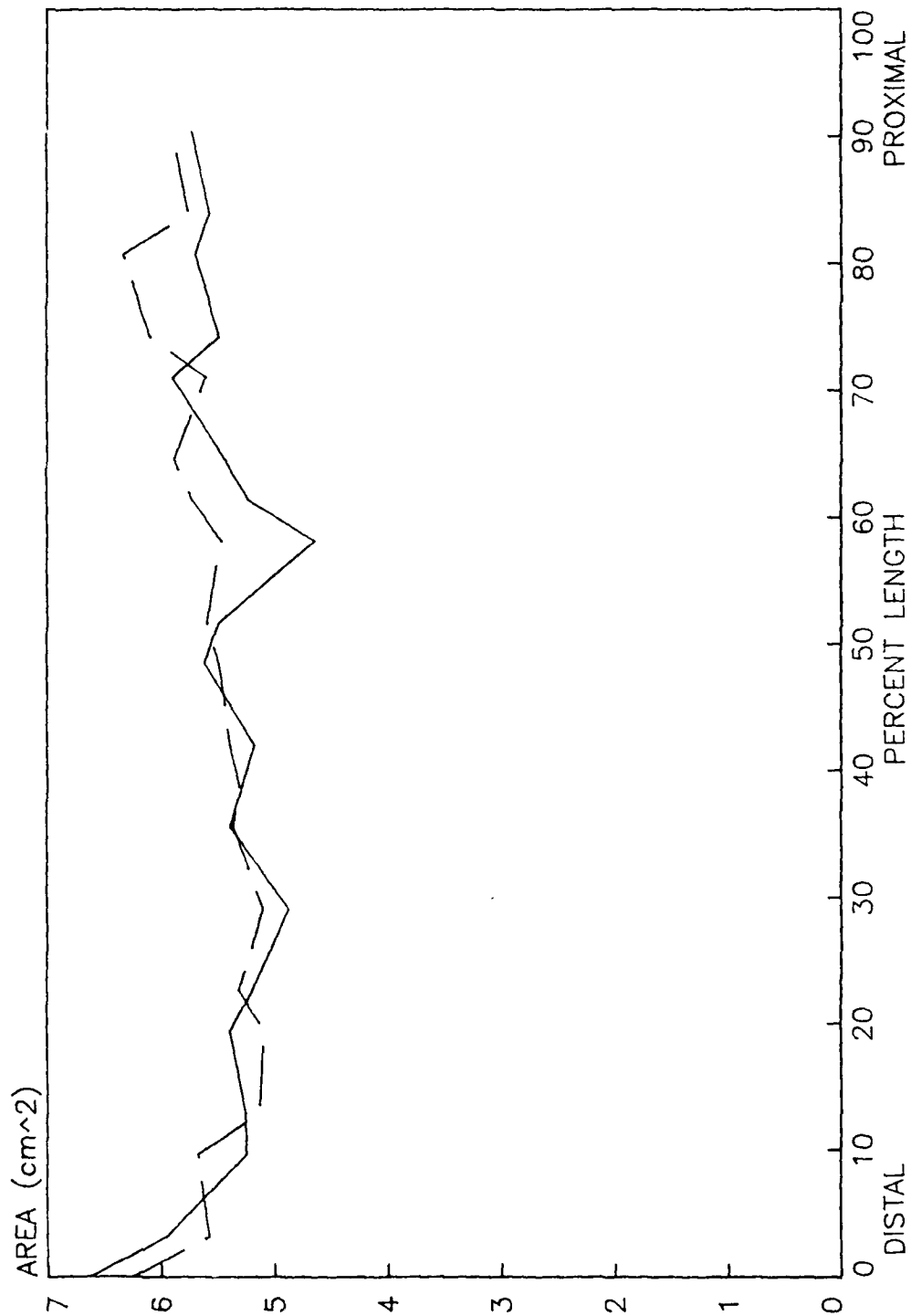
LEFT



# HUMAN FEMUR AREA

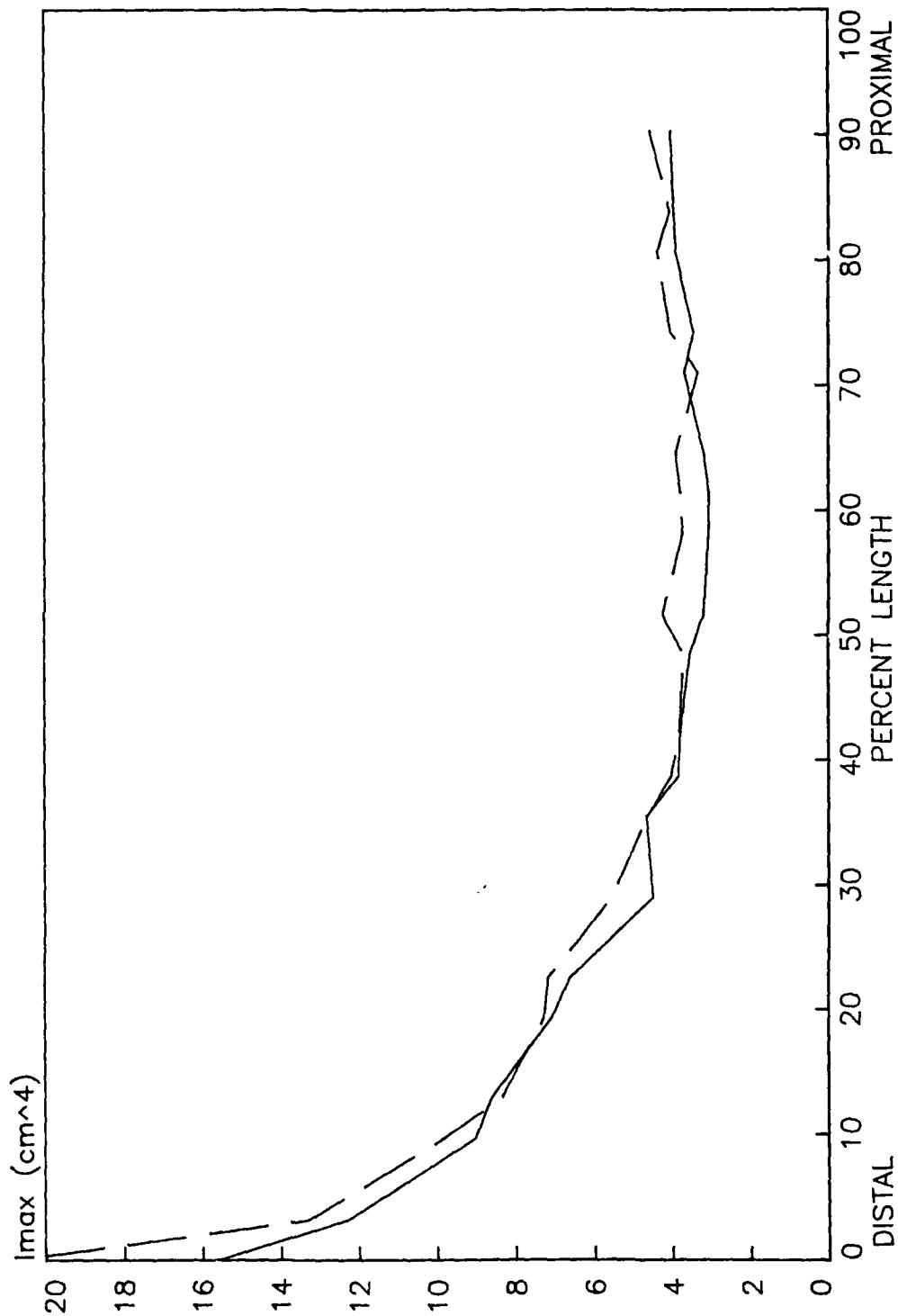
RIGHT

LEFT



# HUMAN FEMUR MAXIMUM MOMENT OF INERTIA

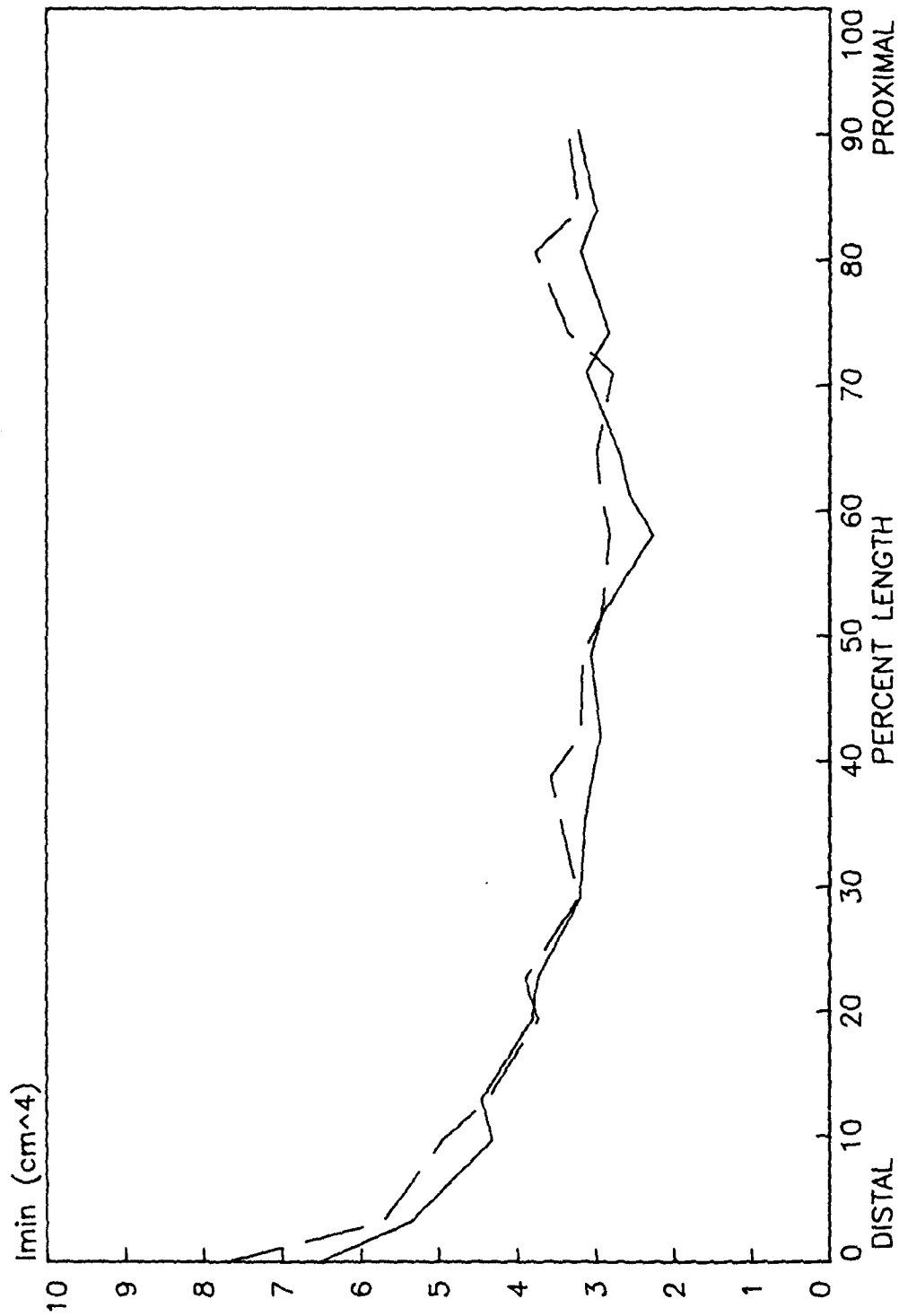
RIGHT      LEFT



# HUMAN FEMUR MINIMUM MOMENT OF INERTIA

RIGHT

LEFT

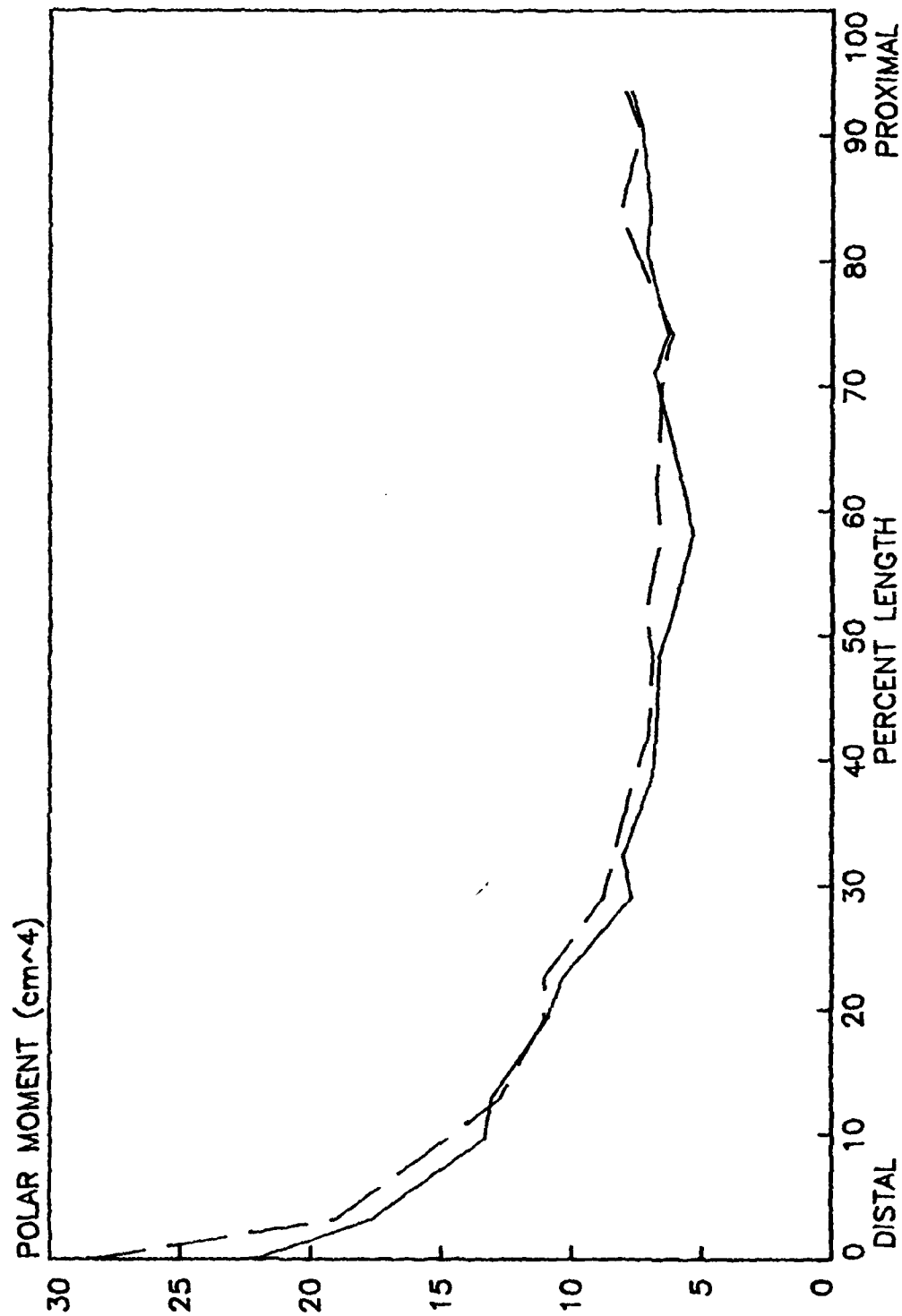




HUMAN FEMUR  
POLAR MOMENT OF INERTIA

RIGHT

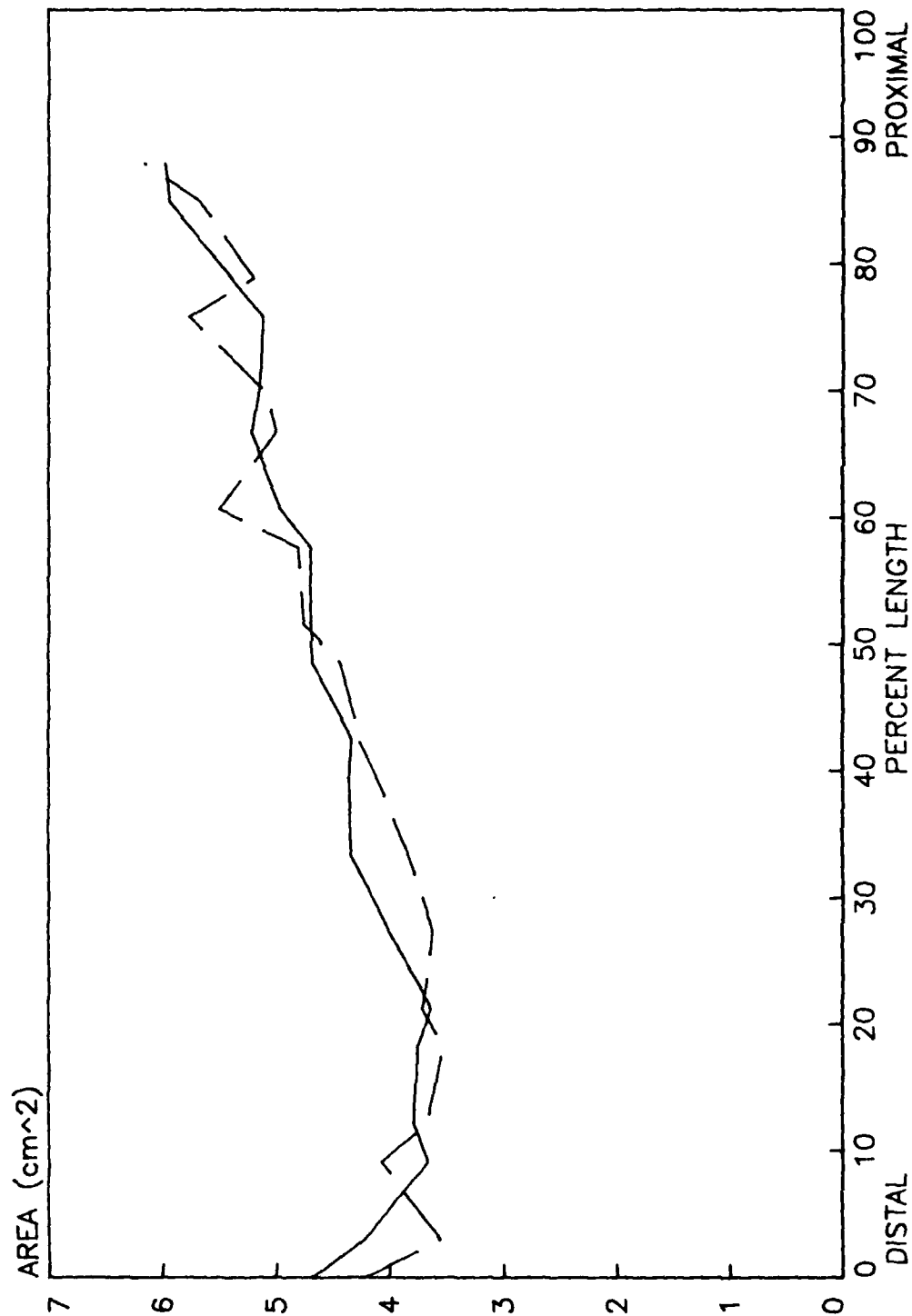
LEFT



# HUMAN TIBIA AREA

RIGHT

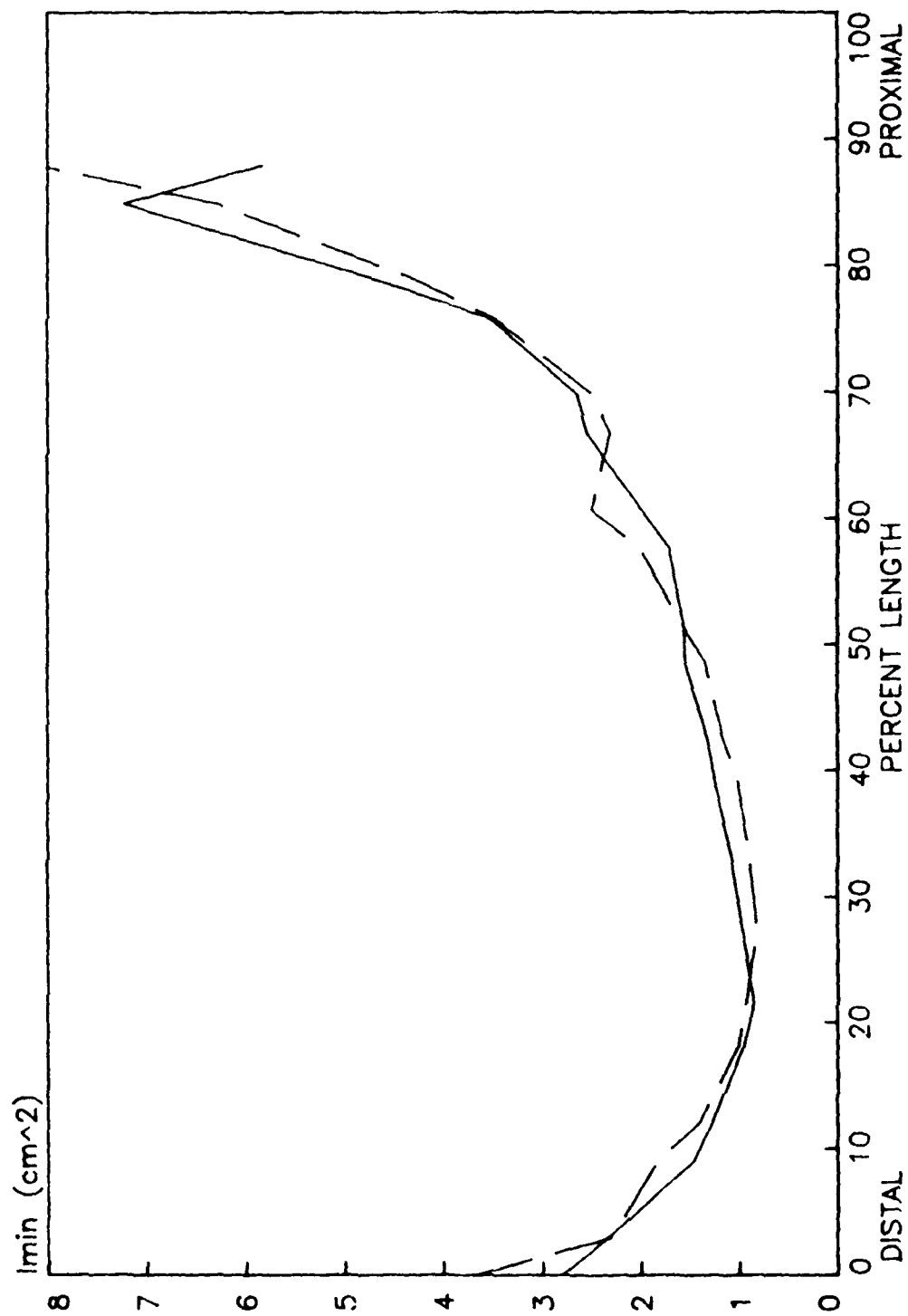
LEFT



# HUMAN TIBIA MINIMUM MOMENT OF INERTIA

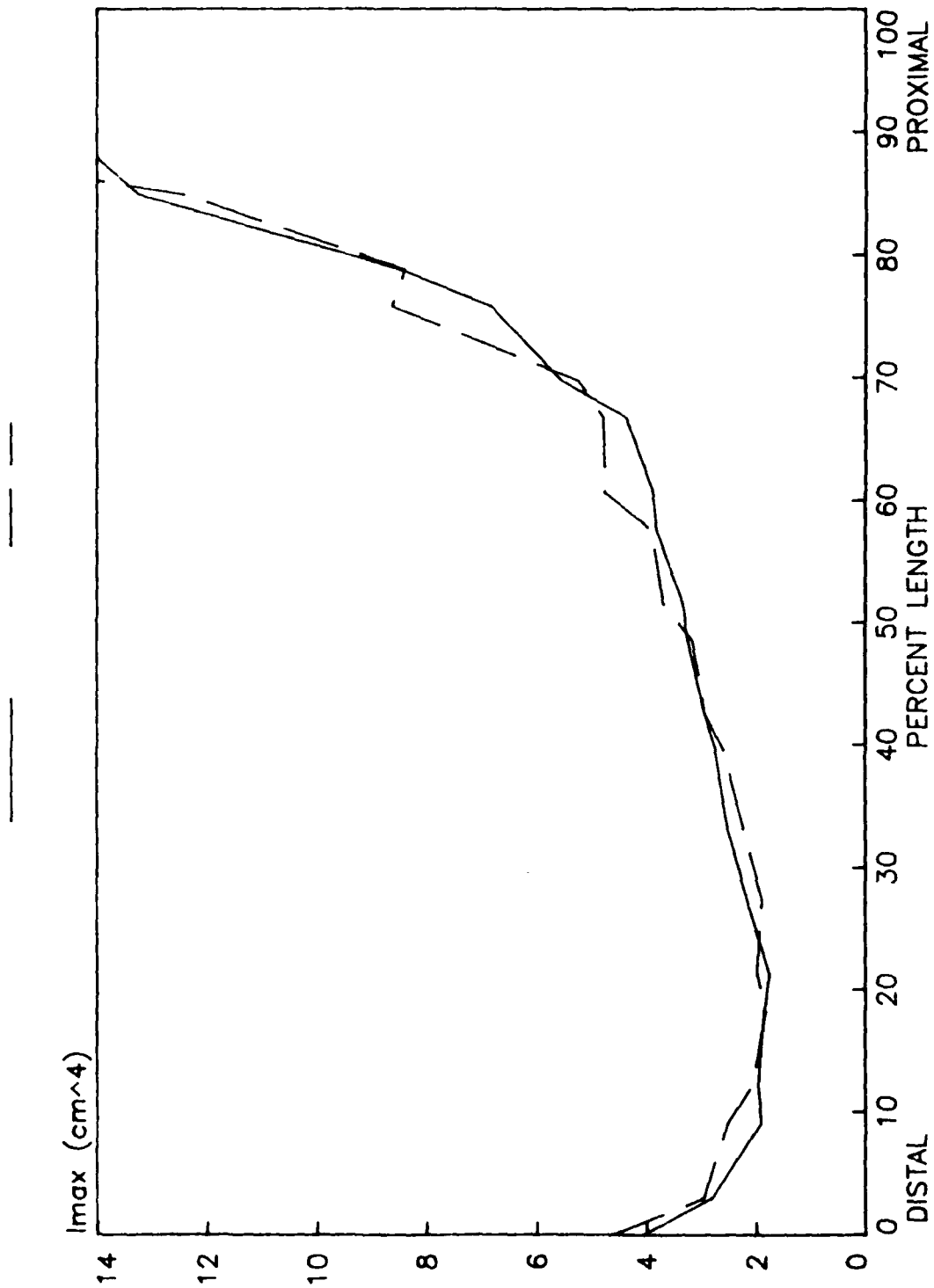
RIGHT      LEFT

\_\_\_\_\_



# HUMAN TIBIA MAXIMUM MOMENT OF INERTIA

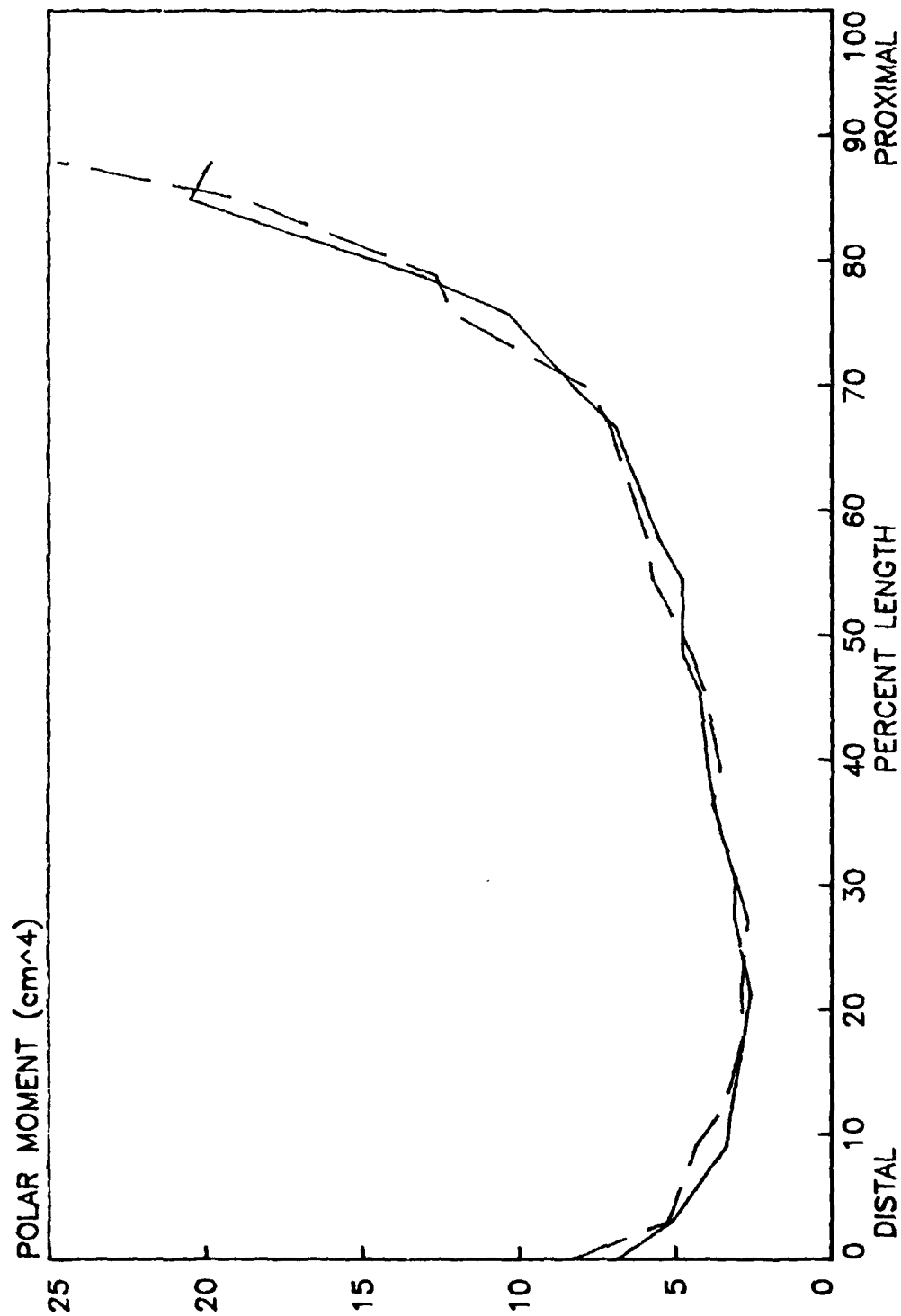
RIGHT      LEFT



# HUMAN TIBIA POLAR MOMENT OF INERTIA

RIGHT

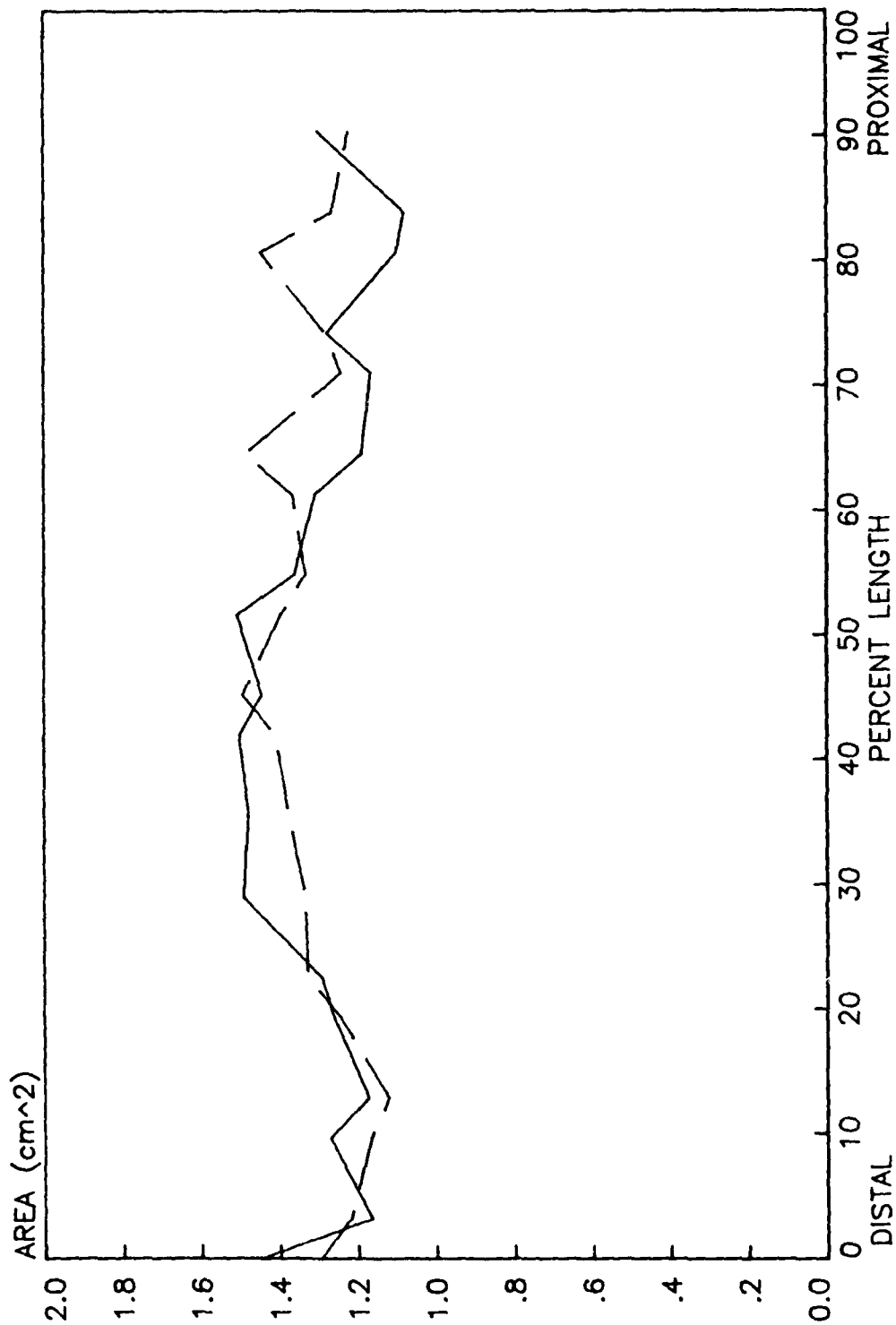
LEFT



# HUMAN FIBULA AREA

RIGHT

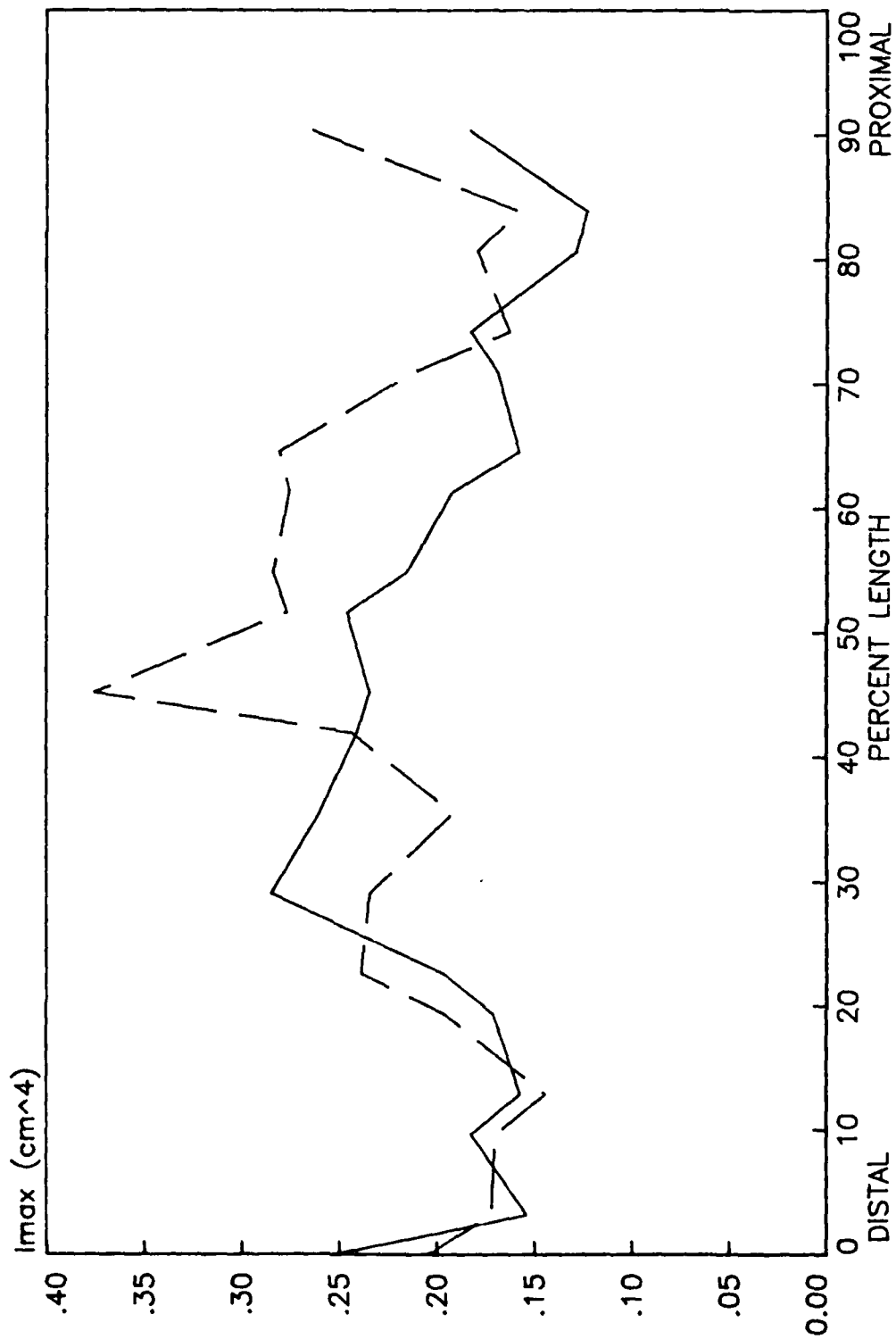
LEFT



# HUMAN FIBULA MAXIMUM MOMENT OF INERTIA

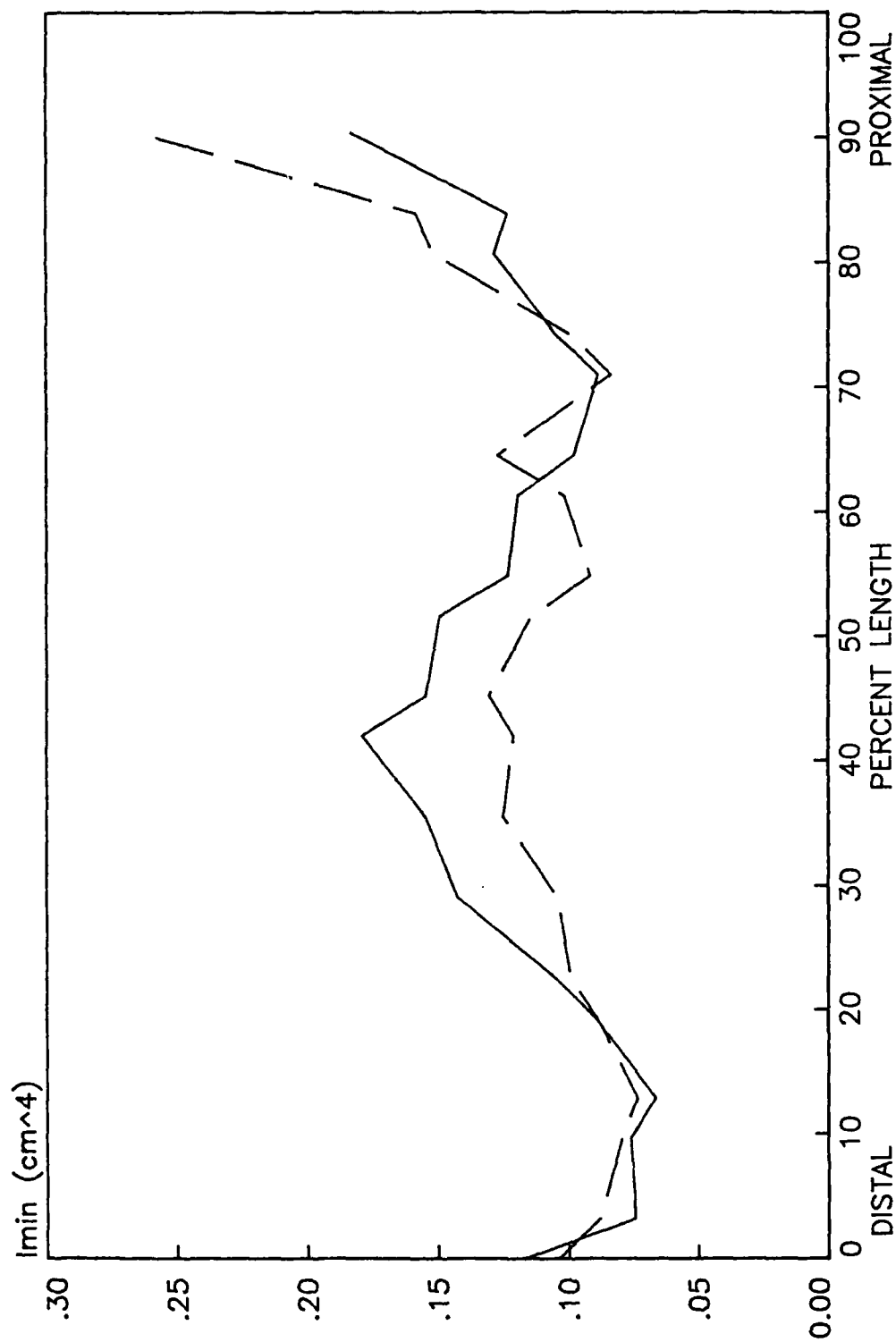
RIGHT

LEFT



# HUMAN FIBULA MINIMUM MOMENT OF INERTIA

RIGHT      LEFT





# HUMAN FIBULA POLAR MOMENT OF INERTIA

RIGHT      LEFT

